INTERACTION OF FLUIDS AND THIN STRUCTURES: SIMULATION AND APPLICATIONS

BY

Bo Yin

Dissertation
Submitted to the Faculty of the
Graduate School of Vanderbilt University
in partial fulfillment of the requirements
for the degree of

DOCTOR OF PHILOSOPHY
in
Mechanical Engineering

May, 2013

Nashville, Tennessee

Approved:
Professor Haoxiang Luo, Chair
Professor Greg Walker
Professor Amrutur V. Anilkumar
Professor Jon Edd
Professor Prodyot K. Basu

ACKNOWLEDGMENTS

First, I would like to thank Prof. Haoxiang Luo, my advisor, for his generous support and insightful guidance. His passion for research and wide interest always motivate me to go further in my study.

My commitment to the field of Computational Fluid Dynamics comes from my previous advisor, Prof. Yaosong Chen in Peking University of China. His passion for advancing this technology was stirring, and deeply motivated those around him. He introduced me to the field and gave me the confidence necessary to withstand challenging times. For that I am sincerely thankful.

I extend my thanks to Prof. Amrutur Anilkumar, Prof. Greg Walker, Prof. Jon Edd and Prof. Prodyot Basu for serving on my defense committee and reviewing my dissertation.

Having worked in Olin Hall for the past four and a half years, I have developed great relationships with the faculties, staff and students. I thank Dr. Nilanjan Sarkar for his support in my academic career. To Suzanne Weiss, I owe thanks for her supportive assistance. To my former and current labmates Dustin House, Paulo Ferreira de Sousa, Hu Dai, Fangbao Tian, Jialei Song, Shiyuan Chang and Chi Zhu, I own gratitude.

I appreciate my family's heartfelt support. They consistently encourage my educational endeavors. Above all, I would like to express my deepest gratitude to my mother Yulan Luo and father Guiming Yin. With their unconditional love, I could devote my best to graduate study. My dissertation is dedicated to them.

Finally I would like to thank the American Chemical Society Petroleum Research Fund and National Science Foundation for supporting my research.

CONTENTS

LIST OF FIGURES

CHAPTER 1

INTRODUCTION

1.1 Motivation

1.1.1 Interaction of fluids with thin solid structures

The interactions between fluids and thin structures can be found in many examples in nature, for instance, elastic membranous wings of insects [1], undulating fins of fish [2], flapping flags and tree leaves in the wind, oscillations of underwater plants in unsteady currents, rotating flagella of bacteria [3], deformation of cell membranes [4] (see Fig. 1.1). Complicated fluid–structure interaction (FSI) is involved in these systems. Computational modeling of these system is typically very challenging because the solid bodies experience large displacements, which causes the mesh generation in the conventional methods of computational fluid dynamics (CFD) to be an expensive and sometimes even formidable procedure.

We are specifically interested in two applications in this work: (1) aerodynamics of the flapping wings of insects; and (2) energy harvesting using tree-leaf-like structures attached with piezoelectric materials. The background of each application is briefly discussed here and will be further described in the pertinent chapter.

Aerodynamics of insect flight has drawn considerable attention in recent years due to its promising application in the development of biomimetic micro air vehicles [5]. During flight, insect wings typically experience dynamic deformations [6], i.e., change of the wing shape from its rest configuration regardless the position or orientation of the wing. Even though the deformation magnitude and pattern vary from species to species, physiological studies have shown that insect wings do not possess an internal actuation mechanism and thus the deformation has to be passive [7]. That is, an insect wing is

(a) A hovering hummingbird (Credit: Dean E. Briggins, U.S. Fish and Wildlife Service)

(b) Swimming fish (Credit: Dr. James C. Liao, University of Florida)

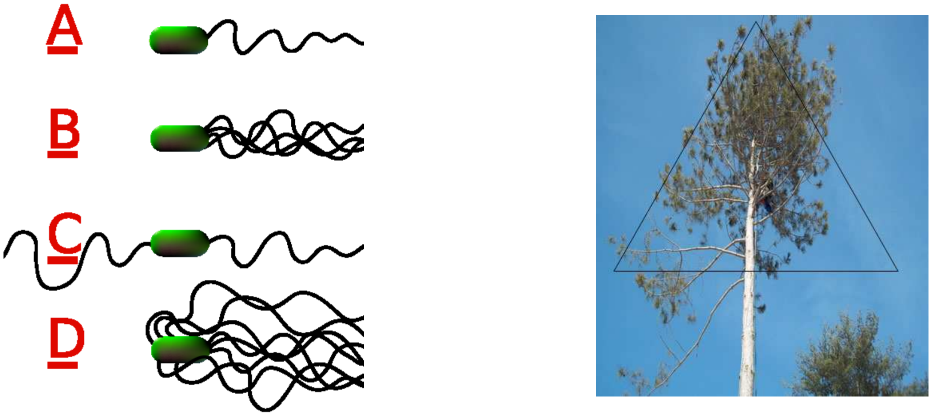

(c) Bacterial flagella (Credit: Michael D. Jones, http://en.wikipedia.org/wiki/Flagellum)

(d) Tree leaves (Credit: Dr. Yahya Modarres-Sadeghi, University of Massachusetts)

Figure 1.1: Interactions between fluids and thin structures.

deformed by the external means, i.e., the aerodynamic force from the air around the wing, or due to the wing acceleration, i.e., the inertial force. The mass ratio describing the relative effect of the wing inertia with respect to the aerodynamic force is difficult to match in an experiment requiring dynamic similarity. Therefore, a computational study would be very useful in studying the effect of wing deformation.

On a separate application, recent experimental studies have demonstrated that tree-leaf-like thin structures can be used as energy harvesters when placed in a flow [8–10]. When the structure is vibrating due to vortex shedding, the piezoelectric material

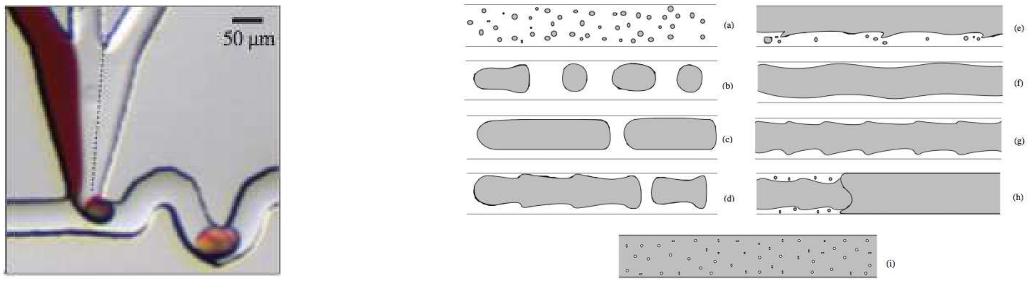

(a) A wavy microchannel for drop-based mixing (Credit: Bringer et.al [12])

(b) Water-oil flows used in pipeline transport of crude oils (Credit: D.D. Joseph et.al [13])

Figure 1.2: Interactions of flows with fluid–fluid interfaces.

attached to the structure converts the kinetic energy into electricity through a circuit. The device may be potentially used to power small electronic devices. In the work of [11], a single leaf unit is able to produce an amount of power around 300 μW. So it may be possible to use multiple units to power a small electronic device that requires power on order of 100 mW. Nevertheless, the efficiency of the energy harvesting needs to be improved significantly in order for such a mechanism to have practical use. Therefore, a study of the flow-induced vibration of an array of thin structures will be useful for exploring the parameter regime in which the system would have enhanced performance.

1.1.2 Interaction of fluids with fluidic interfaces

In a different situation, two-phase flows of immiscible fluids (e.g., oil and water, or air and water) have wide applications in industry ranging from microfluidics to pipeline transport of crude oils (see Fig. 1.2). The interface between the two liquids has zero thickness, and across the interface, the velocity is continuous but the traction undergoes a jump due to the presence of the surface tension. In a sense, such a fluid–fluid interface may be viewed as a thin structure that may be stretched and bent. Compared to the thin solid bodies, there are added complexities for modeling such fluid–fluid interfaces, as these interfaces not only go through great bending and stretching deformations but may also experience topological changes, e.g., breakup and coalescence.

For two-fluid flows in arbitrary domains, both types of boundaries, i.e., the fluid–solid interface and the fluid–fluid interface, would appear in one problem. For example, microchannels with intricate shape features were used to generate and manipulate droplets carrying living cells [14] or physiological fluids [15] on microfluidic devices. Pipeline transporting heavy oils using water lubrication, known as core–annular flow, involves geometries such as pipe fittings, T-junctions, and contractions/expansions of the cross section [16]. Combustion chambers with sophisticated interior design have massive behaviors including break-up and coalescence of liquid fuel drops [17].

The existing methods of numerically simulating two immiscible fluids in non-trivial geometries are usually based on meshes that conform to the surface of the solid, i.e., either a curvilinear grid or an unstructured grid, so that the boundary conditions, typically no-slip and no-penetration wall conditions, can be applied at the surface straightforwardly. On the other hand, there are several approaches for handling the interface between the two fluids in which the computational mesh does not have to conform to the interface. Based on the approach of tracing the fluid–fluid interface, the existing methods for modeling multi-fluid flows include the following: (I) the Lagrangian mesh approach, where the interface is represented by a set of marker points and a mesh moving with the local fluid. (II) the volume-of-fluids (VOF) method, where the interface is represented by the volume fraction of the fluids [18]; (III) the level set function, where the interface is represented by the zero-level contour of a distance function [19]; and more recently (IV) the phase-field method, where the interface is represented by the chemical energy level of the fluids [20]. In the first method, the surface tension can be directly incorporated into the boundary condition if the volume mesh moves together with the interface, e.g., the arbitrary Lagrangian-Eulerian (ALE) method [21], or it can spread into the fluid near the interface if the volume mesh is fixed, e.g., the front-tracking method [22]; Among these methods, only the ALE method requires the volume mesh to be adapted to the moving interface, and the other methods can be built on a fixed mesh. Furthermore, except the Lagrangian mesh approach that utilizes an explicit surface meshing technique, the other methods use a scalar variable advected by the flow to trace the interface implicitly, and they have the inherent capability of handling topological changes of the interface.

The immersed-boundary methods based on fixed meshes, especially Cartesian grids, have been developed and applied extensively in treating complex and moving boundaries of solids. In its original version, Peskin [23] converted the surface traction exerted by the thin elastic body immersed in the fluid into a volume force using a regularized Dirac's delta function. Conceptually, this method closely resembles the front-tracking method and thus both can be categorized as the diffuse-interface method. After Peskin's work, several other families of the Cartesian grid based approaches were developed for arbitrary solid boundaries and were dubbed with terms such as the immersed-interface method [24], the embedded-boundary method [25], or still, the immersed-boundary method [26]. These later methods have significantly deviated from Peskin's original notion of an immersed boundary in that they retain the surface-force nature of the traction from the solid boundary and are therefore referred to the sharp-interface method [26]. Nevertheless, compared with the curvilinear or unstructured grid based methods, the common advantages of these immersed-boundary methods are simple mesh generation and efficient computational algorithms that are based on the Cartesian grid. In all these methods, an explicit mesh representing the solid body is needed. For further reviews of the immersed-boundary methods and also additional methods that are based on fixed grids, e.g., the fictitious domain method, the readers are referred to the works of [27], [26], and [28].

Having listed many non-boundary-conformal approaches for either fluid–fluid interfaces or fluid–solid interfaces, we point out that there are few approaches available that utilize Cartesian meshes to treat both types of interfaces in one program. The major reason for this is that the two interfaces are associated with different characteristic deformations and also boundary conditions. A fluid surface typically can be bent and stretched to a large degree, or even change its topology substantially, while a solid surface may be rigid or inextensible (e.g., a moving piston or an elastic airplane wing). With regard to the boundary conditions, the velocities are usually specified for a solid surface, while a fluid surface involves the unknown interfacial velocity but a known traction jump across the interface due to the presence of the surface tension. As a result, none of the aforementioned methods is readily suitable for both types of surfaces in general. For example, an explicit mesh using Lagrangian markers may be suitable for representing a solid surface but has difficulty dealing with morphology of a fluid surface. On the other hand, the level set method can handle interfacial morphology easily, but it cannot give the location of the interface explicitly and thus is not straightforward for implementation of the no-slip condition at a solid surface.

Therefore, a proper combination of some of the existing methods based on Cartesian grids would be appropriate for simulating two immiscible fluids involving solid boundaries of arbitrary geometries. In the present work, we combine the level-set method for the fluid surface and a sharp-interface immersed-boundary method for the rigid or deformable solid boundary. For the solid boundary, the sharp-interface treatment is chosen because the method is typically second-order accurate as opposed to the generally first-order accuracy for the diffuse-interface treatment [29]. Furthermore, for a rigid body, an iterative approach would be needed in the diffuse-interface treatment for the no-slip boundary condition to be satisfied, which may lead to slow convergence or even numerical instability [26]. The combined method presented in this work will have the following features: (1) easy to represent both fluid and solid surfaces, even if the surfaces are complex-shaped or moving, (2) straightforward to incorporate the boundary conditions associated with each type of the interfaces, (3) capable of handling the topological change of the fluid surface, and (4) simple mesh generation and efficient computation on the Cartesian grid.

1.2 Objectives of the dissertation

The specific objectives of this work can be summarized as follows:

1. Computationally model the fluid–structure interaction of the flapping wings of insect and study (1) the effect of wing deformation on the aerodynamic performance of the wing and (2) the relative role of the wing inertial with respect to the aerodynamic force.

2. Computationally model the hydrodynamic interaction between the thin structures that are placed in close range and seek the regime in which the energy level of the entire system is significantly increased; and if such a regime is found, the underlying physical mechanism will be studied.

3. Develop a three-dimensional immersed-boundary method that can be used to simulate two immiscible fluids in arbitrary domains. The method should be able to capture both the morphological and topological changes of the fluid–fluid interface.

4. Use the immersed-boundary method to study the dynamics of drops traveling through microchannels with asymmetric wall bumps and to investigate the interior flow pattern for the purpose of mixing enhancement.

1.3 Outline of the dissertation

This dissertation includes the discussion and implementation of the numerical algorithms for treatment of the fluid–solid interface and the fluid–fluid interface, and it also covers three independent applications of the current method.

Chapter 1 provides the overall motivation for a numerical method capable of simulating the interaction between fluids and thin structures. The background of the three applications are briefly described.

Chapter 2 provides the descriptions of the numerical methods. The Navier-Stokes equations are numerically solved on a fixed Cartesian grid. The sharp and diffuse immersed-boundary methods are combined in one program to separately treat the fluid–solid interface and the fluid–fluid interface. The level-set function is introduced with the mass conservation and stability issues addressed. Numerical validation cases are provided.

Chapter 3 describes the application of the current method to the fluid–structure interaction of flapping wings. A two-dimensional model is developed to model the hovering flight of insects. The effect of wing deformation and the role of the wing inertia are addressed by varying the mass ratio and structural flexibility of the wing. The implication of the findings on insect flight is discussed.

Chapter 4 describes the application of the current method to the fluid–structure interaction of an array of elastic sheets placed in a free stream. The parameter regime for the system resonance is studied, and the mechanism of the resonance is examined in detail.

Chapter 5 describes the application of the current method to the drops going through an asymmetric microfluidic channel that has bumps on one side. The parameters that lead to the asymmetric flow pattern inside the drops are investigated for the purpose of mixing enhancement.

Chapter 6 provides a summary of the dissertation. Overall conclusions and contributions are presented, and future work based on the current results is suggested.

CHAPTER 2

NUMERICAL METHOD FOR THE FLOW

2.1 Governing equations and numerical discretization

The fluid in this study is considered to be viscous, incompressible and Newtonian. The governing Navier-Stokes equation for the viscous incompressible flow is written as

$$\begin{aligned} \rho\left(\frac{\partial \mathbf{u}}{\partial t} + \mathbf{u}\cdot\nabla\mathbf{u}\right) &= -\nabla p + 2\,\nabla\cdot(\mu\,\mathbf{E}) + \mathbf{F} \\ \nabla\cdot\mathbf{u} &= 0, \end{aligned} \tag{2.1}$$

where $\mathbf{u} = (u, v, w)$, p, ρ, μ are the velocity, pressure, density, and viscosity, respectively,

$$\mathbf{E} = \frac{1}{2}(\nabla\mathbf{u} + \nabla\mathbf{u}^T) \tag{2.2}$$

is the rate-of-deformation tensor, and $\mathbf{F}$ denotes the external body force, which can be gravity, an imposed pressure gradient, the elastic membrane stress, or the regularized surface tension in the application of a continuous surface force model (CSF) [30] for the fluid-fluid interface. In the CSF model, the surface tension effect is included as

$$\mathbf{F} = \sigma\kappa\mathbf{n}\delta(\phi) \tag{2.3}$$

where σ is the constant surface tension, κ and $\mathbf{n}$ are the mean curvature and normal vector of the fluid–fluid interface, respectively, and $\delta(\phi)$ is the regularized Dirac delta function which will be discussed later (Section 2.3).

According to the vector identities, the rate-of-deformation tensor in Eq. (2.1) for an incompressible flow can be expressed as [31]

$$2\nabla \cdot (\mu \mathbf{E}) = \mu \nabla^2 u + \nabla \mu \times \omega + 2\nabla \mu \cdot \nabla u, \tag{2.4}$$

where

$$\omega \equiv \nabla \times u \tag{2.5}$$

is the vorticity. In the present work, the viscosity of each fluid is assumed to be constant. Thus, $\nabla \mu$ is only non-zero near the two-fluid interface and is along the surface normal of interface.

The entire rectangular computational domain, which includes the fluid region and part of the solid region, is discretized on a nonuniform and non-staggered Cartesian grid. For the bulk-fluid region (away from the solid boundary), the governing equation is solved using a variant of Chorin's projection method which involves several sub-steps:

$$\begin{aligned} \rho \frac{\partial u}{\partial t} &= -\nabla P_0 + \nabla \mu \times \omega + \mathbf{F} \\ \frac{\partial u}{\partial t} + (u - \frac{2}{\rho} \nabla \mu) \cdot \nabla u &= \nu \nabla^2 u \\ \rho \frac{\partial u}{\partial t} &= -\nabla p. \end{aligned} \tag{2.6}$$

The first sub-step is treated explicitly, while the advection-diffusion equation in the second sub-step is solved implicitly using the Crank-Nicolson scheme to obtain an intermediate velocity u^*. In the discrete form, this step can be written as

$$\frac{u_i^* - u_i^n}{\Delta t} + \frac{1}{2} \left[\frac{\delta (V_j u_i)^*}{\delta x_j} + \frac{\delta (V_j u_i)^n}{\delta x_j} \right] = \frac{\nu}{2} \left[\frac{\delta}{\delta x_j} \left(\frac{\delta u_i^*}{\delta x_j} \right) + \frac{\delta}{\delta x_j} \left(\frac{\delta u_i^n}{\delta x_j} \right) \right] \tag{2.7}$$

where $\frac{\delta}{\delta x_j}$ represents a second-order central difference scheme,

$$V_j = U_j - \frac{2}{\rho}\frac{\delta\mu}{\delta x_j} \tag{2.8}$$

is the modified velocity component, and U_j is the face-centered velocity obtained by averaging u_j along the j-direction. Note that Eq. (2.7) is a nonlinear equation, and we update U_j^* and V_j^* from available u_i^* in an iterative solution process.

Before solving the third sub-step in Eq. (2.6), the pressure is obtained by requiring the velocity after this step to be divergence-free. Thus,

$$\frac{\delta}{\delta x_j}\left(\frac{\delta p^{n+1}}{\delta x_j}\right) = \frac{\rho}{\Delta t}\frac{\delta U_j^*}{\delta x_j}, \tag{2.9}$$

for which an inhomogeneous Neumann boundary condition,

$$\frac{\partial p}{\partial \mathbf{n}} = -\rho\frac{\mathrm{D}\mathbf{u}}{\mathrm{D}t}\cdot\mathbf{n} \tag{2.10}$$

is assumed and $\mathrm{D}\mathbf{u}/\mathrm{D}t$ stands for the material derivative of the velocity. After the pressure is obtained, the third sub-step in Eq. (2.6) is executed in its discrete form,

$$u_i^{n+1} = u_i^* - \frac{\Delta t}{\rho}\frac{\delta p^{n+1}}{\delta x_i}. \tag{2.11}$$

2.2 Sharp-boundary treatment for the fluid–solid interface

In this work, a previously developed sharp-interface immersed-boundary method [32, 33] is used to handle the complex geometry of the fluid–solid interface. In this method, the irregular solid interface is triangulated by an unstructured surface mesh consisting of a set of Lagrangian marker points. The nodal points on the Cartesian grid that discretizes the computational domain are labeled either as “solid nodes” or “fluid nodes” depending on which side of interface the node is located. Away from the solid surface,

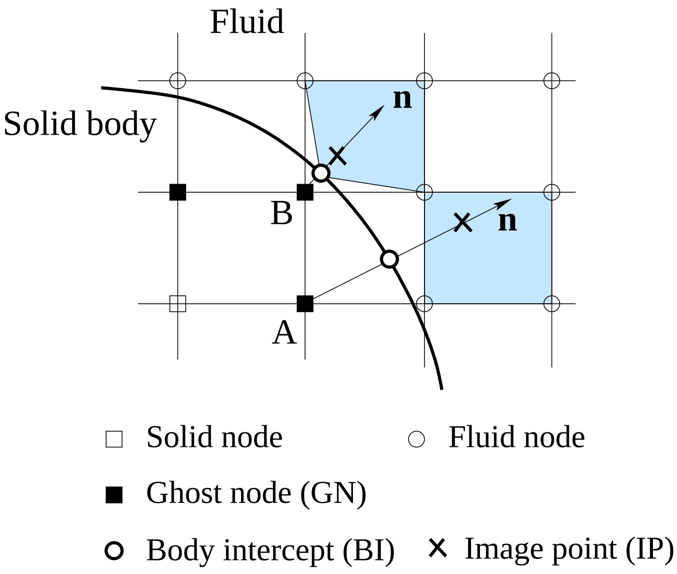

Figure 2.1: Illustration of the sharp-interface immersed-boundary method for the fluid–solid boundary. Flow field extrapolation is applied at the ghost nodes.

the Navier–Stokes equation is discretized using a standard second-order central difference scheme. Such a scheme is also applied at the fluid–fluid interface after the diffuse interface treatment, as will be discussed in next section.

Near the solid surface, the standard central difference scheme cannot be applied for those nodes at which the stencil involves solid nodes. These fluid nodes are immediately next to the solid surface and are termed “hybrid” nodes, and the corresponding solid nodes involved in the stencil are termed “ghost” nodes (GN). Flow field reconstruction is applied at the ghost nodes with the boundary condition incorporated [32]. To accomplish this, the image point (IP) on the fluid side is found by projecting the ghost node along the surface normal, and the body intercept (BI) on the solid surface is thus located midway between the ghost node and image point. Assume that $\phi(x, y, z)$ is a generic variable. To interpolate the value of ϕ at the image point, a trilinear interpolation is used in the local area with eight nodes enclosing the image point,

$$\begin{aligned} \phi(x_1, x_2, x_3) &= C_1 x_1 x_2 x_3 + C_2 x_1 x_2 + C_3 x_2 x_3 + C_4 x_3 x_1 \\ &+ C_5 x_1 + C_6 x_2 + C_7 x_3 + C_8 \end{aligned} \tag{2.12}$$

where the polynomial coefficients $C_i, i = 1, 2, ..., 8$ are determined by the values of ϕ at the eight nodes, ϕ_i,

$$\{C\} = [V]^{-1}\{\phi\}. \tag{2.13}$$

with $\{C\}^T = \{C_1, C_2, ..., C_8\}$ and $\{\phi\}^T = \{\phi_1, \phi_2, ..., \phi_8\}$. The matrix $[V]$ is the Vandermonde matrix constructed from the coordinates of the eight nodes,

$$[V] = \begin{bmatrix} x_1x_2x_3|_{n_1} & x_1x_2|_{n_1} & x_2x_3|_{n_1} & x_3x_1|_{n_1} & x_1|_{n_1} & x_2|_{n_1} & x_3|_{n_1} & 1 \\ x_1x_2x_3|_{n_2} & x_1x_2|_{n_2} & x_2x_3|_{n_2} & x_3x_1|_{n_2} & x_1|_{n_2} & x_2|_{n_2} & x_3|_{n_2} & 1 \\ \vdots & \vdots & \vdots & & & & & \vdots \\ x_1x_2x_3|_{n_8} & x_1x_2|_{n_8} & x_2x_3|_{n_8} & x_3x_1|_{n_8} & x_1|_{n_8} & x_2|_{n_8} & x_3|_{n_8} & 1 \end{bmatrix} \tag{2.14}$$

where the subscripts n_i means the ith node. With the solved coefficients, the trilinear interpolation is complete and the interpolated value at the image point becomes

$$\phi_{\mathrm{IP}}(x_1, x_2, x_3) = \{X\}\{C\} = \{X\}[V]^{-1}\{\phi\} = \sum_{i=1}^{8} \beta_i\phi_i \tag{2.15}$$

where $\{X\} = \{x_1x_2x_3, x_1x_2, x_2x_3, x_3x_1, x_1, x_2, x_3, 1\}|_{IP}$ denotes the vector of coordinates of the image point and β_i is the interpolation weight calculated from $\{X\}[V]^{-1}$. From Eq. (2.15), the interpolation weight β_i depends on the positions of the image point and the eight data points only. Thus, it can be determined once the geometrical information is available and is then ready for use during the iterative solution of the flow variables.

The eight data points used for interpolation could be the eight vertices on the computational cell surrounding the image point. However, the ghost node itself could be one of the eight nodes, as shown by one of the two situations depicted in Fig. 2.1. Under such circumstance, the ghost node is replaced by the body intercept in the interpolation process. At the body intercept, either Dirichlet (for the velocity) or Neumann (for the pressure) condition is specified. For the Dirichlet condition, using the body intercept in the interpolation is straightforward – the interpolation formula, Eq. (2.15), remains the same and the coordinates in X and $[V]$ should be replaced by those for the body intercept. For the Neumann condition, $\partial\phi/\partial n$, needs to be incorporated into the interpolation formula. This is done by modifying the last row of the Vandermonde matrix in Eq. (2.14) into

$$\begin{bmatrix} \frac{\partial(x_1x_2x_3)}{\partial n}\Big|_{n_8} & \frac{\partial(x_1x_2)}{\partial n}\Big|_{n_8} & \frac{\partial(x_2x_3)}{\partial n}\Big|_{n_8} & \frac{\partial(x_3x_1)}{\partial n}\Big|_{n_8} & \frac{\partial x_1}{\partial n}\Big|_{n_8} & \frac{\partial x_2}{\partial n}\Big|_{n_8} & \frac{\partial x_3}{\partial n}\Big|_{n_8} & 0 \end{bmatrix}. \tag{2.16}$$

with the definition of $\partial/\partial n$, Eq. (2.16) can be re-written as:

$$\begin{bmatrix} n_1x_2x_3 + n_2x_1x_3 + n_3x_1x_2 & n_1x_2 + n_2x_1 & n_2x_3 + n_3x_2 & n_1x_3 + n_3x_1 & n_1 & n_2 & n_3 & 0 \end{bmatrix} \tag{2.17}$$

where (n_1, n_2, n_3) represents the normal at node 8. Correspondingly, the last element in ϕ is replaced by $\partial\phi/\partial n$ at the body intercept, and Eq. (2.15) becomes

$$\phi_{\mathrm{IP}}(x_1, x_2, x_3) = \sum_{i=1}^{7} \beta_i\phi_i + \beta_8\frac{\partial\phi}{\partial n}. \tag{2.18}$$

For the velocity boundary condition, a linear distribution is assumed along the line segment connecting the ghost node, body intercept, and the image point. That is,

$$\mathbf{u}_{GN} + \mathbf{u}_{IP} = 2\mathbf{u}_{BI}. \tag{2.19}$$

Given the boundary velocity, $\mathbf{u}_{BI}$, where $\mathbf{u}_{BI} = 0$ for a stationary boundary, $\mathbf{u}_{GN}$ can be calculated from Eq. (2.19). For the pressure, $\frac{\partial p}{\partial n}$ is given as the boundary condition. Using a central difference approximation, the condition can be written as

$$\frac{\partial p}{\partial n}\bigg|_{BI} = \frac{p_{IP} - p_{GN}}{\Delta l} = -\rho\frac{\mathrm{D}u}{\mathrm{D}t}\cdot\mathbf{n}\bigg|_{BI} \tag{2.20}$$

where the Δl is the distance between the IP and GN. Inhomogeneous pressure condition

$\partial p/\partial \mathbf{n} = -\rho(\mathrm{D}\mathbf{u}/\mathrm{D}t)\cdot\mathbf{n}$ has been assumed here. The value of $\mathrm{D}\mathbf{u}/\mathrm{D}t$ at the BI is interpolated from the acceleration of the Lagrangian marker points on the solid surface in the case of a moving boundary.

With the above numerical descriptions of the flow variables at the ghost nodes and the finite-difference discretization at all the fluid nodes, a complete algebraic system could be formed for all the discrete variables. More details of implementation and validation of this sharp-interface treatment are provided in Mittal *et al.* [32]. In the case that the solid surface is a moving boundary, such a method may be subject to numerical oscillations as the solid surface moves across the stationary grid and the ghost nodes have to be re-identified at each time step. To suppress the oscillation, Luo *et al.* [33] improved the method by applying a hybrid numerical description at the fluid nodes immediately next to the solid surface where the finite-difference stencil involves some of the ghost nodes. In the hybrid description, a local interpolation and the standard finite-difference discretization are weighted based on the distance of the fluid node to the solid surface. Thus, as the boundary moves, the interpolation and finite-difference formulas transition to each other gradually rather than abruptly. Since the primary focus of the current work is on stationary solid boundaries, further details of the moving-boundary treatment is not discussed here. Readers are referred to Luo *et al.* [33] for more information.

2.3 Tracking the fluid–fluid interface: the level set method

We consider a viscous incompressible flow of two immiscible fluids in an arbitrary geometry. The level set function[19, 34] is one popular method to implicitly represent the interface between two fluids. In this method, a smooth continuous scalar function ψ is established with zero value on the interface of two fluids, positive in one phase and negative in another (Fig. 2.2). One particular advantage of the level set method is that it can deal with the topological change inherently, for example, coalescence and breakup

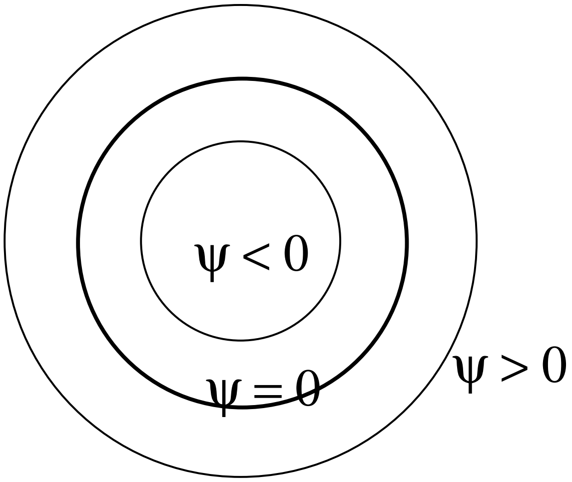

Figure 2.2: The signed distance function as the level set function.

of the interface. The classical level set function is defined as a signed minimum distance function:

$$\psi(\mathbf{x}) \equiv \text{dist}(\mathbf{x}) = \min(|\mathbf{x} - \mathbf{x}_I|), \qquad \mathbf{x} = \{x_1, x_2, x_3\}, \qquad \mathbf{x}_I \in \partial\Omega \tag{2.21}$$

where $\partial\Omega$ is the interface. $\psi(\mathbf{x}) = 0$ represents the position of the interface, while $\psi(\mathbf{x}) > 0$ for $\mathbf{x} \in \partial\Omega^+$ and $\psi(\mathbf{x}) < 0$ for $\mathbf{x} \in \partial\Omega^-$. This definition maintains the feature $|\nabla\psi| = 1$ inside the entire domain. As a continuous function, ψ has adequate smoothness that the normal $\mathbf{n}$ and curvature κ of the interface can be directly computed from ψ,

$$\mathbf{n} = \frac{\nabla\psi}{|\nabla\psi|}, \qquad \kappa = -\nabla \cdot \mathbf{n}. \tag{2.22}$$

These two quantities are used in the calculation of the surface tension force in Eq. (2.3).

Under the fluid velocity field, the standard equation for convecting the level set function is given as

$$\frac{\partial\psi}{\partial t} + \mathbf{u} \cdot \nabla\psi = 0. \tag{2.23}$$

Thus the zero level of distance function, or the interface, will be transported along with the local fluid. Since the density and viscosity remain constant in each fluid phase, they can be written with the Heaviside function as

$$\begin{aligned}\rho &= \rho_1 + (\rho_2 - \rho_1)H(\phi) \\ \mu &= \mu_1 + (\mu_2 - \mu_1)H(\phi) \qquad (2.24)\end{aligned}$$

where the subscript indicates the phase 1 or 2. To regularize the discontinuous Heaviside function, the following approximation is used instead,

$$H(\psi) = \begin{cases} 0, & \psi < -\epsilon \\ \frac{\epsilon+\psi}{2\epsilon} + \frac{1}{2\pi}\sin\left(\frac{\pi\phi}{\epsilon}\right), & -\epsilon \le \psi \le \epsilon \\ 1, & \epsilon < \psi \end{cases} \qquad (2.25)$$

where ϵ is the parameter that determines the bandwidth of the smeared interface. Typically ϵ varies from one to two grid intervals around the interface. The regularized Heaviside function is also used to derive the approximate Dirac delta function in Eq. (2.3),

$$\delta(\psi) = H'(\psi) = \begin{cases} 0, & \psi < -\epsilon \\ \frac{1}{2\epsilon} + \frac{1}{2\epsilon}\cos\left(\frac{\pi\psi}{\epsilon}\right), & -\epsilon \le \psi \le \epsilon \\ 0, & \epsilon < \psi \end{cases} \qquad (2.26)$$

Thus, $\delta(\psi)$ is equal to zero elsewhere except within the thickness of the diffuse interface.

When solving the advection equation (2.23), the distance function will be distorted and the smoothness of ψ may be lost, which leads to inaccuracy of the geometrical quantities and even numerical instabilities at the interface [34](Chapter 7). To keep ψ smooth and a meaningful distance function, re-initialization of the signed distance profile is enforced in the vicinity of the zero-level contour every a few time steps. The usual re-initialization step is to solve a Hamilton-Jacobi equation

$$\frac{\partial\psi}{\partial\tau} + S(\psi_0)(|\nabla\psi| - 1) = 0, \tag{2.27}$$

where $S(\psi_0)$ is a sign function taking 1 in Ω^+, -1 in Ω^-, and 0 on the interface, and τ is the pseudo time. Numerically, $S(\psi_0)$ is also smoothed to increase the stability,

$$S(\psi_0) = \frac{\psi_0}{\sqrt{\psi_0^2 + (\Delta x)^2}} \tag{2.28}$$

where ψ_0 is the initial value of ψ at the beginning of each re-initialization iteration and Δx is the mesh interval. After a few iterations in the pseudo time, Eq. (2.27) can reach the steady state, where the $\partial\psi/\partial\tau$ approaches zero and $|\nabla\psi|$ is equal to one.

The advection equation, Eq. (2.23), is a special kind of Hamilton-Jacobi equation [35], and many numerical algorithms, e.g., the 3rd-order ENO (Essentially Non-Oscillatory) and the 5th-order WENO (Weighted ENO), have been developed to solve (2.23) and (2.27), which can achieve high-order accuracy and robustness. The ENO introduced by Harten et al. [36] increases the accuracy of approximation for ψ_x^- and ψ_x^+ significantly, where ψ_x^- and ψ_x^+ are the approximate $\partial\psi/\partial x$ on a left- and right-biased stencil in the x-direction, respectively. Its basic idea is to reconstruct ψ using a high-order polynomial on a four-point stencil and then differentiate the polynomial to approximate ψ_x. The stencils for the ENO are tabulated in [37]. Based on the ENO, the WENO [38, 39] is a convex combination of three overlapping ENO stencils to achieve the 5th-order accuracy. In the current work, we have implemented the WENO to solve Eq. (2.27).

Three possible ENO approximations to $(\psi_x^-)_i$ can be calculated on the stencil supported by the nodes $\{x_{i-3}, x_{i-2}, ..., x_{i=2}\}$ [34] as

$$\begin{aligned}
\psi_x^1 &= \frac{v_1}{3} - \frac{7v_2}{6} + \frac{11v_3}{6} \\
\psi_x^2 &= -\frac{v_2}{6} + \frac{5v_3}{6} + \frac{v_4}{3} \\
\psi_x^3 &= -\frac{v_3}{3} + \frac{5v_4}{6} - \frac{v_5}{6}
\end{aligned} \tag{2.29}$$

where $v_1 = (\psi_{i-2} - \psi_{i-3})/\Delta x$, $v_2 = (\psi_{i-1} - \psi_{i-2})/\Delta x$,..., $v_5 = (\psi_{i+2} - \psi_{i+1})/\Delta x$. The WENO consists of a convex combination of the approximation in Eq. (2.30) as

$$\psi_x = \omega_1\psi_x^1 + \omega_2\psi_x^2 + \omega_3\psi_x^3 \tag{2.30}$$

where ω_k are the weights satisfying $\omega_1 + \omega_2 + \omega_3 = 1, 0 \leq \omega_k \leq 1$. The weights are defined as follows [40] to estimate the stencil smoothness:

$$\begin{aligned}
S_1 &= \frac{13}{12}(v_1 - 2v_2 + v_3)^2 + \frac{1}{4}(v_1 - 4v_2 + 3v_3)^2 \\
S_2 &= \frac{13}{12}(v_2 - 2v_3 + v_4)^2 + \frac{1}{4}(v_2 - v_4)^2 \\
S_3 &= \frac{13}{12}(v_3 - 2v_4 + v_5)^2 + \frac{1}{4}(3v_3 - 4v_4 + v_5)^2
\end{aligned} \tag{2.31}$$

Then, we define

$$\begin{aligned}
\alpha_1 &= \frac{0.1}{(S_1 + \epsilon)^2} \\
\alpha_2 &= \frac{0.6}{(S_2 + \epsilon)^2} \\
\alpha_3 &= \frac{0.3}{(S_3 + \epsilon)^2},
\end{aligned} \tag{2.32}$$

where $\epsilon = 10^{-6}\max\{v_1^2, v_2^2, v_3^2, v_4^2, v_5^2\} + 10^{-99}$. By normalizing α_k, we obtain the weights from

$$\omega_i = \frac{\alpha_i}{\alpha_1 + \alpha_2 + \alpha_3}, i = 1, 2, 3. \tag{2.33}$$

2.3.1 Mass conservation

One challenging issue for the level set method is the mass conservation problem. Mass gain/loss during update of the two-fluid interface causes a crucial impact to the accuracy of the method. The mass conservation problem has been discussed frequently in literature [41–45]. Spelt [46] utilized a simple correction method to compensate the mass loss,

$$\tilde{\psi} = \psi + \frac{V - V_0}{2S} \tag{2.34}$$

where V is the volume of one phase, V_0 is the initial value of the same phase, and S is the area of the interface. Both V and S can be determined straightforwardly from the Heaviside and $\delta(\psi)$ functions. The correction of the fluid volumes is applied at the end of each convection step in Eq. (2.23). This treatment exactly conserves the volumes of the two fluids and does not have a significant effect on the non-physical interface displacement [47]. Therefore, we have implemented it in the current method.

2.3.2 Curvature smoothing

In the CSF model expressed by Eq. (2.3), the surface tension force is calculated based on the surface normal **n** and the curvature κ. However, the computation of the curvature is prone to numerical noise, which could cause inaccuracy and failure of the surface force model. Previously, smoothing kernels or operators have been applied to the level set method and volume-of-fluid (VOF) method [48, 49] to counteract the numerical instability. Recently, Chiu & Lin [50] employed a Helmholtz smoother to stabilize the calculation of the curvature. This smoother is adopted in the current work and is described here as

$$H = 1 - \epsilon^2 \nabla^2, \tag{2.35}$$

Where ϵ is a constant parameter. Apply this operator and solve the Helmholtz equation

$$\psi = H(\tilde{\psi}) = \tilde{\psi} - \epsilon^2 \nabla^2 \tilde{\psi}, \tag{2.36}$$

then we obtain the smoothed function $\tilde{\psi}$. The curvature κ can then be calculated from $\tilde{\psi}$ using a 2nd-order central difference scheme,

$$\kappa = \nabla \cdot \mathbf{n} = \nabla \cdot \left(\frac{\nabla \tilde{\psi}}{\left| \nabla \tilde{\psi} \right|} \right). \tag{2.37}$$

Fig. 2.3 shows the comparison between the smoothed and non-smoothed curvature computation. In this test, a 2D droplet with a radius $0.5d$ is placed in the Poiseuille flow originally at the center of the domain that has dimension of $[-d, d] \times [-d, d]$. Here d is the half channel width. A uniform grid of 200×200 points is used to discretize the domain, and the time step is chosen to be $\Delta t = 10^{-3} d/U$. The inlet boundary is at $x = -d$, and the outlet at $x = d$. The Reynolds number is $Re = \rho U d/\mu = 1$, where U is the centerline velocity of the Poiseuille flow. Fig. 2.3 shows the level set contour and the corresponding curvature at two different time instances, $tU/d = 0.1$ and 0.2. At both time moments, the smoothing treatment does not cause significant difference in the level set contours. However, oscillations can be clearly seen at top and bottom sides of the contours of the curvature for the non-smoothed calculation. In comparison, the curvature from the smoothed calculation has a stable solution and much smoother contours.

The parameter ϵ affects the strength of curvature smoothing. Here we choose $\epsilon = k\Delta x$, where Δx is the grid interval. After several tests with the droplet in the Poiseuille flow, we set $k = 5$, which gives a reasonable result.

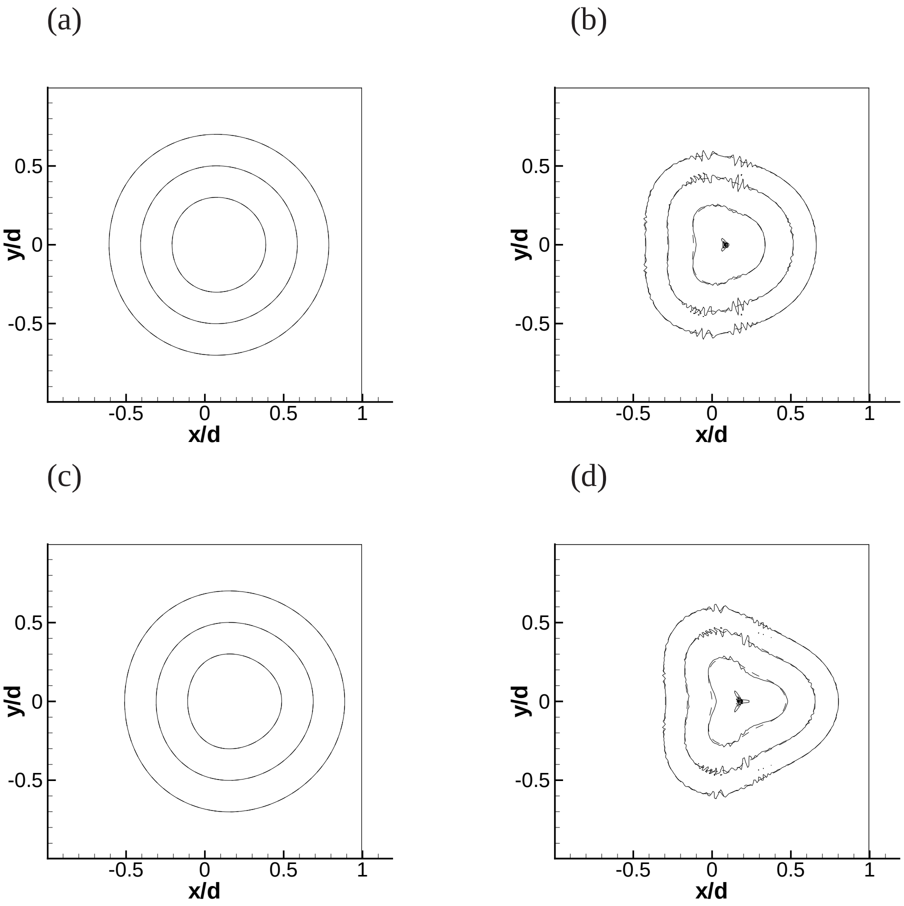

Figure 2.3: Effect of curvature smoothing for an initially cylindrical droplet placed in a channel flow at time (a,b) $tU/d = 0.1$ and (c,d) $tU/d = 0.2$. (a,c) The level set contours; (b,d) contours of the curvature calculated from the level set function. The solid lines are from the non-smoothing treatment, and the dashed lines from the smoothing treatment.

CHAPTER 3

EFFECT OF WING INERTIA ON HOVERING PERFORMANCE OF FLEXIBLE FLAPPING WINGS

3.1 Background

Aerodynamics of insect flight (Fig. 3.1) has drawn considerable attention in recent years due to its promising application in the development of biomimetic micro air vehicles [5]. During flight, insect wings typically experience dynamic deformations [6], i.e., change of the wing shape from its rest configuration regardless the position or orientation of the wing. Even though the deformation magnitude and pattern vary from species to species, physiological studies have shown that insect wings do not possess an internal actuation mechanism and thus the deformation has to be passive [7]. That is, an insect wing is deformed by either the aerodynamic force from the surrounding air, or the inertial acceleration, or a combination of both.

The structural deformation during flapping may significantly change the flow behavior around the wing and consequently have an important effect on its aerodynamic performance. A few studies have been devoted to the understanding of the effect of the wing flexibility. Using a two-link model representing a chordwise wing section, Vanella *et al.* [51] performed a two-dimensional numerical simulation of the flow–structure interaction in hovering flight. They found that the structural flexibility can enhance the aerodynamic performance of the wing by increasing the lift-to-drag and lift-to-power ratios, and that the best performance is obtained when the flapping frequency is a fraction of the natural frequency of the wing structure. In a separate study using also the linkage model, Eldredge *et al.* [52] investigated the effect of the wing flexibility in a range of kinematic parameters describing the combined pitching and heaving motion of the wing. They found that a mildly flexible wing has consistently good performance over a wide range of phase differences between pitching and heaving, which is in contrast with the relative sensitivity of a rigid wing to this parameter. Full three-dimensional numerical simulations of the desert locust, *Schistocerca gregaria*, were recently performed by reconstructing the detailed wing kinematics, including the time-varying camber and spanwise twist of the wing surface, from the high-speed digital video of the real insect flight [53]. By comparing the performance of the wing model based on the fully reconstructed kinematics and that of the corresponding wing models without the camber or twist, Young *et al.* [53] found that the wing deformation leads to substantial power economy in lift production. Meanwhile, they noticed that the leading edge vortex remains attached to the wing during the entire flapping cycle in the full-kinematics model, which may have contributed to the aerodynamic power efficiency of the wing. The aerodynamic advantage of the passive wing flexibility was also reported for the biomimetic wings that are designed to produce characteristic deformation patterns of insects or birds [54].

In insect flight, both the inertial force and the fluid force can be the primary causes of the wing deformation. Combes & Daniel [55] compared vibrations of the excited hawkmoth *Manduca sexta* wing in normal air and in helium (approximately 15% of the air density) and noticed that the difference in the wing deformation pattern between the two cases is very small. Their result suggests that the *Manduca* wing deformation is mainly due to the inertia force of the wing. In another study, Chen *et al.* [56] performed a vibration test of the dragonfly wing and found that the lowest frequency among the natural vibration modes is on order of 170 Hz, which is much higher than the flapping frequency of the insect. Therefore, they concluded that the wing inertia is small compared to the elastic force for the dragonfly and the wing deformation is mainly due to the aerodynamic force.

From the aeroelasticity point of view, whether the wing deformation is caused by the wing inertia or the fluid force will not only affect the deformation pattern but also

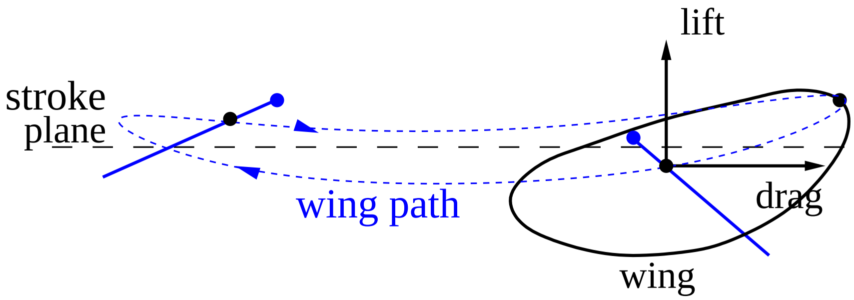

Figure 3.1: Illustration of the wing motion during hovering flight of an insect.

change the phase of the wing deflection during a flapping cycle. It is therefore worthwhile to investigate the aerodynamic consequences of this issue. Since both situations exist in insect flight, as seen in the hawkmoth and dragonfly, investigation of this issue may provide some biomechanical insight into the morphological differences between these insect wings. To address the problem, we have performed a two-dimensional numerical simulation of the flow–structure interaction in hovering flight and have systematically studied the effect of the mass ratio of the wing, defined as

$$m^* = \frac{\rho_s h}{\rho_f c} \tag{3.1}$$

where $\rho_s h$ is the surface density of the wing, ρ_f is the density of the air, and c is the characteristic length of the wing. The deformable wing section is represented by an elastic plate which may undergo large displacements. Therefore, the wing model in the present study has infinite degrees of freedom and can have a smooth camber, as opposed to the previous linkage models [51, 52].

Note that experimental measurements of the aerodynamic force in insect flight are typically carried out in water or oil in order to scale up the size of the wing model while keeping the Reynolds number in the physiological regime [57–59]. In that case, the hydrodynamic pressure is much higher than the inertial force of the wing. Therefore, the effect of the wing inertia could not be addressed in those studies. We also point out that the effect of the wing inertia was a topic in a few previous theoretical studies [60, 61].

However, these works mainly focused on the thrust generation, not lift production, of the flexible wings. Furthermore, in Zhu [60] only potential flow is assumed and the viscous effects including flow separation are completely omitted. Michelin & Smith [61] introduced point vortices into their inviscid flow model to account for the vortex shedding effect, but the stroke distance of the wing is very small compared to the chord length and flow separation at the leading edge is not included.

3.2 Problem formulation

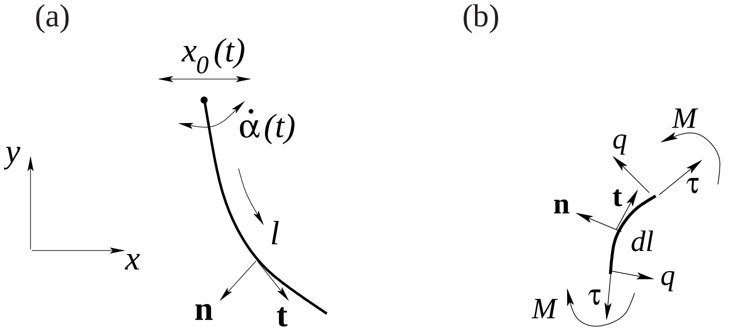

Figure 3.2: (a) A schematic of the wing section during hovering flight. (b) A wing segment illustrating the in-plane tension τ, the transverse stress q, and the bending moment M.

We consider a two-dimensional hovering wing section with the chord length c, as shown in Fig. 3.2(a). The wing undergoes a combined translational and rotational motion specified at the leading edge [62, 63],

$$x_0(t) = \frac{A_0}{2}\cos(2\pi f t) \tag{3.2}$$

$$\alpha(t) = \alpha_0 + \beta\sin(2\pi f t + \phi) \tag{3.3}$$

where $x_0(t)$ is the horizontal position of the leading edge, $\alpha(t)$ is the angle between the leading edge and the horizontal axis (measured in the counterclockwise direction), A_0 is the stroke distance of the leading edge, α_0 is the initial orientation, β is the angle amplitude, f is the flapping frequency, and ϕ is the phase difference between the rotation and translation. In the present work, we choose $\alpha_0 = -\frac{\pi}{2}$ and $\phi = 0$, which corresponds to the symmetrical rotation [62].

The wing chord is assumed to be elastic and nearly inextensible, and its dynamics is governed by the nonlinear equation

$$\rho_s h \frac{\mathrm{d}^2\mathbf{x}}{\mathrm{d}t^2} = \frac{\partial}{\partial l}(\tau \mathbf{t} + q\mathbf{n}) + \mathbf{f}, \tag{3.4}$$

where ρ_s and h are density and thickness of the wing, respectively, $\mathbf{t}$ is the unit tangent vector pointing in the direction of increasing arc length, l, from the leading edge, $\mathbf{n}$ is the unit normal vector, and $\mathbf{f}$ is the difference between the distributed loads on the two sides of the wing. The in-plane tension, τ, is assumed to be proportional to the tangential strain so that

$$\tau = E_S \left(\left| \frac{\partial \mathbf{x}}{\partial l_0} \right| - 1 \right) = E_S \left(\left| \frac{\partial l}{\partial l_0} \right| - 1 \right), \tag{3.5}$$

where E_S is the stretching coefficient of the plate, and l_0 is the arc length in the unstretched state. The transverse stress, q, is linearly related to the bending moment, M, by

$$q = \frac{\partial M}{\partial l} = \frac{\partial (E_B \kappa)}{\partial l}, \tag{3.6}$$

where E_B is the bending modulus, and κ is the curvature [64]. The boundary conditions at $l = 0$ include the specified position and orientation, i.e.,

$$\mathbf{x} = \mathbf{x}_0(t), \qquad \frac{\partial \mathbf{x}}{\partial l} = (\cos\alpha, \sin\alpha). \tag{3.7}$$

At the trailing edge, $l = c$, both the bending moment and the transverse stress vanish, which requires $\kappa = 0$ and $\partial\kappa/\partial l = 0$. Therefore, we have

$$\frac{\partial^2 \mathbf{x}}{\partial l^2} = 0, \qquad \frac{\partial^3 \mathbf{x}}{\partial l^3} = 0. \tag{3.8}$$

The flow is governed by the viscous incompressible Navier–Stokes equation and the continuity equation,

$$\begin{aligned} \frac{\partial v_i}{\partial t} + \frac{\partial v_j v_i}{\partial x_j} &= -\frac{1}{\rho_f}\frac{\partial p}{\partial x_i} + \nu_f \frac{\partial^2 v_i}{\partial x_j^2}, \\ \frac{\partial v_i}{\partial x_i} &= 0, \end{aligned} \tag{3.9}$$

where v_i is the velocity, ρ_f and ν_f are the fluid density and viscosity, and p is the pressure. No-slip and no-penetration conditions are specified at the flow–solid boundary. To parametrize the system, we define the non-dimensional groups including the normalized wing stroke, Reynolds number, mass ratio, and frequency ratio, which are given by

$$\frac{A_0}{c}, \quad Re = \frac{\pi A_0 f c}{\nu_f}, \quad m^* = \frac{\rho_s h}{\rho_f c}, \quad \omega^* = \frac{\omega_f}{\omega_n} = \frac{2\pi f}{\omega_n} \tag{3.10}$$

respectively, where $\omega_f = 2\pi f$, and

$$\omega_n = \frac{k_n^2}{c^2}\sqrt{\frac{E_B}{\rho_s h}} \tag{3.11}$$

with $k_n = 1.8751$ is the frequency of the first natural vibration mode of the wing [65]. Physically, m^* represents the ratio between the inertial force of the wing and the aerodynamic pressure, and ω^* represents the wing rigidity.

The equations governing the system, (3.4) and (3.9), are solved numerically in an implicitly coupled manner using an in-house solver. Specifically, the incompressible flow is solved using a sharp-interface immersed-boundary method [32, 66] with a special treatment to suppress the pressure oscillations associated with the moving boundaries [67]. In this method, a single-block Cartesian grid is used to discretize the Navier–Stokes equation on a rectangular domain, and the ghost nodes and hybrid nodes are defined near the fluid–solid interface to facilitate the boundary treatment at the interface. The infinitely thin membranous wing is augmented with an artificial thickness that is about three times the spacing of the Cartesian grid and is automatically reduced as the grid is refined. The wing section is discretized by a set of Lagrangian points initially distributed uniformly along the wing. A standard central finite difference scheme is used to discretize Eqns. (3.4) to (3.8), and Eq. (3.4) is solved iteratively as an inner loop embedded within the implicit algorithm for the flow–structure interaction. The flow–structure interaction is solved at each time step by iterating the flow and the structural dynamics until convergence is reached [67].

3.3 Validation of the numerical method

The simulation of the unsteady flow around a thin and rigid wing is compared with previous results in [63]. In this test, the wing rotates around its center, whose stroke distance is denoted by A_0. The parameters are otherwise defined in the same way as in Section 3.2. To match the simulation setup, $A_0/c = 2.8$ and $\beta = \pi/4$ are chosen for the wing kinematics, and the Reynolds number is $Re = 75$. The flow is initially quiescent. The lift and drag coefficients for first a few cycles are shown in Fig. 3.3. It can be seen that the present simulation has very good agreement with that in [63] where a vortex particle method was used.

The structural solver is validated by comparing the numerical simulation of the small-amplitude vibration in vacuum with the eigenmodes of the wing structure. To do this, a sinusoidal translation is specified at the leading edge and the amplitude of translation is much smaller than c. The structural dynamics is simulated in the absence of the fluid so that there is no damping mechanism. The frequency of the actuation is chosen to be either the first or second eigenfrequency of the corresponding cantilever

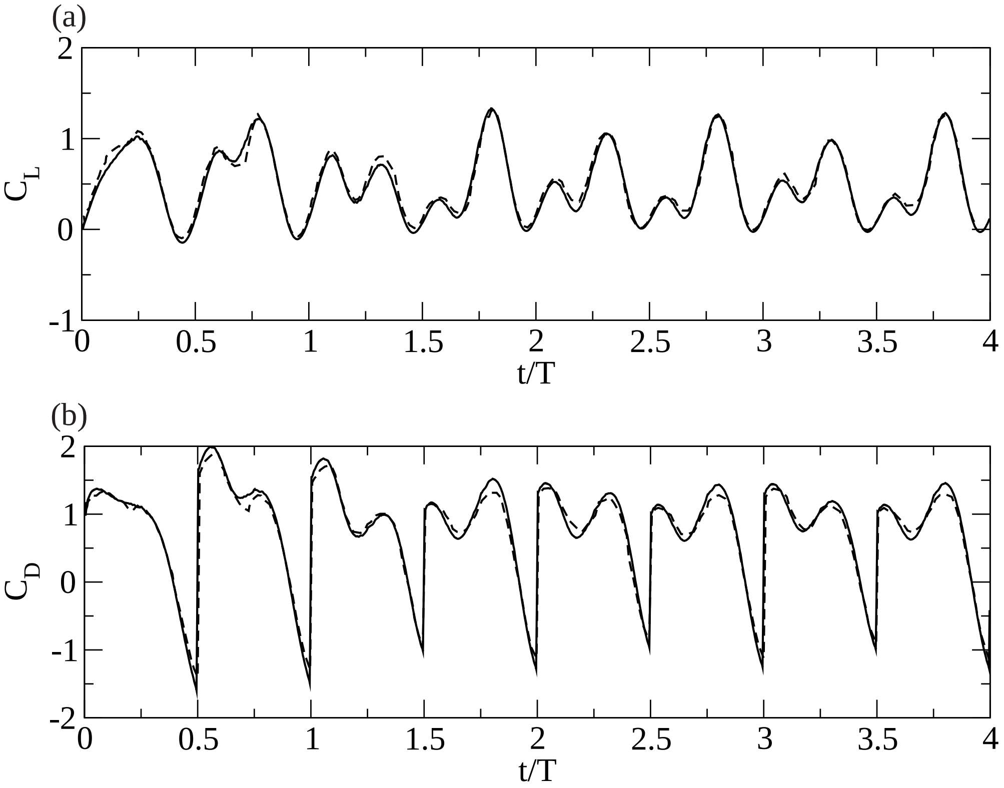

Figure 3.3: (a) Lift and (b) drag coefficients (defined in the same way as in Section 3.5) from the present simulation (solid) and from [63] (dashed).

beam [65]. Figure 3.4 shows the simulation vibration mode together with the analytical eigenfunctions. For the first mode, 20 nodes on the wing are sufficient to capture the deformation pattern accurately. For the second mode, a 100-node mesh leads to a satisfactory solution. In the flow–structure simulations presented here, 100 nodes are used in all cases.

3.4 Simulation setup

In the present simulations, we choose the stroke distance $A_0/c = 2.5$, Reynolds number $Re = 150$, and rotational angle $\beta = 0$, or $\beta = \pi/8$. The parameters describing the wing kinematics are selected based on previous work on insect flight [51, 62, 63]. Three mass ratios are considered, $m^* = 1$, 5 and 25, which represent the light, medium, and heavy wing, respectively. For each of these mass ratios, the frequency ratio ω^* is

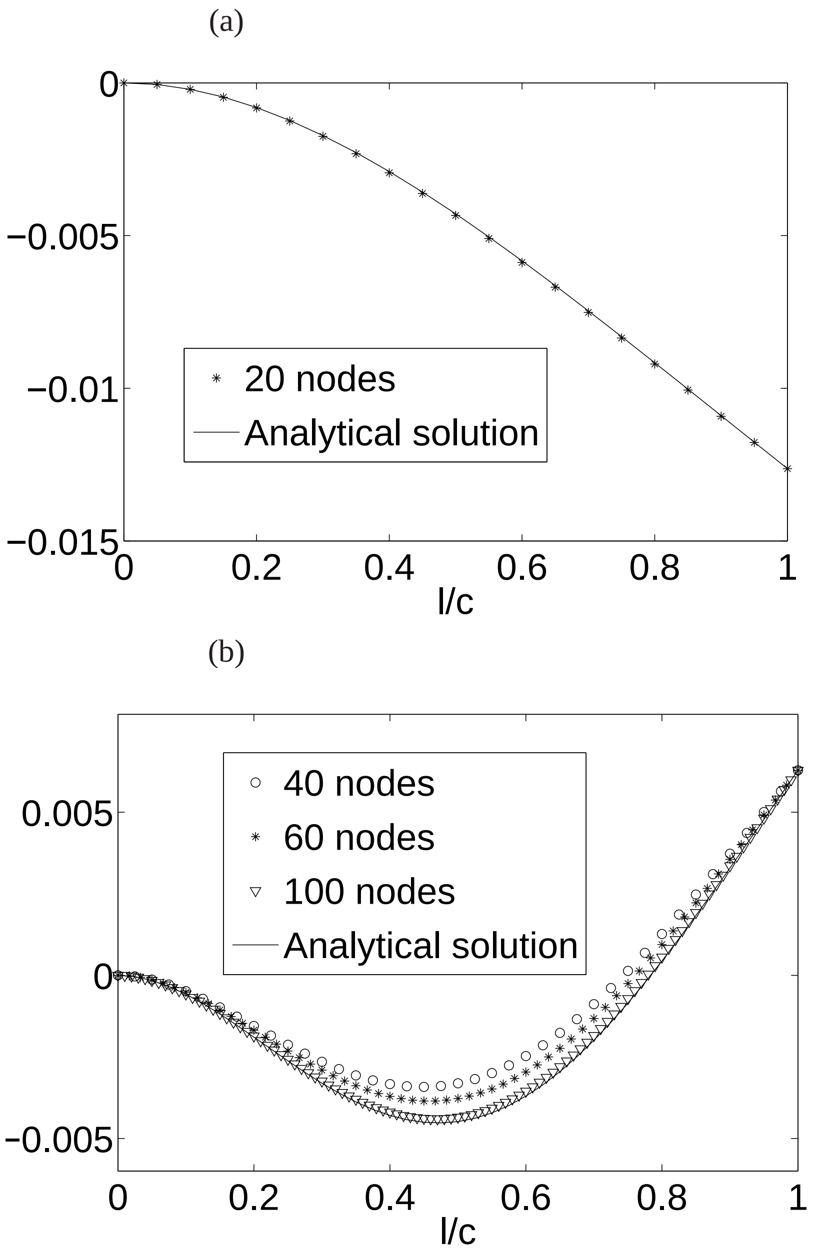

Figure 3.4: Comparison of the simulated vibration mode with the eigenmode. (a) The first mode; (b) the second mode.

chosen to vary among 1/1.25, 1/1.5, 1/2, 1/2.5, 1/3, 1/4, 1/6, and 0, where $\omega^* = 1/1.25$ means that the wing is most flexible and flaps near the resonant frequency, and $\omega^* = 0$ means that the wing is rigid.

The computational domain (Fig. 3.5) has a size of $20c \times 35c$. We have done extensive tests to make sure that the domain is large enough to achieve satisfactory accuracy of the results. The entire domain consists of a nonuniform Cartesian grid of 320×448 points. The grid contains a horizontal band and a vertical band of width $3c$ in which the grid points are uniformly and densely distributed such that the grid spacings $\Delta x = \Delta y = 0.02c$. A total number of 100 nodes are used to discretize the wing and its governing equation. The time step size is $\Delta t = 0.0025T$ where $T = 1/f$ is the period of a flapping cycle. The flow solver and the structure solver have been validated separately as shown in Section 3.3. In addition, grid refinement has been performed to make sure that the simulation results are grid-independent.

3.5 Flexible translating wings without rotation

We first consider the flexible wing driven by the pure translation, i.e., $\beta = 0$, at the leading edge where the wing is clamped. Therefore, the wing has to rely on its deflection to generate a non-zero lift. Fig. 3.6(a) shows the lift coefficient,

$$C_L = 2F_L/(\rho_f U^2 c) \tag{3.12}$$

averaged from 15 flapping cycles, where F_L is the total lift and $U = \pi A_0 f$ is the maximum translational velocity of the leading edge. The result is shown for the mass ratio $m^* = 1, 5, 25$ and frequency ratio ω^* from 0 to 0.8. Two interesting phenomena can be observed from this figure. First, for each mass ratio there is a particular frequency ratio at which the lift force peaks. The peak lift coefficients for the three mass ratios are very close to each other, and all are around 0.9. Second, this particular frequency

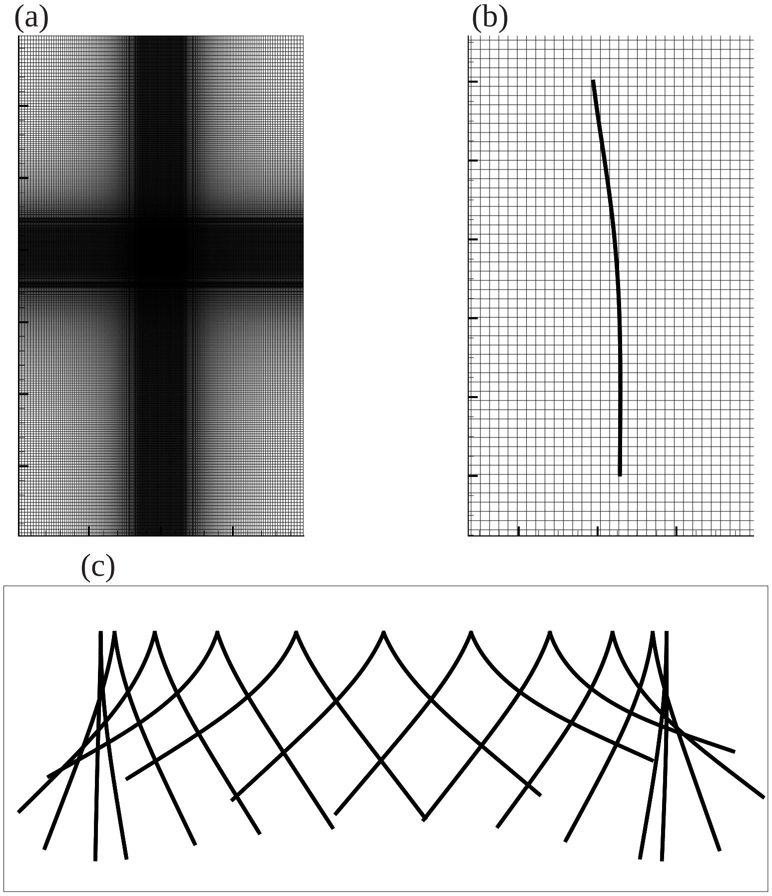

Figure 3.5: (a) The computational domain with strecthed structural mesh; (b) Immersed flexible wing; (c) One flapping cycle.

ratio depends on the mass ratio of the wing. For $m^* = 25$, C_L peaks at $\omega^* = 0.8$. For $m^* = 5$ and 1, the peaks of C_L are shifted to the left, taking place at $\omega^* = 0.5$ and 0.4, respectively. That is, as the mass ratio is reduced, the frequency ratio for the peak lift also decreases. Physically, this result means that for the heavy wing (large m^*), flapping near the resonant frequency produces higher lift, and for the light wing (small m^*), flapping at a frequency much lower than the resonant frequency would produce higher lift. To understand this result, we point out that when the mass ratio is large, the fluid force becomes insignificant compared to the wing's inertial force, and the flapping actuation has to be close to the natural vibration mode in order to produce significant wing deformations for lift production. On the other hand, when the mass ratio is low, the wing is deformed by the fluid force, and a lower flapping frequency would suffice to produce the necessary deformation. If the flapping frequency is too high in the case of low m^*, the wing deformation may become exceedingly large, and the lift would drop as shown in Fig. 3.6(a) for large ω^*.

Figure 3.6(b) shows the drag coefficient defined as

$$C_D = 2F_D/(\rho_f U^2 c) \tag{3.13}$$

averaged over the 15 flapping cycles. Here F_D is the total horizontal fluid force on the wing defined to be positive when it is against the translational motion of the leading edge. This force can be temporarily negative in a cycle due to the wing deformation, as seen later. For $m^* = 25$ and 5, the average C_D changes approximately within 20% as ω^* is varied. For $m^* = 1$, the average C_D decreases drastically from 2.76 to 0.69 as ω^* is increased from 0 to 0.8, and the drag is generally much lower than the other two wings with the same rigidity. Such a drag reduction is because the light wing is deflected by the fluid force and its shape is adapted to the drag by reducing the frontal area. When ω^* is large and the wing is more flexible, this self-adaptation effect becomes more pronounced. On the other hand, when ω^* goes zero, that is, the wing behaves essentially as a rigid plate, the lift coefficient vanishes and the drag coefficient approaches the same constant for all the mass ratios as expected. Note that in the cases of $m^* = 25$ and 5, the average drag of a flexible wing ($\omega^* > 0$) can be higher than that of a corresponding rigid wing ($\omega^* = 0$), which indicates that the inertia-dominated deformation may substantially augment the drag force.

The dependence of the lift-to-drag ratio on m^* and ω^* is shown in Fig. 3.6(c). It can be seen that the low-mass wings clearly out-perform the high-mass wings when the wing rigidity is the same. For $m^* = 25$, the lift-to-drag ratio increases nearly monotonically as ω^* is raised and the wing becomes more flexible; for $m^* = 5$, this ratio increases first and then reaches a plateau of 0.31; and for $m^* = 1$, the lift-to-drag ratio first increases, then reaches a peak of 0.56 around $\omega^* = 0.6$, and finally drops as ω^* is further raised.

To analyze the power consumption, we first define the net power $P(t)$ as

$$P(t) = F_x \dot{x}_0 + M_z \dot{\alpha} \tag{3.14}$$

where F_x and M_z are the total force and total torque, respectively, applied at the leading edge to actuate the wing. Note that the second term is zero when the wing has no active rotation. Next we adopt a conservative assumption that the negative power in the either one of the two terms in (3.14) is not reusable. Therefore, we define an alternative power measurement, $\hat{P}$, which represents only the positive contributions from the two terms in (3.14). The averaged net and modified power coefficients, C_P and $C_{\hat{P}}$, defined as the power normalized by $(1/2)\rho_f U^3 c$, are plotted in Figs. 3.6(d) and (e), respectively. For all three mass ratios, the two power measurements overall exhibit a similar trend. For $m^* = 25$ and 5, the net power coefficient increases up to 4.2 and 3.0, respectively, as ω^* is raised, which indicates a significant energy loss due to the large wing deformation. The instantaneous power consumption, as plotted in Fig. 3.7(d) for $\omega^* = 0.5$, shows that at these two mass ratios, the net power fluctuates at a large amplitude in a flapping cycle because the energy changes its form between the kinetic energy of the wing and the elastic potential stored in the wing. Therefore, if the negative power is not reusable as assumed for the modified power, a large portion of the input energy would be lost. This effect is reflected in Fig. 3.6(e), where the $m^* = 25$ wing requires a much higher modified power than the other two wings. Especially when the wing rigidity is low, the modified power coefficient reaches an amount of 12 for $m^* = 25$. On the other hand, for $m^* = 1$, the modified power coefficient is close to the net power coefficient, and both in general decrease as the wing becomes more flexible. As seen in Fig. 3.7(d) for $\omega^* = 0.5$, the instantaneous power coefficient at this mass ratio is almost always positive, and its magnitude is much smaller than that for $m^* = 5$ and 25. Figs. 3.6(d) and (e) show that the average power consumption for $m^* = 1$ is lowest among the three mass ratios. This result is understandable since the wing with $m^* = 1$ experiences a smaller drag resistance compared to the other two wings. The power economy of the low-mass wing is further seen in Fig. 3.6(f), where the ratio between the average lift coefficient and the average modified power coefficient is shown. For the same amount of power input, the wing with $m^* = 1$ may produce more than twice amount of lift than the other two wings. The peak performance for $m^* = 1$ is around 0.58, which takes place at $\omega^* = 0.5$.

We select a specific frequency ratio, $\omega^* = 0.5$, to analyze the details of the force characteristics and flow field. From Fig. 3.6, the wing flexibility at this frequency ratio has nearly the best lift-to-modified-power performance for all three mass ratios. Figure 3.7(a) shows the x-component of the displacement of the wing tail with respect to its undeformed configuration for $m^* = 25$, 5, and 1. At this frequency ratio, the maximum displacement is more than 50% of the chord length in all three cases, while the wing with $m^* = 1$ has largest amplitude. The positions of the positive and negative peaks in the displacement indicate that there is a significant phase difference among the three cases. For $m^* = 25$, the maximum displacement almost always takes place at the stroke reversals, e.g., $t/T = 12.0, 12.5, 13.0, \ldots$, and so on. For $m^* = 1$, there is a phase delay of approximately $\pi/4$ in the maximum displacement. In addition, the wing displacement in this case becomes highly asymmetric between the forward and backward strokes, as indicated by the appearance of two peaks in the first half-stroke. This interesting deformation pattern will be discussed later together with the flow field.

Figures 3.7(b) and (c) show the corresponding lift and drag coefficients to the wing displacement shown in Fig. 3.7(a). The two heavy wings, especially $m^* = 25$, produce a large amount of negative lift every time after the wing passes the middle point of the stroke, at which the wing has recovered to from its deformation and is overshooting and bending forward. In comparison, the light wing with $m^* = 1$ has typically a non-negative lift coefficient throughout the multiple flapping cycles. In the drag history, the two heavy wings cause much higher drag than the light wing, and the peak drag takes

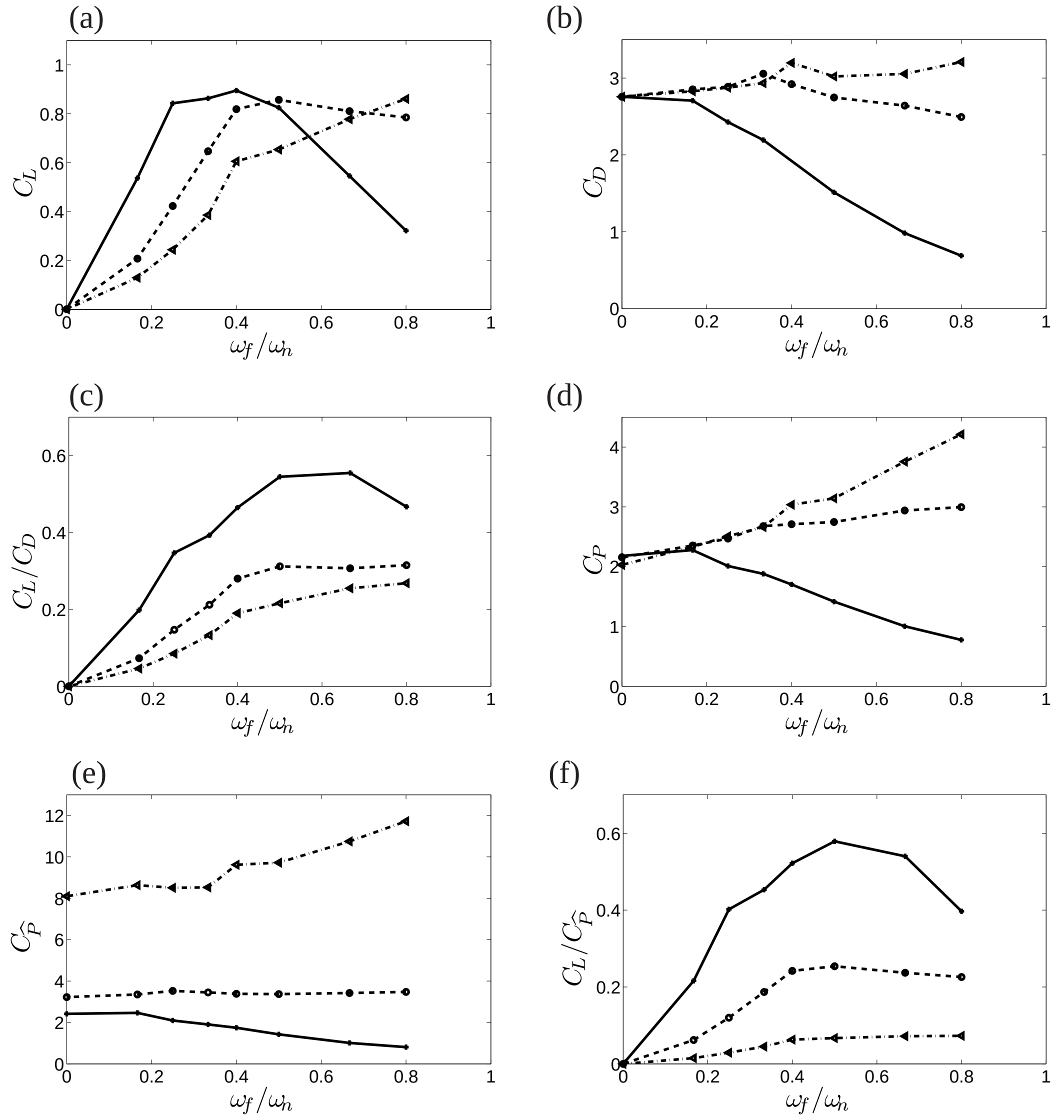

Figure 3.6: (a) Lift, (b) drag, (c) lift-to-drag, (d) net power, (e) modified power, and (f) lift-to-modified-power coefficients of the flexible wing without active rotation and $m^* = 1$ (solid), 5 (dashed), and 25 (dash-dotted).

place when the wing has the maximum translation and is nearly in a vertical position. For $m^* = 1$, the peak drag happens when the wing has the maximum translational velocity and the least frontal area, or when the wing is restoring its shape prior to the stroke reversal, at which point the wing has slowed down its translational movement. In either case, the drag is reduced considerably. The corresponding power coefficients for the three mass ratios are plotted in Fig. 3.7(d). Note that since the rotational term in Eq. (3.14) vanishes as $\beta = 0$, $C_{\hat{P}}$ is exactly equal to the positive portion of C_P in this case. Comparing the three mass ratios, we find that the power coefficient has least fluctuations for $m^* = 1$. In addition, the power peaks have more time delay when m^* is lower. For $m^* = 5$ and 25, the power reaches its maximum magnitude near the stroke reversals due to the inertial acceleration or deceleration of the wing.

The instantaneous vorticity field in an entire flapping cycle and the corresponding wing configuration are shown in Fig. 3.8 for $m^* = 5$ and 1 at $\omega^* = 0.5$. There are several similarities in the vortex behavior between the two cases. For example, a leading-edge vortex (LEV) is generated during each half-stroke and is then re-captured by the wing during its return trip after the stroke reversal (e.g., the positive vortex blob at $t/T = 13.0$ and the negative blob at $t/T = 13.5$). The LEV moves downward along the cambered wing and may merge with the trailing edge vortex (TEV) [68] of the same sign that is being formed (e.g., the positive blob at $t/T = 13.1$ and the negative blob at $t/T = 13.6$). The merged vortex is strengthened and meanwhile stretched by the trailing edge as shown by the positive vortex band at $t/T = 13.3$ and also by the negative band at $t/T = 13.8$. The gradually thinned trailing edge vortex eventually pinches off in the middle (e.g., the filament between two positive blobs at $t/T = 13.5$). The portion that attaches to the trailing edge, now termed the end-of-stroke vortex (ESV) [51], has been evolving during the stroke reversal while the wing is restoring its shape and then deforming in the other way (e.g., $t/T = 13.3$ to 13.6). After the TEV breaks off from the ESV, it travels downward in the wake, while the ESV later also detaches from the trailing edge but may temporarily move upward before disappearing or merging into

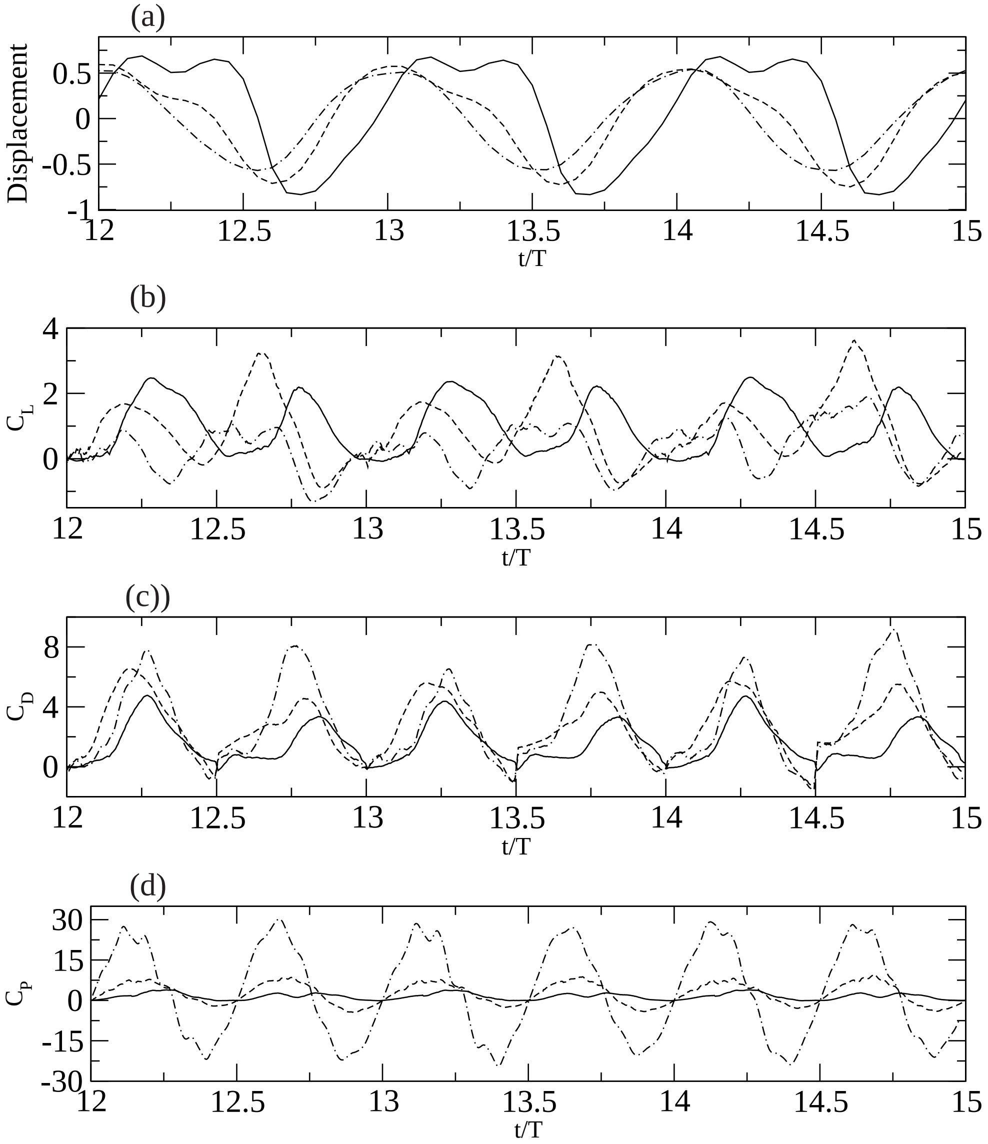

Figure 3.7: Histories of (a) the tail displacement in the *x*-direction, (b) C_L, (c) C_D, and (d) C_P for $\omega^* = 0.5$ and $m^* = 1$ (solid), 5 (dashed), and 25 (dash-dotted).

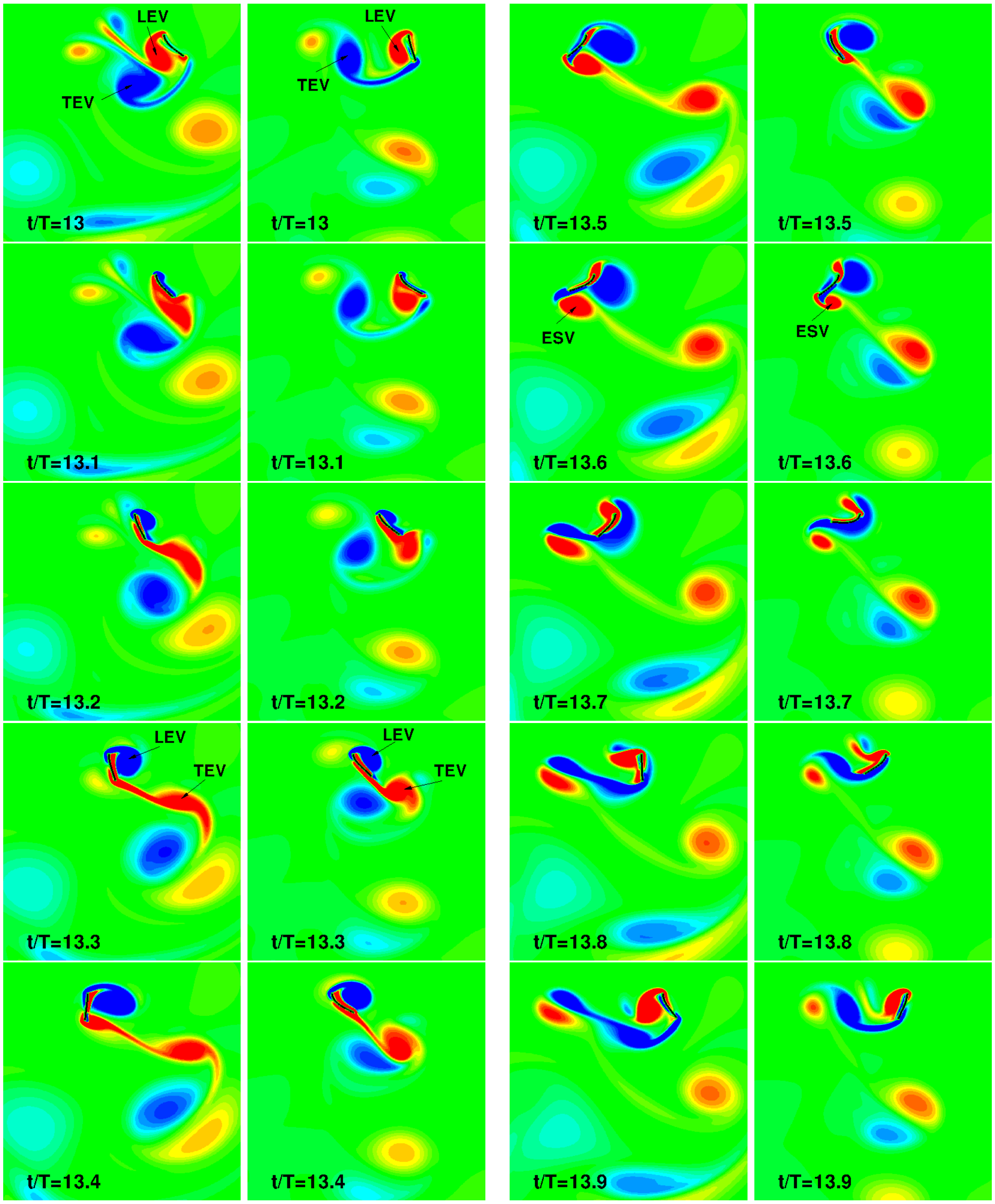

Figure 3.8: A series of instantaneous vortex field in a flapping cycle for $\omega^* = 0.5$, m^*=5 (first and third columns) and $m^* = 1$ (second and fourth columns). The contour level ranges from -3.2U/c to 3.2U/c.

the downwash. The wake below the hovering wing is marked by a pair of TEVs with opposite signs that are generated by the two half-strokes in a complete cycle.

The differences in the flow field between $m^* = 5$ and 1 are also evident. First, the size of the LEV for $m^* = 5$ is generally larger than that for $m^* = 1$. Second, the stretched trailing edge vortex for $m^* = 5$ is aligned more in the horizontal direction, while it is more in the vertical direction for $m^* = 1$, as shown in the frames from $t/T = 13.4$ to 13.7. These flow features are consistent to the higher drag formation for $m^* = 5$. Furthermore, a substantial portion of the flow in the case of $m^* = 5$ travels in the horizontal direction, or even in an upward direction, while in the case of $m^* = 1$, the flow mainly travels downward, leading to superior energy efficiency of this wing. For $m^* = 1$, the unsteady vortices may cause aperiodic vibration of the wing. This phenomenon is illustrated in the frames $t/T = 13.2$ to 13.4, where a blob of negative vortex passes underneath the wing, causing the wing to deflect for the second time in the same half-stroke.

The distinct vortices have been indicated in Fig. 3.8. To quantify the strength of these vortices, we first visualize the vorticity field using contour lines. After each vortex is manually identified, a closed contour line is generated around this vortex with the specified level, and then the circulation Γ is computed along this line. Though the magnitude of the circulation depends on the chosen contour level, the characteristic behavior of the vortex is not affected by this choice. The computed circulations of the LEV, TEV, and ESV are shown in Fig. 3.9 for the vortices indicated in Fig. 3.8. It can be seen that the LEV for $m^* = 5$ is much stronger than the corresponding vortex for $m^* = 1$ over a significantly long period of time. The TEV is initially stronger for $m^* = 5$, but after breaking up, it has a similar strength for both mass ratios. Furthermore, the timing of the LEV and the TEV is similar for the two mass ratios. It should be pointed out that the difference between the LEVs and between TEVs shown in Fig. 3.9 is fairly consistent for different wing strokes, but the difference between the ESVs is not. The appearance and strength of the ESV vary from stroke to stroke, and they depend on the evolution of the LEV. For example, in Fig. 3.8 for $m^* = 5$ from $t/T = 13.0$ to 13.1, the LEV moves along the wing to the trailing edge and suppressed formation of the ESV. Consequently, the ESV for $m^* = 1$ is stronger during that stroke reversal (this ESV is visible in Fig. 3.8 but is too weak to show up in Fig. 3.9).

Generally speaking, the strength and timing of the vortices have important consequences on the force production of flapping wings. In the present case, the three types of vortices have both positive and negative effects on the wing performance. For example, during the translational stage, the LEV and the TEV cause the flow to circulate around the leading edge and the trailing edge, reducing the pressure difference between the two sides of the wing and thus lowering the lift. However, the shed vortices provide lift augmentation through the wake-capturing mechanism. This effect can be seen from Fig. 3.8 at $t/T = 13.6$, where the LEV and ESV create a flow directed against the wing and thus the lift is enhanced. The lift enhancement at the moment is seen from Fig. 3.7(b), where the $m^* = 5$ wing has significantly higher lift than the $m^* = 1$ wing at $t/T = 13.6$.

3.6 Flexible translating wings with rotation

Next we consider the situation where the wings both translate and rotate actively around the leading edge with an amplitude of $\beta = \pi/8$. Only $m^* = 5$ and 1 are considered here. Figure 3.10(a) shows the averaged lift coefficient C_L of the wing. The corresponding non-rotational cases are also included in the figure for comparison. It can be seen that for both $m^* = 5$ and 1, adding a moderate amount of active rotation significantly increases the lift force for a range of ω^*. When ω^* is large and the wing is very flexible, the active rotation reduces the lift instead due to the upward swinging motion of the wing tail. The frequency ratio of the rotational wing at which the lift peaks is lower compared to that of the corresponding non-rotational wing. Therefore, when the wing is actively rotating, less structural flexibility is needed for lift enhance-

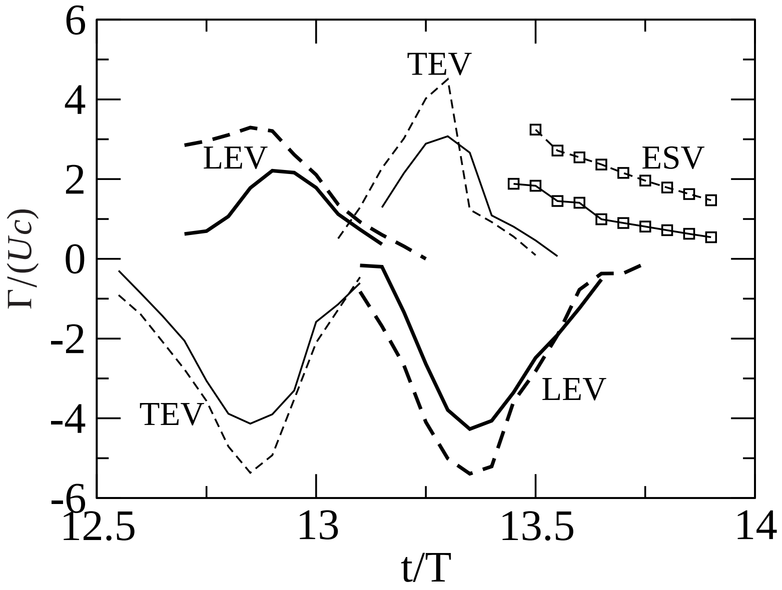

Figure 3.9: Histories of the circulation for the vortices in the flow at $\beta = 0$, $\omega^* = 0.5$, $m^* = 1$ (solid lines) and 5 (dashed lines); the vortex type and the specified contour level are: LEV with $\pm 3.95U/c$ (thick lines), ESV with $\pm 1.9U/c$ (squares), and TEV with $\pm 3.95U/c$ (thin lines).

ment. Furthermore, like the non-rotational wings, the lift curves of the rotational wings also have a peak value whose amplitude is insensitive to the wing mass ratio but whose corresponding frequency ratio exhibits a left-shift trend when the mass ratio is reduced.

The average drag coefficient is shown in Fig. 3.10(b). The active rotation reduces the drag for both $m^* = 5$ and 1 for all the frequency ratios. In addition, the effect of the frequency ratio on the drag coefficient for the rotational wings is similar to that for the corresponding non-rotational wings. That is, for $m^* = 5$, the drag coefficient only changes slightly when the wing becomes more flexible, while for $m^* = 1$ the drag coefficient reduces significantly. The lift-to-drag ratio in Fig. 3.10(c) shows that the combination of the active rotation and passive wing deformation improves the wing performance by 66.7% for $m^* = 5$ and 38.7% for $m^* = 1$. Compared to the wings without rotation, the optimal frequency ratio for the lift-to-drag ratio is shifted to a lower value for the wings with active rotation. For both $m^* = 5$ and 1, this value is around $\omega^* = 0.4$. As a reference, we provide the lift coefficient, the drag coefficient, and the lift-to-drag-ratio of a rigid wing performing the same translation at the leading edge but rotates with an amplitude of $\beta = \pi/4$. The Reynolds number is also $Re = 150$ for this rigid wing. The results are shown in Fig. 3.10(a,b,c) as the dotted lines. Comparing this rigid wing with the flexible wings that has less active rotation, we notice that the flexible wings may generate higher lift when they have a proper rigidity, but the reference wing has considerably lower drag. In terms of the lift-to-drag ratio, only the light wing with $m^* = 1$ can out-perform the reference wing by a small amount (around 6%). This result suggests that there may be an optimal combination of the active wing rotation and the passive wing deformation.

The active rotation has a similar effect on the power efficiency of the flexible wings. Figures 3.10(d) to (f) show the net power coefficient, the modified power coefficient, and the lift-to-modified-power coefficient, respectively. Overall, introducing active rotation reduces the power requirement and significantly improves the power efficiency. The frequency ratio for the optimal power performance is down-shifted to 0.35 for the wings with active rotation, regardless the mass ratio. Finally, we point out that in both the lift-to-drag and lift-to-modified-power measurements, the wing with $m^* = 1$ significantly out-performs the wing with $m^* = 5$ by 34% for C_L/C_D and 71% for $C_L/C_{\hat{P}}$.

Figure 3.11 shows the x-displacement, lift, drag, and power histories of the rotational wing at $\omega^* = 0.4$. There is again a phase delay in the displacement of the wing with $m^* = 1$ compared to that for $m^* = 5$. Although the light wing does not have an obvious double-peak displacement within a single half-stroke as shown earlier for the corresponding non-rotational wing, the deformation has nearly a plateau after the wing passes the mid-stroke point. The peak lift for $m^* = 1$ takes place at the mid-stroke point where the wing has the maximum translation. For $m^* = 5$, the peak lift point during second half-stroke also takes place at the mid-stroke point, but it is brought earlier during the first half-stroke. The drag histories are in phase with each other for the two wings, but the $m^* = 5$ wing clearly produces a higher peak drag when the wing passes the mid-stroke point. The histories of the net and modified power coefficients, plotted

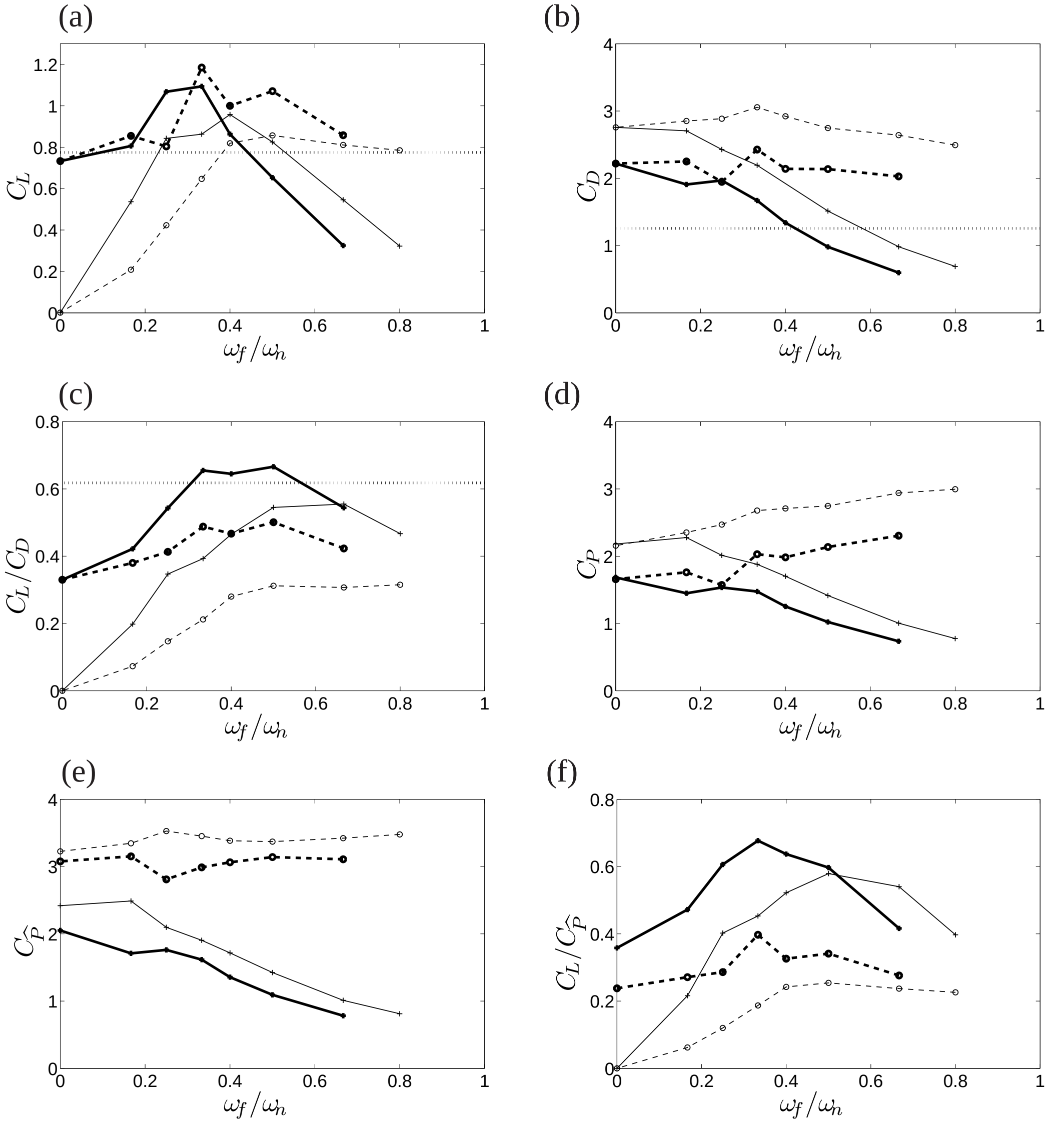

Figure 3.10: (a) Lift, (b) drag, (c) lift-to-drag, (d) net power, (e) modified power, and (f) lift-to-modified-power coefficients of the flexible wing with active rotation $\beta = \pi/8$ for $m^* = 1$ (thick solid) and 5 (thick dashed). The corresponding data for the non-rotational wing are shown as thin lines. The dotted lines in (a) to (c) are for the corresponding rigid wing with a rotation angle of $\beta = \pi/4$.

in Fig. 3.11(d,e), show that the power input has large fluctuations for $m^* = 5$, especially before and after the stroke reversals when the wing experiences the maximum inertial deceleration or acceleration. On the other hand, the power input for $m^* = 1$ is nearly always positive and has a much lower amplitude of fluctuation.

The flow field is shown in Fig. 3.12 for $m^* = 5$ and 1 at $\omega^* = 0.4$. Comparing this figure with Fig. 3.8, it can be seen that the LEV now becomes more attached to the rear side of the wing due to the active rotation and an on-average reduced angle of attack at the leading edge. Compared the flow fields between $m^* = 5$ and 1, we see again that the LEV of the light wing is smaller in size than that of the heavy wing. In addition, the vortices have less upward movement in the case of $m^* = 1$, and the vortex pairs in the wake are more evenly spaced compared to $m^* = 5$. Using the same approach described earlier, we compute the instantaneous circulations for the LEV, TEV, and ESV identified from the vorticity contours shown in Fig. 3.12, and the result is plotted in Fig. 3.13. Like the non-rotational wing, the LEV and the TEV are again consistently much stronger for $m^* = 5$ than for $m^* = 1$, while the difference between the ESVs of the two wings may vary for each stroke reversal. Among these three vortices, the LEV and the ESV have a significant contribution to the lift during the wake capture. Therefore, immediately after the right stroke reversals (e.g., $t/T = 13.1$), the wing with $m^* = 5$ has both stronger LEV and ESV and thus a much higher lift coefficient than the wing with $m^* = 1$; while immediately after the left stroke reversals, the wing with $m^* = 5$ has a stronger LEV but a weaker ESV (e.g., $t/T = 13.6$), thus the wing has only a moderately higher lift coefficient than the wing with $m^* = 1$, as shown in Fig. 3.11.

3.7 Discussion

According to the insect data in [55], a hawkmoth *Manduca* wing has a chord length on order of 10 cm and an approximate thickness of $h = 45\ \mu$m. Using the wing density $\rho_s = 1200$ kg/m^3 and the air density $\rho_f = 1.2$ kg/m^3, we obtain the mass ratio $m^* =$

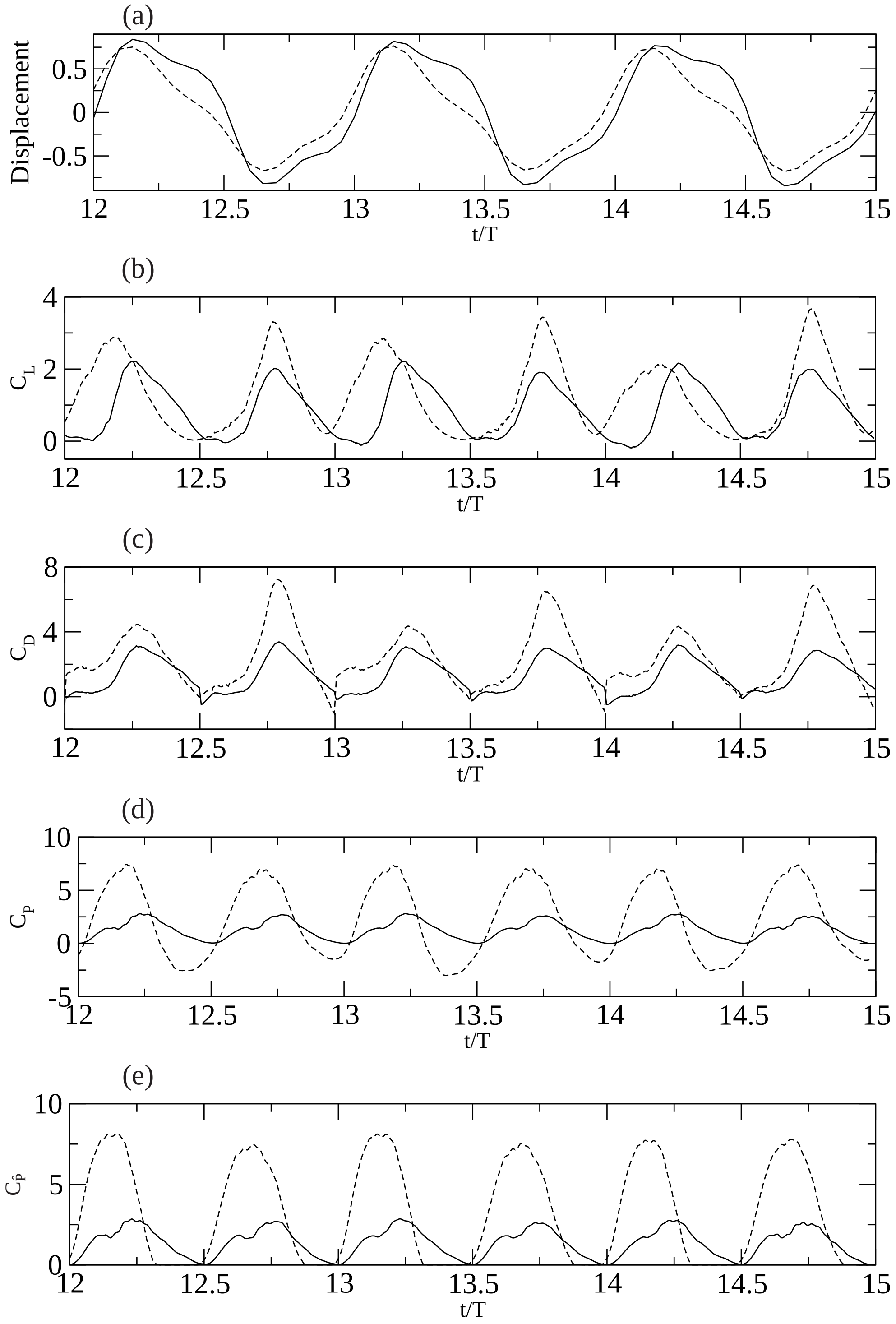

Figure 3.11: Histories of (a) the tail displacement in the x-direction, (b) C_L, (c) C_D, (d) C_P, and (e) $C_{\hat{P}}$ for $\omega^* = 0.4$, $m^* = 1$ (solid), 5 (dashed), and the rotational angle $\beta = \pi/8$.

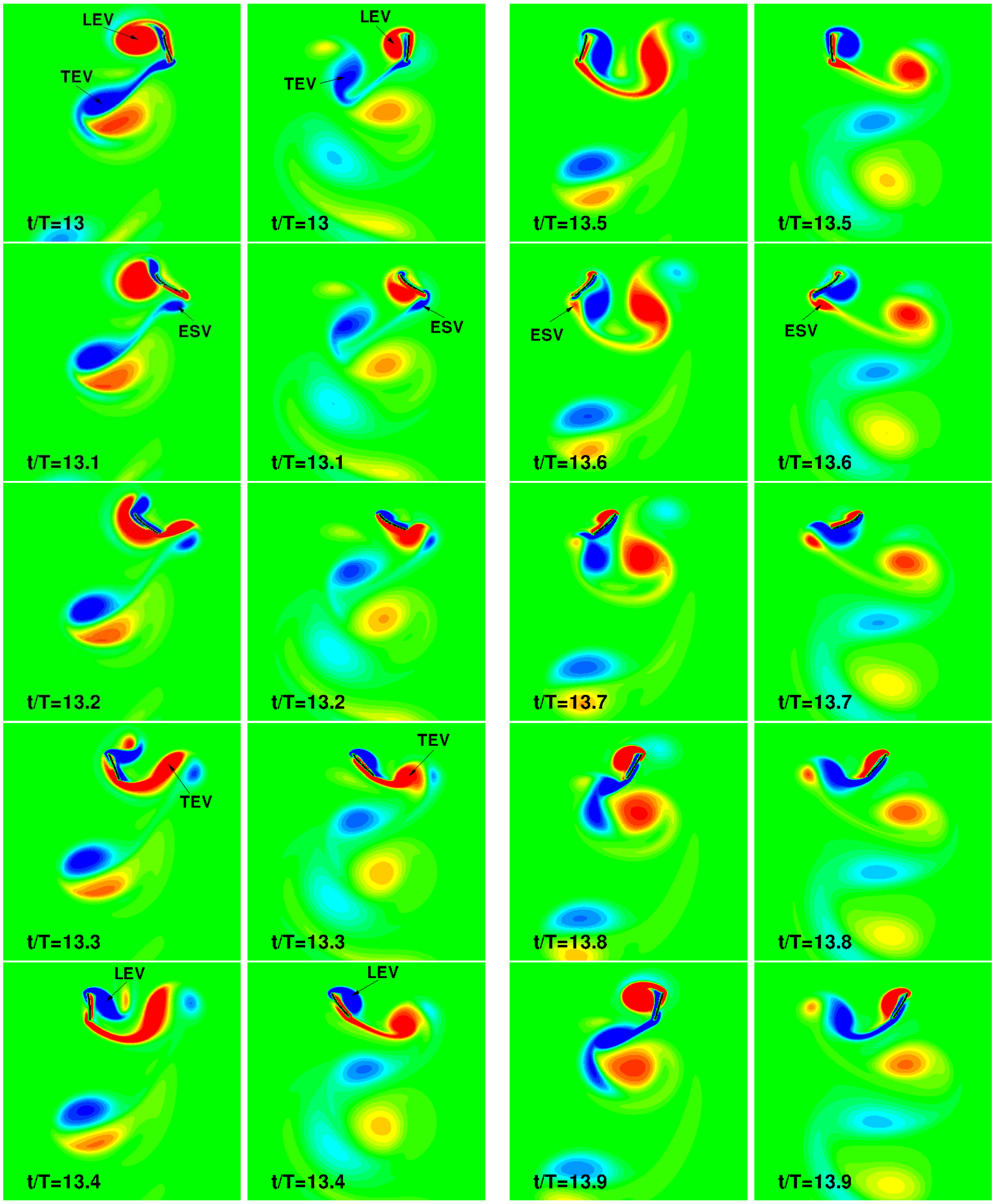

Figure 3.12: A series of instantaneous vortex field in a flapping cycle for $\beta = \pi/8$, $\omega^* = 0.4$, m^*=5 (first and third columns) and $m^* = 1$ (second and fourth columns). The contour level ranges from -3.2U/c to 3.2U/c.

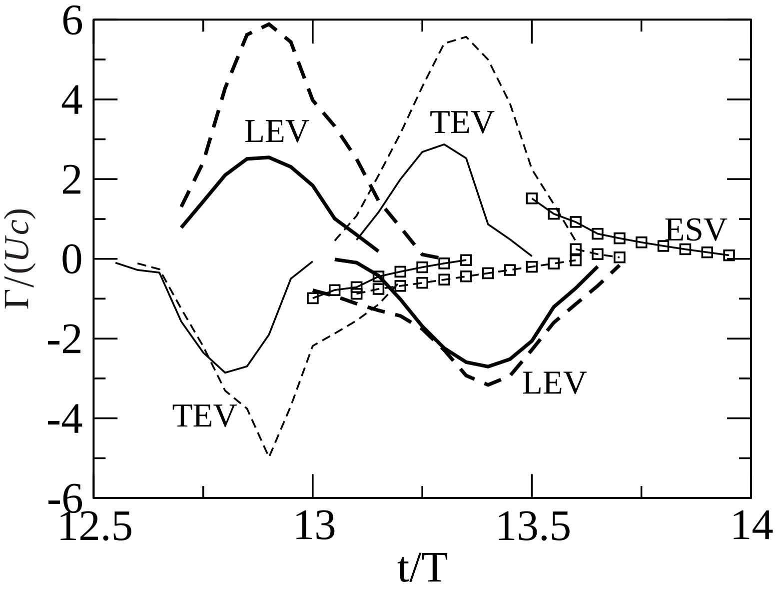

Figure 3.13: Histories of the circulation for the vortices in the flow at $\beta = \pi/8$, $\omega^* = 0.4$, $m^* = 1$ (solid lines) and 5 (dashed lines); the vortex type and the specified contour level are: LEV with $\pm 3.95U/c$ (thick lines), ESV with $\pm 1.9U/c$ (squares), and TEV with $\pm 3.95U/c$ (thin lines).

$\rho_s h/(\rho_f c) = 4.5$. Chen *et al.* [56] measured the natural frequency of the dragonfly wing (*Orthetrum pruinosum* and *Orthetrum sabina*). In their study, the wing has a dimension of 38 mm × 8 mm, and the wing mass is 2.5 mg. Based on these data, the mass per unit wing area is around $\rho_s h = 8.2$ mg/mm^2, and the mass ratio is $m^* = 0.85$. Therefore, the hawkmoth and dragonfly wings correspond roughly to the $m^* = 5$ and 1 cases, respectively, in the present simulations, and the wing inertia seems to play different roles in the structural deformation in these two insects. Chen *et al.* [56] found that the flapping frequency of the dragonfly is only about 16% of the natural frequency of the wing. Their finding is thus consistent to our result that for the low-mass wing to have best performance, the flapping frequency should be much lower than the resonant frequency. Our simulation further suggests that the dragonfly could have taken advantage of the low mass ratio of its wings for efficient lift production. We should point out that a direct comparison of the aerodynamic performance between the dragonfly wing and the hawkmoth wing is not possible through the present work, since the three-dimensional effect, which is an important factor in insect flight, is not considered here.

Finally, we should note that the mass ratio of an insect wing can not be reduced arbitrarily, even though reducing the mass ratio more may further improve the wing performance aerodynamically. This is because the wing needs to maintain at least a minimal thickness to achieve the necessary rigidity and its physiological functions. In some insect wings, certain structural features may help reduce the wing mass while retaining the necessary stiffness, e.g., corrugations of the dragonfly wing [69].

3.8 Conclusion

In this study the fluid-structure interaction of a two-dimensional hovering wing is numerically simulated in order to investigate the effect of the wing inertia on the wing deformation and the aerodynamic performance. The wing is parametrized by a nondimensional mass ratio and a frequency ratio representing the wing flexibility. The mass ratio is taken from the physiological data of insects. The simulation shows that when the amount of deformation is about the same, the low-mass wing has consistently better performance than the high-mass wing in terms of the lift-to-drag ratio and power efficiency. Therefore, the present result suggests that the fluid force dominated wing flexibility has aerodynamic advantages over the inertial force dominated flexibility.

CHAPTER 4

HYDRODYNAMIC INTERACTION OF OBLIQUE SHEETS IN TANDEM ARRANGEMENT

4.1 Background

Vortex-induced vibration is a common phenomenon for elastic bodies immersed in flow, and it has a broad range of applications in the engineering design of aerospace and civil structures. The underlying fluid–structure interaction in this phenomenon has been discussed extensively in literature [70]. In its early applications, vortex-induced vibration is generally deemed harmful to the system and thus should be avoided during the design process. Recently, this phenomenon has been explored as a mechanism for harvesting energy from the flow. For example, Bernitsas *et al.* [71] presented a hydroelectric device in which vortex shedding from a group of cylinders causes the cylinders to vibrate and the vibration is then converted to electricity through the electromagnetic system on the tracks of each cylinder's axle. In Akaydin *et al.* [10] and Li *et al.* [11], thin elastic structures with built-in piezoelectric materials were used to convert the kinetic energy of the vibrating structures into electricity. In those piezoelectric devices, the elastic sheet is either mounted transverse to the flow [11] or parallel to the flow [10]. In the latter case, vibration of the sheet is sustained by the vortices shed from a bluff body located upstream. In all these examples, the system resonance is sought, instead of being avoided as in early applications, to maximize the potential of energy conversion.

When multiple oscillators are placed in close range in a flow, hydrodynamic interaction among the oscillators would be unavoidable (Fig. 4.1). It may be possible to utilize such interaction to improve the energy harvesting performance of the oscillators. The basic idea is that the overall capacity of a group of devices exceeds the sum of the individuals operating independently. Analogies in nature of this idea are the schooling behavior of fish and the formation flight of birds, where the animals are likely able to save energy by taking advantage of the vortices shed from their neighbors [72–74]. Motivated by the application of the piezo-sheets in energy production and inspired by the animal behaviors in nature, in the present work we consider the hydrodynamic interaction of two elastic sheets that are placed in tandem in a free stream.

For vortex-induced vibration, an elastically mounted cylinder is a classical configuration to study the fundamental fluid–structure interaction. A comprehensive review of this model problem can be found in Williamson & Govardhan [70]. The hydrodynamic interaction between two closely placed bodies is also studied frequently using two cylinders. The cylinders may be fixed [75] but more often are allowed to vibrate freely [76–78]. Zdravkovich [76] provided a review of vibrations of two cylinders in tandem, side-by-side, and staggered arrangements. For the tandem arrangement, Zdravkovich described several experimentally observed response types of the cylinders and briefly sketched two interference mechanisms that lead a variety of vibration behaviors. These are the so-called gap-flow-switch mechanism, which takes effect in the region of $1 < d/D < 3.5$, and the wake-displacement mechanism, which takes effect

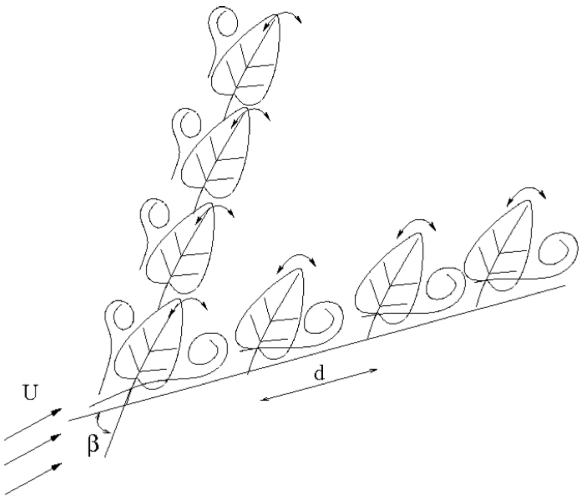

Figure 4.1: Illustration of leaves in the wind.

in the region of $d/D > 3.5$. Here d denotes the center-to-center distance and D the diameter of the cylinders. The main difference between the two is that in the former mechanism the downstream cylinder disrupts vortex shedding from the upstream cylinder, while in the latter the downstream cylinder is affected by the upstream vortices but it does not in turn change the vortex shedding event of the upstream cylinder. Borazjani & Sotiropoulos [78] numerically studied two cylinders in tandem at a distance of $d/D = 1.5$ and further discussed the underlying vortex-vortex and vortex-cylinder interactions. They systematically varied the reduced velocity and determined the lock-in region within which both cylinders undergo increased and coordinated vibrations. According to their conclusion, the direct exposure to the free stream by the displaced rear cylinder initiates a flow through the gap region created due to the relative position shift of the two cylinders in the transverse direction, and such a gap flow is the key to sustain the large-amplitude oscillations of the cylinders.

Compared to the cylinders with elastic foundation, oscillations of deformable bodies such as thin-walled structures in tandem arrangement were studied much less frequently. Having more degrees of freedom, deformable bodies may interact with the flow in more complex manners than rigid bodies. In the case of two elastic sheets considered here, vortex shedding is affected by the movement as well as the shape change of the sheets. Furthermore, since the sheets will be clamped on one side in the current study, the relative position of the sheets in the cross-flow direction does not change as the two free cylinders would. As a result, the rear sheet is not directly subject to the free stream, and the mechanism used to explain the excitation of the cylinders [78] is thus not be applicable in the present study.

It should be noted that deformable bodies in tandem arrangement have been studied in the context of flapping flags, e.g., Ristroph & Zhang [79] and Zhu [80]. In those studies, two highly flexible filaments pinned at the leading edge and are aligned along with the free stream. It was found that like the cylinders, both the front and rear flags can be affected by the wake interference. However, the front flag's oscillation is typically sup-

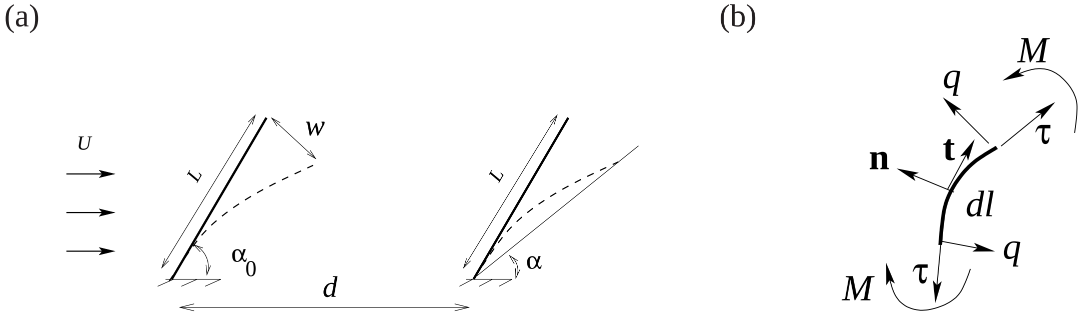

Figure 4.2: (a) Two elastic sheets in tandem mounted obliquely to the free stream, where α_0 is the mount angle, α is the pitch angle used to measure the passive rotation, and w is the tip displacement. (b) A segment of the sheets showing the in-plane tension τ, the transverse stress q, and the bending moment M.

pressed compared to the single flag, while the rear flag's oscillation can be increased. In the present study, the two elastic sheets are oblique to the free stream and are clamp-mounted, and it is not straightforward to predict the deformation modes and the energy levels of the sheets. We also point out that in the studies of the flapping flags, the bending rigidity of the structures is very low and may be on order of 10^{-4} when normalized by the freestream properties (density and velocity) and the length of the flags [80]. As a result, the flags exhibit high modes of deformation under the flow-induced vibration, and traveling waves are formed along the flags. From the energy-harvesting perspective, little energy is stored in such structures. In the present configuration, the elastic sheets are mounted obliquely to the flow to facilitate flow instability and vortex shedding, and the setup will allow the induced vibration to happen at much higher bending stiffness. This feature could be desirable for the purpose of energy harvesting.

In the present study, we will investigate that for given elastic properties, whether there is a particular distance at which the hydrodynamic interaction would enhance the vibration of both front and rear sheets and what would be the basic mechanism for such interaction.

4.2 Problem formulation and numerical method

We consider a two-dimensional configuration as shown in Fig. 4.2(a), where two identical elastic sheets of length L are clamp-mounted in tandem and are oblique to the flow with an angle α_0. The distance between them is d. The sheets are nearly inextensible but can have dynamical bending. The balance of the inertial force, the elastic force, and the hydrodynamic load for each sheet is governed by following equation [64]

$$\rho_s h \frac{\mathrm{d}^2\mathbf{x}}{\mathrm{d}t^2} = \frac{\partial}{\partial l}(\tau\mathbf{t} + q\mathbf{n}) + \mathbf{f}, \tag{4.1}$$

where ρ_s and h are the density and the thickness of the sheet, respectively, $\mathbf{t}$ is the unit tangent vector pointing in the direction of increasing arc length l from the base to the tip, $\mathbf{n}$ is the unit normal vector, and $\mathbf{f}$ is the difference between the distributed loads on the two sides of the sheet. The in-plane tension τ, is assumed to be proportional to the tangential strain so that

$$\tau = E_S\left(\left|\frac{\partial l}{\partial l_0}\right| - 1\right), \tag{4.2}$$

where E_S is the stretching coefficient and l_0 is the arc length at the unstretched state. The transverse stress, q, is linearly related to the bending moment, M, by

$$q = \frac{\partial M}{\partial l} = \frac{\partial(E_B\kappa)}{\partial l}, \tag{4.3}$$

where E_B is the bending coefficient, and κ is the curvature [64]. E_B is related to Young's modulus E by $E_B = EI$, where I is the second moment of inertia of the cross section. Note that structural damping is not included in the present model. The boundary conditions at the base include the specified position and orientation, i.e.,

$$\mathbf{x} = \mathbf{x}_0, \qquad \frac{\partial\mathbf{x}}{\partial l} = (\cos\alpha_0, \sin\alpha_0). \tag{4.4}$$

At the free end, $l = L$, both M and q vanish, which requires $\kappa = 0$ and $\partial\kappa/\partial l = 0$. Therefore, we have [64]

$$\frac{\partial^2 \mathbf{x}}{\partial l^2} = 0, \qquad \frac{\partial^3 \mathbf{x}}{\partial l^3} = 0. \tag{4.5}$$

The flow is governed by the viscous incompressible Navier–Stokes equation and the continuity equation,

$$\begin{aligned} \frac{\partial v_i}{\partial t} + \frac{\partial v_j v_i}{\partial x_j} &= -\frac{1}{\rho_f}\frac{\partial p}{\partial x_i} + \nu_f \frac{\partial^2 v_i}{\partial x_j^2}, \\ \frac{\partial v_i}{\partial x_i} &= 0, \end{aligned} \tag{4.6}$$

where v_i is the velocity, ρ_f and ν_f are the fluid density and viscosity, and p is the pressure. No-slip and no-penetration conditions are specified at the fluid–solid interface.

The equations governing the system, (4.1) and (4.6), are solved numerically in a coupled manner using an in-house solver. Specifically, the flow is solved using a sharp-interface immersed-boundary method [81]. The thickness of the sheet is assumed to be small so that $h << L$. In the numerical method, the sheet is augmented with an artificial thickness that is about three times of grid spacing around the sheet. A standard central finite-difference scheme is used to discretize Eq. (4.1), which is solved iteratively as an inner loop embedded within the iterative algorithm at each time step for the fluid–structure coupling. More details about the numerical method can be found in our previous publications [82, 83].

The non-dimensional groups in this problem include the reduced distance between the sheets, d/L, the Reynolds number

$$Re = \frac{UL}{\nu_f}, \tag{4.7}$$

the mass ratio,

$$m^* = \frac{\rho_s h}{\rho_f L}, \tag{4.8}$$

and the Strouhal number,

$$St_n = \frac{f_n L}{U}, \tag{4.9}$$

where

$$f_n = \frac{k_n^2}{2\pi L^2}\sqrt{\frac{E_B}{\rho_s h}} \tag{4.10}$$

and $k_n = 1.8751$, is the natural frequency of the first vibration mode based on the Euler-Bernoulli beam theory [65]. Note that m^* represents the ratio between the inertial force and the dynamic pressure of a sheet vibrating in an otherwise quiescent fluid. A large value of m^* means that the inertial force of the sheet is higher than the fluid force. The stiffness of the sheets is represented by St_n. The amplitude of vibration, A_m, is defined by dividing the peak-to-peak displacement of the free end of the sheet by two. In addition, we define the pitch angle, α, as the angle from the x-axis to the straight line connecting the base and tip of each sheet (see Fig. 4.2(a)), and we calculate the total hydrodynamic torque on each sheet by integrating along each sheet according to

$$T = \int_0^L (\mathbf{x} - \mathbf{x}_0) \times \mathbf{f} \mathrm{d}\mathbf{x} \tag{4.11}$$

where $\mathbf{x}_0$ is the base point of the sheet.

Unless otherwise noted, $Re = 300$ is used in the simulation. The Strouhal number is $St_n = 0.2$, which is chosen so that the natural frequency is close to the vortex shedding frequency. In the literature, the inverse of St_n or the reduced velocity, $f_n L/U$, is also often used to represent the frequency of the structure. We set the mass ratio to be $m^* = 1$

or 5. Note that when St_n is fixed, the sheet with $m^* = 1$ is more flexible than the sheet with $m^* = 5$. The specific values of m^* are chosen based on the insect wing data [84], where $m^* = 5$ means that the wing inertia is dominant and $m^* = 1$ means that the wing inertia and the fluid force are comparable. Interestingly, these values fall within the range of data for tree leaves, as shown by a straightforward calculation based on the data given in Milla & Reich [85]. The mount angle is chosen to be $\alpha_0 = 60°$, which represents the angle between tree leaves and wind.

The computational domain is a rectangular box of $40L \times 22L$ in size, and a nonuniform Cartesian grid of 445×324 points is used to discretize the entire domain. The minimum grid spacing around the sheets is $0.025L$ in both x- and y-directions. The non-dimensional time step is $\Delta tU/L = 0.0125$. To confirm that the grid is sufficient, we have doubled the resolution in both directions around the sheets. The result is shown by plotting the history of the tip displacement in Fig. 4.3 for both the front and rear sheets at $m^* = 1$ and $d/L = 1.2$. The comparison indicates that the current resolution is satisfactory. Furthermore, we have done a few tests to verify that the current size of the computational domain is large enough.

4.3 Results: the characteristics of vibration

We vary the separation distance, d/L, from 1.2 to 6 while keeping all the other variables constant. The statistics are calculated from more than 20 cycles after the vibrations of the sheets are fully established. Fig. 4.4 shows the reduced vibration amplitude, A_m/L, for both $m^* = 1$ and $m^* = 5$ as a function of d/L. As a reference, the amplitude of the corresponding single sheet is also plotted. Note that the mean displacement has been excluded from the definition of the vibration amplitude. It can be seen that for both mass ratios, there is an obvious region of d/L within which the oscillations of the two sheets are significantly higher than that of the single sheet. In particular, the rear sheet is greatly excited, and its amplitude can be a few times as

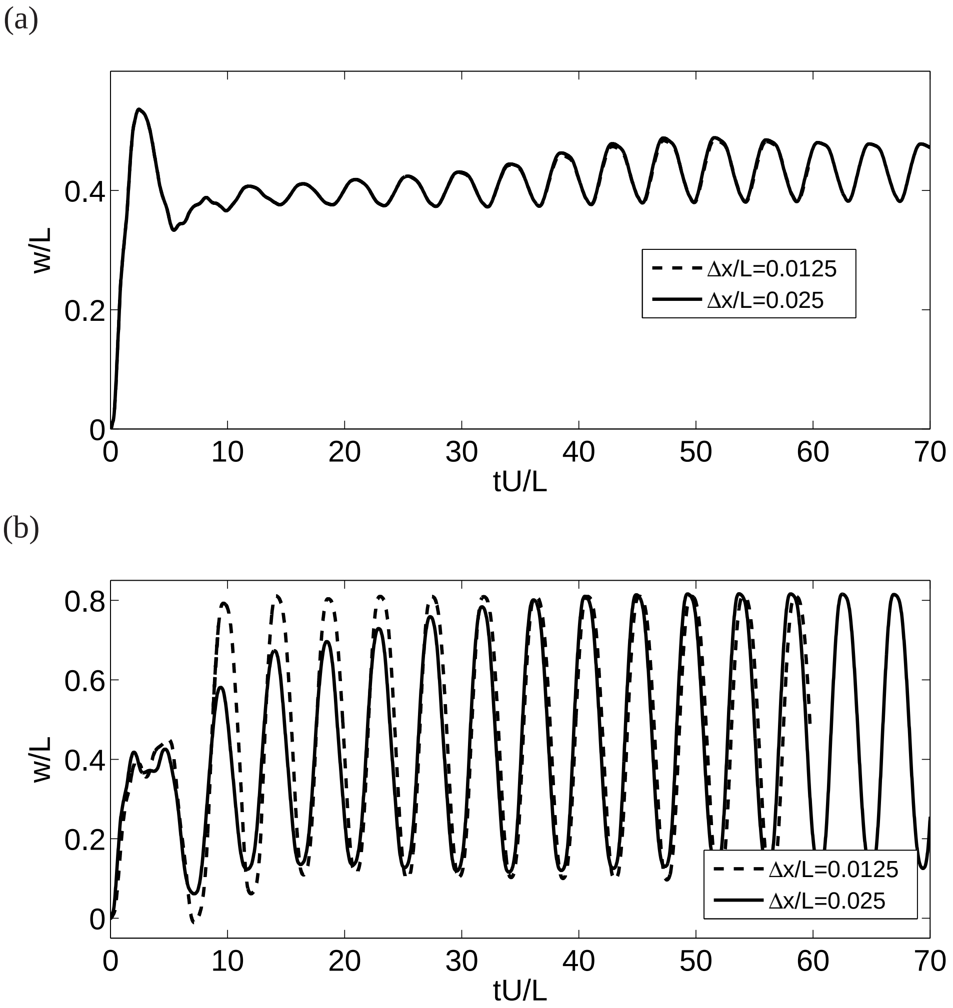

Figure 4.3: The tip displacement, w/L, of the front sheet (a) and of the rear sheet (b) for $m^* = 1$ and $d/L = 1.2$.

high as that of the front sheet. We will refer this phenomenon as the system resonant behavior and will focus on the detail of the fluid–structure interaction at this state. Such resonance was also seen for two elastically mounted cylinders [78] when they are in close proximity and when the Strouhal number is adjusted to a proper range. However, as discussed in Section 4.1, there are important differences between the thin sheets and the cylinders.

Fig. 4.4 also shows that the region of resonance and the magnitude of vibration vary depending on the mass ratio. For $m^* = 1$, the region of resonance ranges from the lowest separation distance that we tested, $d/L = 1.2$, to approximately $d/L = 4$.

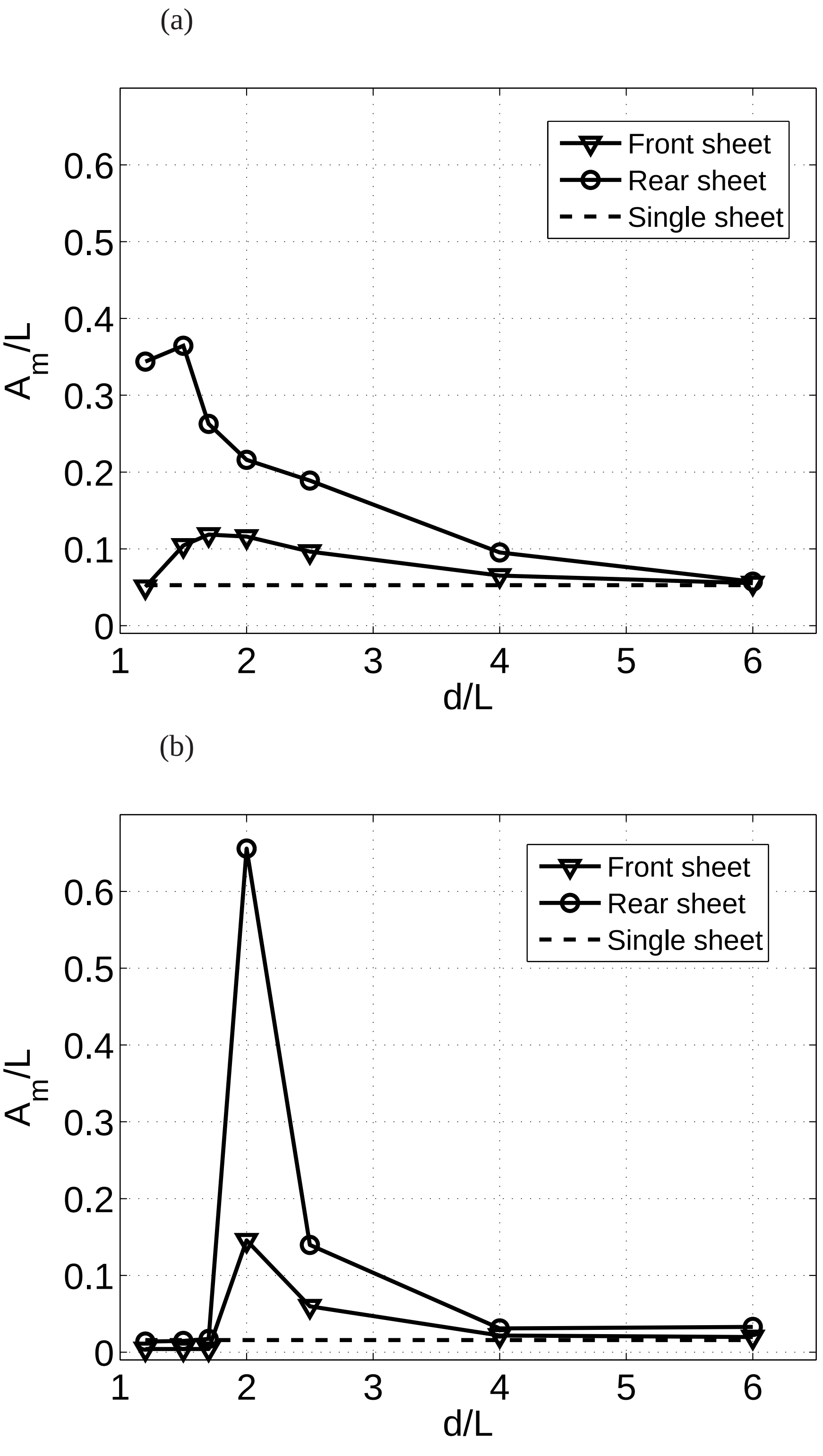

Figure 4.4: The time-averaged vibration amplitude against the separation distance for (a) m^*=1 and (b) m^*=5.

The peak oscillation is achieved around $d/L = 1.5$. At this distance, the oscillation amplitudes of the front and rear sheets are respectively twice and seven times that of the single sheet. For $m^* = 5$, the region of resonance is narrower, from $d/L = 2$ to $d/L = 4$. However, the excited sheets at this mass ratio are much more vibrant than those at $m^* = 1$. The peak oscillation takes place at $d/L = 2$ and the oscillation amplitude has reached $A_m = 0.15L$ for the front sheet and $A_m = 0.65L$ for the rear sheet. These two values are respectively eight and forty times of increase when compared with that for the corresponding single sheet. As the separation distance is further increased beyond $d/L = 4$, the oscillations of the two sheets approach to that of the single sheet due to the weakening interaction between the sheets.

The vibration patterns of the sheets are shown in Fig. 4.5 for the resonant cases. Also plotted is the single sheet at the corresponding mass ratios. It can be seen that in the case of $m^* = 1$, the mean deformations of the sheets are greater than those of the sheets in the case of $m^* = 5$. This is because the low-mass-ratio sheets also have lower stiffness when their natural frequencies are fixed. On the other hand, at high mass ratios, the hydrodynamic forces are smaller compared to the inertial force of the sheets. Therefore, due to the reduced dampening effect from the fluid, the sheets with high mass ratios may have stronger vibration, which is indeed seen here in the case of $m^* = 5$. Another observation from Fig. 4.5 is that the deformation patterns are of the first-mode type, and the magnitude of the displacement is clearly large enough for nonlinearity to occur in the dynamics of the sheets.

To quantify the energy level of the sheets, we calculate the kinetic energy, E_k, and the elastic potential, E_p, using the following expressions

$$\begin{aligned} E_k &= \frac{\rho_s h}{2}\int_0^L \left[\left(\frac{dx}{dt}\right)^2 + \left(\frac{dy}{dt}\right)^2\right] \mathrm{d}l \\ E_p &= \frac{1}{2}\int_0^L E_B \kappa^2 \mathrm{d}l. \end{aligned} \tag{4.12}$$

The total energy is thus $E_t = E_k + E_p$. In Fig. 4.6 we plot the time-averaged total energy

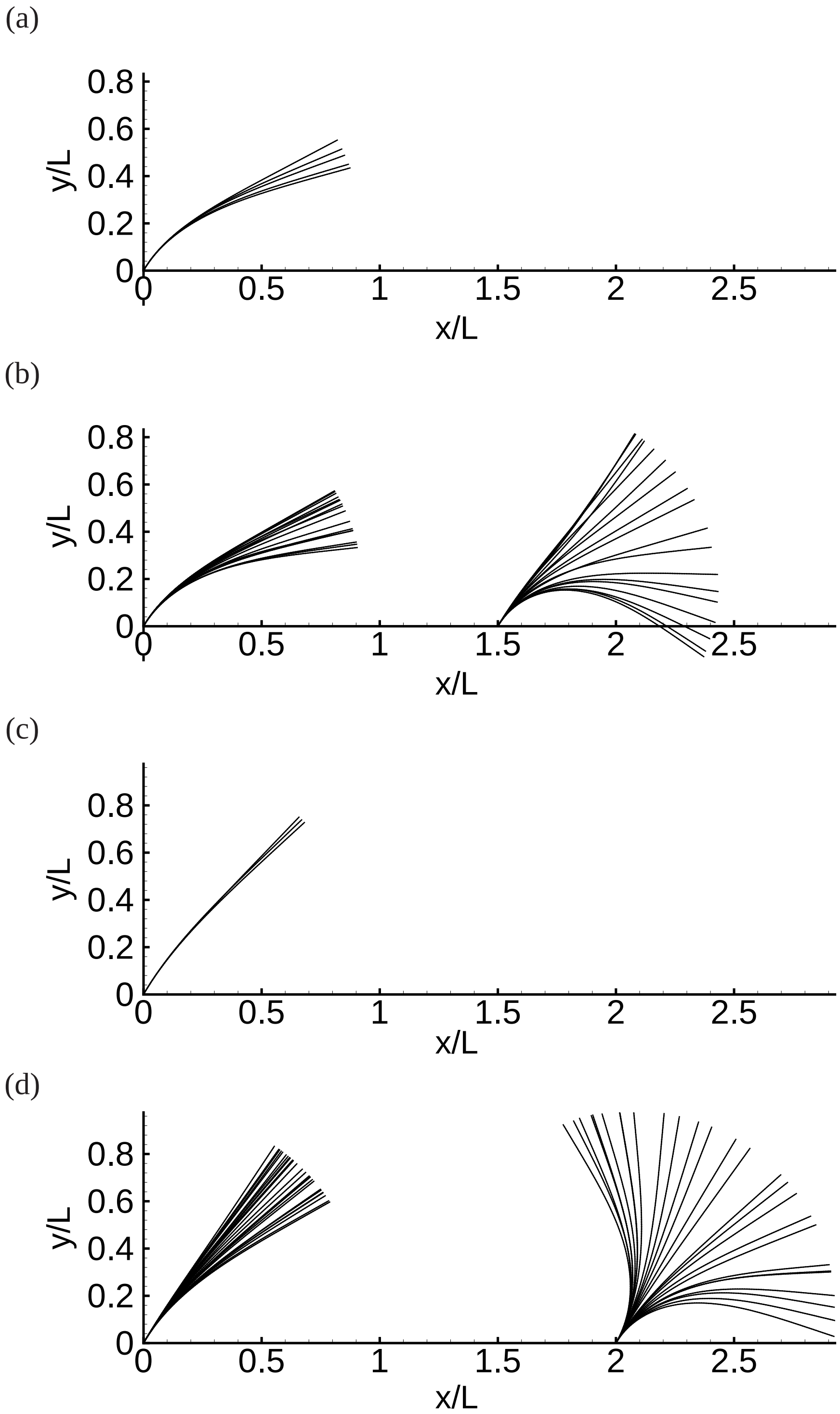

Figure 4.5: Deformation patterns of a single sheet (a,c) and two sheets at the resonant state (b,d), where the mass ratio is $m^* = 1$ in (a,b) and $m^* = 5$ in (c,d). The separation distance is $d/L = 1.5$ in (b) and $d/L = 2$ in (d).

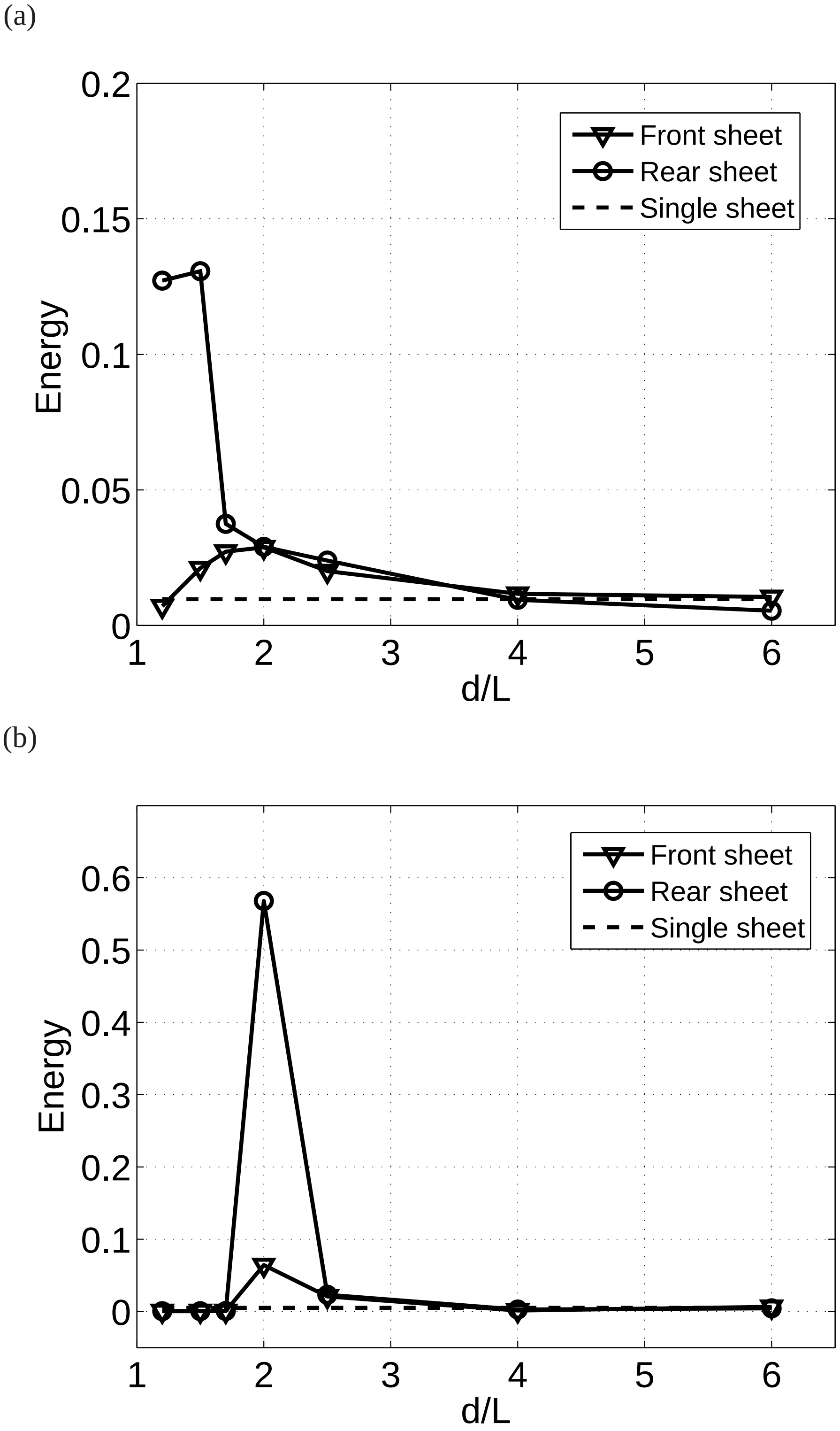

Figure 4.6: The normalized energy (by $\rho_f U^2 L^2$) of each sheet for (a) m^*=1 and (b) m^*=5, where the energy includes both the elastic potential and the kinetic energy.

normalized by $\rho_f U^2 L^2$. It can be seen that the trends in this figure are very similar to those in Fig. 4.4 for the vibration amplitude. That is, at the system resonance, the energy level of both sheets is much higher than that of the single sheet, and the rear sheet is more energetic than the front sheet.

In Fig. 4.7(a), we plot the ratio between the vibration frequency, f_v, and the natural frequency f_n to show the relationship between these two frequencies. Due to the vortex-shedding synchronization, which will be described later, the two sheets vibrate at the same frequency. Therefore, only one frequency graph is plotted for each mass ratio. In addition, the vibration frequency of the single sheet is also plotted as a reference. The result shows that the frequency of a single sheet is significantly higher than the natural frequency, with $f_v/f_n = 1.5$ for $m^* = 1$ and $f_v/f_n = 1.2$ for $m^* = 5$. The vibration frequency is not exactly the same as the natural frequency of the sheet because the oscillator has been detuned by vortex shedding and is engaged in the "soft" lock-in vibration [77]. When the two sheets are arranged in tandem, the frequency of the sheets becomes lower than that of the corresponding single sheet. At the system resonance, the oscillation frequency of the sheets reaches its lowest value, which is $f_v/f_n = 1.13$ for $m^* = 1$ and $f_v/f_n = 0.92$ for $m^* = 5$.

Fig. 4.7(b) shows the phase advance angle of the rear sheet with respect to the front sheet, where the phase angle changes from π to -0.75π as the separation distance is increased from $1.2L$ to $6L$. Therefore, the sheets are out of phase with each other when they are very close to each other. At the resonant state, the phase angle is 0.75π for $m^* = 1$ with $d/L = 1.5$, and it is 0.3π for $m^* = 5$ with $d/L = 2$. As shown later, such phase differences between the sheets will prevent the free stream from directly impacting on the rear sheet.

Fig. 4.8 shows the time course of the tip displacement, w/L, for the two sheets at the resonant state. For the first case where $m^* = 1$ and $d/L = 1.5$, we see that both the front sheet and the rear sheet experience steady oscillations and there is little cycle-to-cycle variation. For the second case where $m^* = 5$ and $d/L = 2$, we see that other than

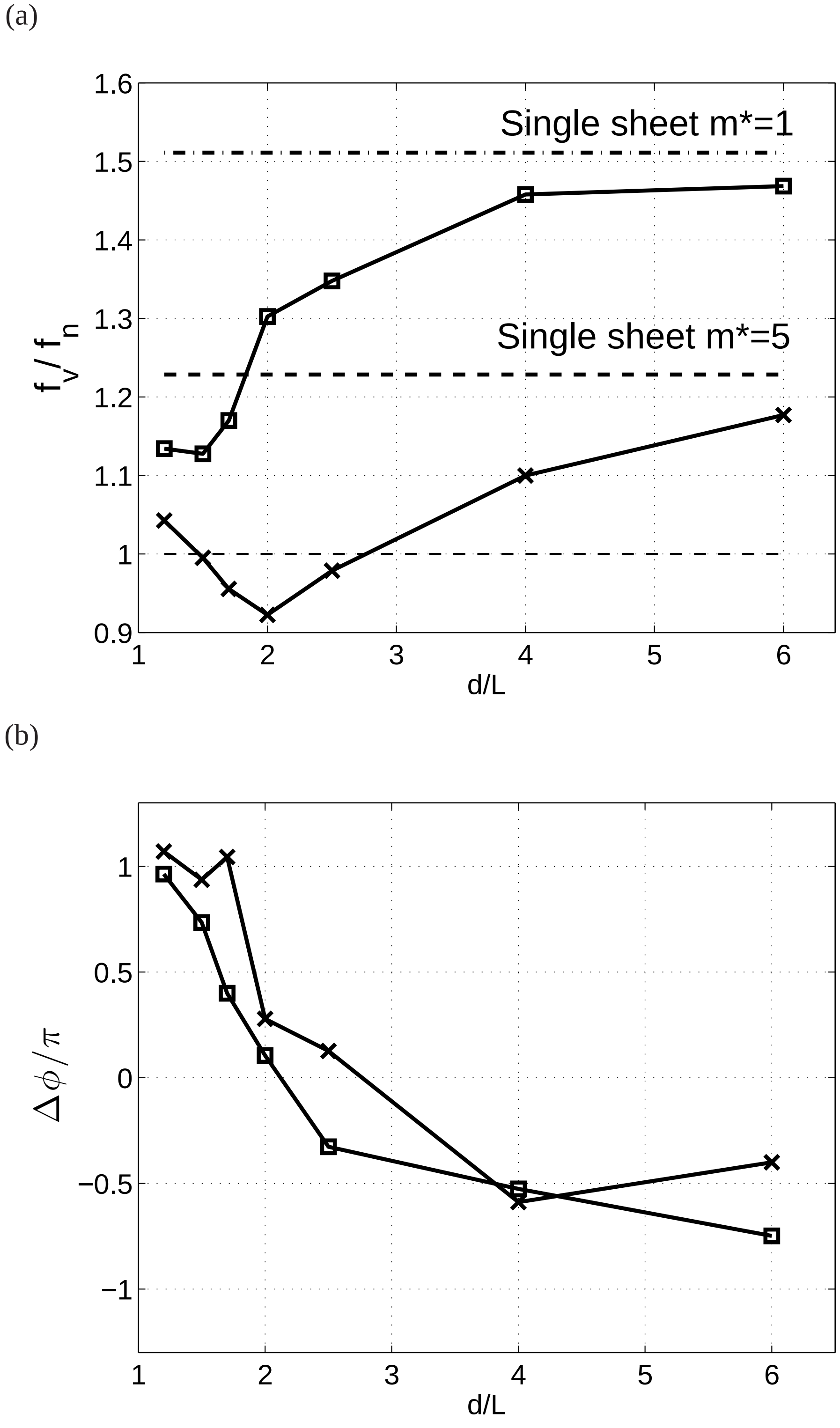

Figure 4.7: (a) The normalized vibration frequency, f_v/f_n, and (b) phase difference, $\Delta\phi$, for $m^* = 1$ (squares) and $m^* = 5$ (crosses). A positive value of $\Delta\phi$ means that the rear sheet is advanced with respect to the front sheet.

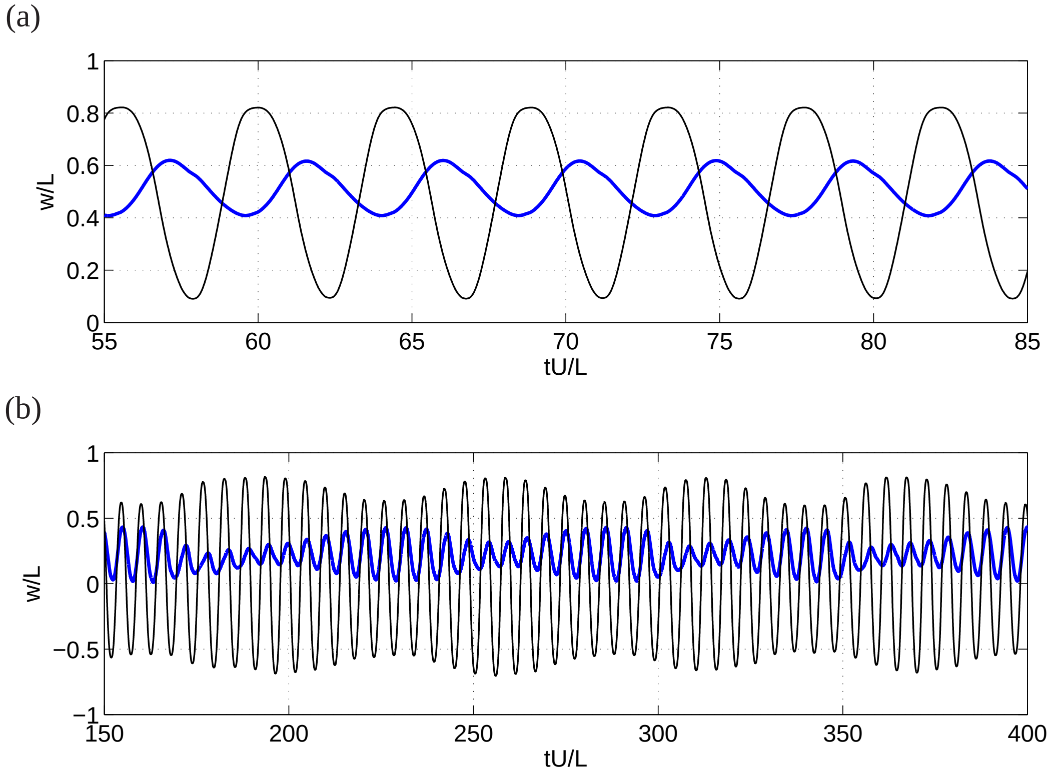

Figure 4.8: Time courses of the tip displacement, w/L, for the resonant cases: (a) $m^* = 1$ and $d/L = 1.5$ and (b) $m^* = 5$ and $d/L = 2$. Thick line: the front sheet; thin line: the rear sheet.

the main oscillation frequency, there is also a low-frequency waveform that governs the cycle-to-cycle variations of each sheet. Furthermore, the modulating wave for the front sheet is out of phase with that for the rear sheet. Therefore, when the rear sheet has large oscillation amplitude, the front sheet has low oscillation amplitude, and vice versa.

4.4 Mechanism of the system resonance

4.4.1 Flow analysis for the single sheet

Vibration of an elastic body has to do with the magnitude, frequency, and phase of the external load acting on the body. To better understand the behavior of the two sheets, we shall examine these force characteristics and study their relationship with the vortex shedding in the flow. For comparison, we first briefly discuss the result for the case of the single sheet. Fig. 4.9(a,b) shows the vortex shedding pattern for the single sheet at $m^* = 5$. The flow pattern for $m^* = 1$ is similar and is thus not plotted. For both mass ratios, the deformation of the single sheet is small, and the wake pattern is close to that of a rigid sheet. That is, the positive and negative vortices in turn pinch off from the sheet and form a vortex train in the wake.

Fig. 4.9(c,d) shows the fluctuating components of the pitch angle α and hydrodynamic torque T, α' and T', for the two mass ratios. The mean values of α and T are subtracted when calculating the fluctuating components. Furthermore, the torque has been normalized by $0.5\rho_f U^2 L^2$. Compared to $m^* = 1$, $m^* = 5$ has greater torque oscillations but it has a smaller vibration amplitude. The reason is that the sheets are stiffer for $m^* = 5$. Another observation is that for both mass ratios, T' is nearly out of phase with α'. That is, T' reaches the peak value when the sheet has its maximum deformation. Note that at the maximum deformation, the velocity of the sheet is at the lowest level. Therefore, the energy flow at the moment is limited because the force and the velocity mismatch. For a simple linear mass-spring-damper system that experiences resonant vibrations under a sinusoidal load, the external force has a phase lead of $\frac{\pi}{2}$ with respect to the displacement of the mass. In that case the work is done in an "efficient" manner because the force and the velocity of the mass would be in phase and both would reach the maximum values at the same time.

4.4.2 Resonant vibration of two sheets at $m^* = 5$ and $d/L = 2$

When the two sheets are placed in close range, the vortices shed from the front sheet and the vortices from the rear sheet interact with each other. We will discuss three factors that have contributed to the observed system resonance. First of all, the vortex-vortex and vortex-sheet interactions in the tandem arrangement alter the frequency of vortex shedding for both sheets and makes the frequency closer to the natural frequency of the sheets. Second, for the front sheet, the phase shift between its hydrodynamic

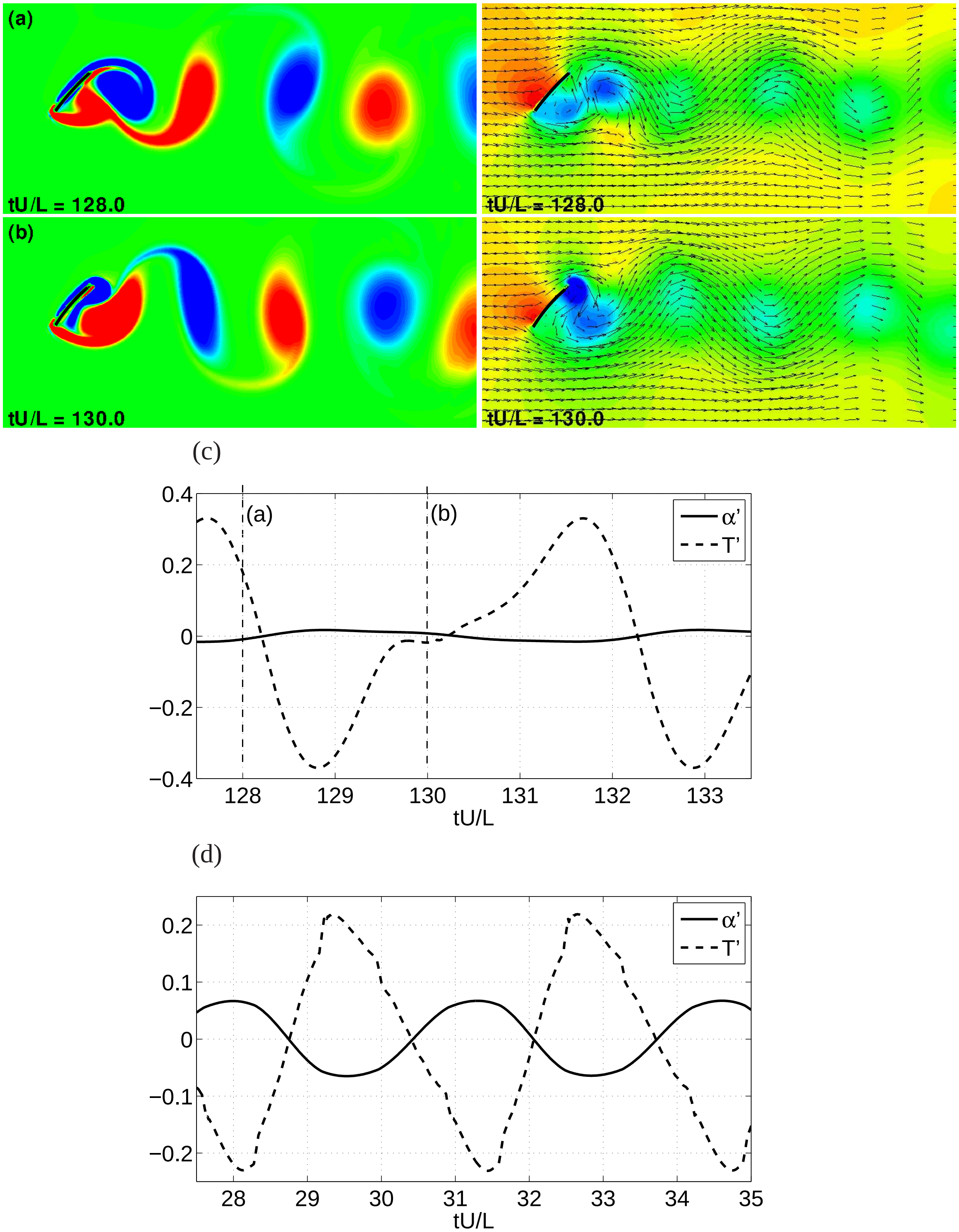

Figure 4.9: (a,b) Instantaneous vorticity field (left column) and pressure/velocity (right column) for the single sheet at $m^* = 5$. The vorticity ranges from $-3U/L$ to $3U/L$ and pressure from $-\rho_f U^2$ to $3\rho_f U^2$. (c,d) The fluctuating components of the pitch angle and the torque, α' and T', for $m^* = 5$ (c) and $m^* = 1$ (d).

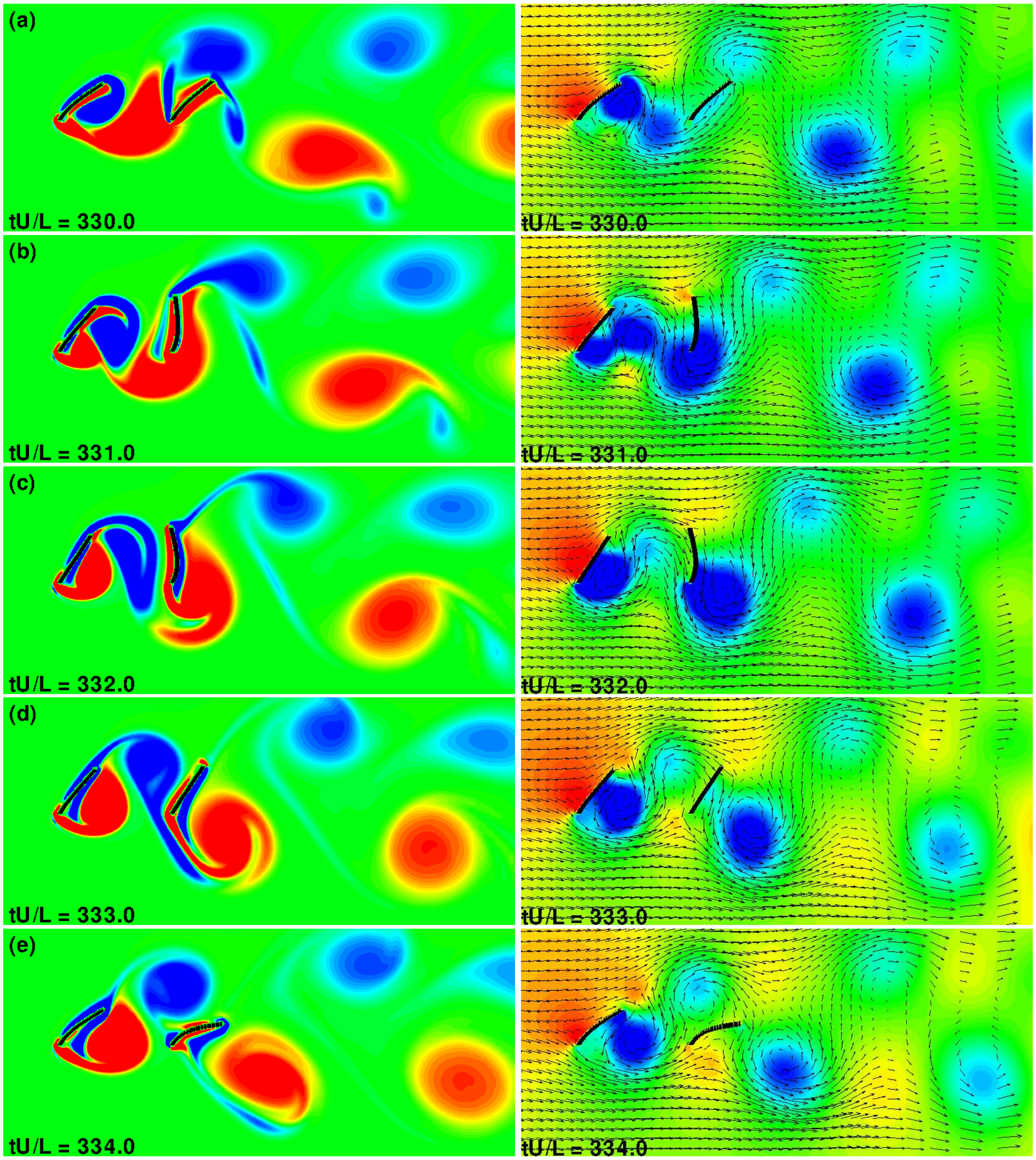

Figure 4.10: See next page for the caption.

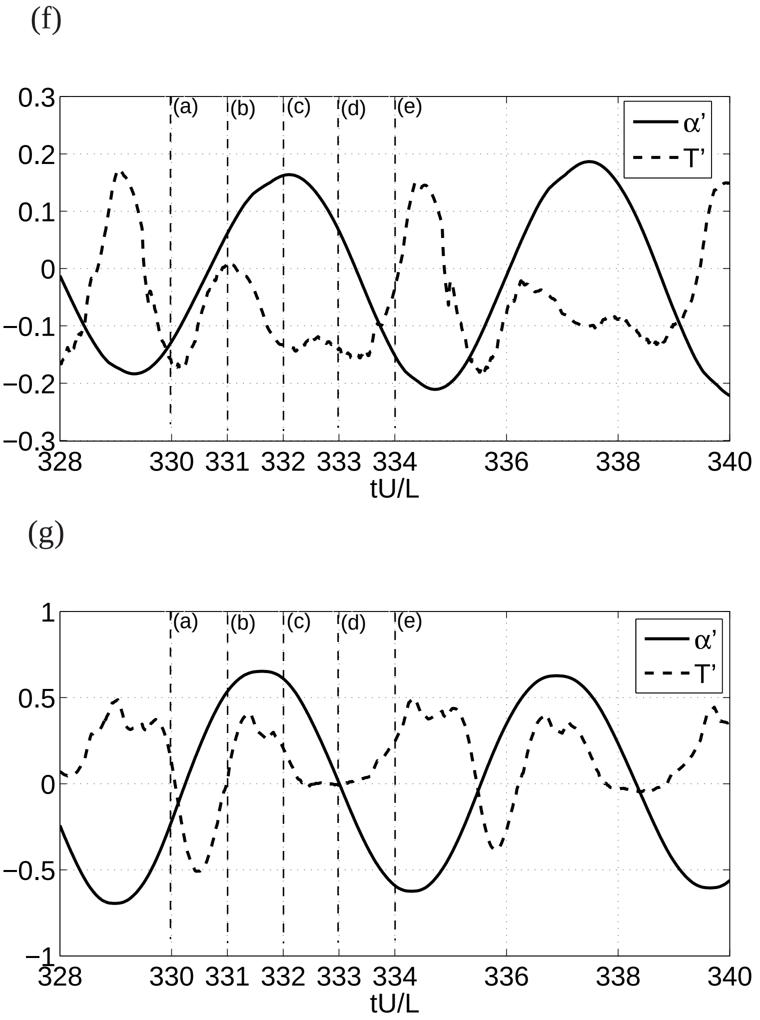

Figure 4.10: (a-e) Instantaneous vorticity field (left column) and pressure/velocity (right column) for two sheets at $m^* = 5$ and $d/L = 2$. The contour levels are the same as in Fig. 4.9. The fluctuation components of the pitch angle and torque are shown in (f) for the front sheet and (g) for the rear sheet.

torque and its pitching motion becomes beneficial for the energy transfer between the fluid and the sheet itself. Third, for the rear sheet, great force oscillations occur when the vortices shed from the front sheet merges with its own vortices in a coordinated manner. Next, we will discuss these effects along with the flow field in detail.

Fig. 4.10 shows the instantaneous flow at the system resonance for $m^* = 5$ and $d/L = 2$ during the time period between $tU/L = 330$ and 334. The velocity field and the pressure/vorticity contours are plotted for five selected time instances that are marked in Fig. 4.10(f,g), where the histories of α' and T' are shown. From the flow field we first notice that introducing a second sheet has completely modified the wake structure that is seen in Fig. 4.9(a,b) for the single sheet. Behind the two sheets, the wake exhibits two trains of vortices with the upper train consisting of negative (clockwise) vortices and the lower train consisting of positive (counterclockwise) vortices. Further inspection shows that these vortex trains are formed due to the vortices of the same signs, i.e., the negative vortices from the tip side of the two sheets, or the positive vortices from the base side, merging into one stronger vortex.

For the rear sheet, the coordinated vortex shedding causes great oscillations of the load on sheet. Fig. 4.10(g) shows that normalized T' oscillates between -0.5 and 0.5. For the corresponding single sheet, normalized T' is approximately between -0.37 and 0.35, as seen in Fig 4.9(c). Combining Fig. 4.10(a), (b), and (g), we see that the negative peak of T' takes place when the positive vortex from the base of the front sheet is growing in size and is connected to the shear layer below the rear sheet (Fig 4.10(a)). The merged vortex then pinches off from the front sheet and continues to develop from the rear sheet (Fig 4.10(b)). As seen in the pressure contour in Fig 4.10(b), this positive vortex forms a low pressure pocket below the rear sheet, which leads to negative T' on the sheet between times (a) and (b). Positive T' is generated between times (b) and (c) when a merged negative vortex is about to pinch off the tip of the rear sheet. Another positive peak of T' is caused after time (e) when a negative vortex shed from the front sheet passes over the rear sheet. These large-magnitude peaks cause great deformation to the rear sheet.

The reason for the front sheet to be excited is not as clearly seen as for the rear sheet. Comparing Fig. 4.10(f) and Fig. 4.9(c), we see that the torque oscillation of the front sheet is actually lower compared to that of the single sheet. For the front sheet, normalized T' varies between -0.17 and 0.17. However, compared the single sheet, the vibration frequency of this sheet is closer to the natural frequency. Fig. 4.7 shows that $f_v = 0.92 f_n$ for the two-sheet system while $f_v = 1.23 f_n$ for the single sheet. Note that for both the single-sheet and the two-sheet cases, the vortex shedding frequency is the same as the vibration frequency of the sheets. The reason for the reduced frequency in the two-sheet case is that the evolution and shedding of the vortices from the front sheet are somewhat slowed down due to the downstream obstruction of the rear sheet. For the rear sheet, there is a corresponding slowdown in the vortex evolution/shedding because its upstream flow is dominated by the vortex shedding from the front sheet. Therefore, both the front and the rear sheets in the present case are vibrating near the natural frequency, which is important for the resonance to occur.

In addition to the frequency of vortex shedding, we also examined the phase shift between the torque and the pitch angle of each sheet. As seen in Fig. 4.10(f,g), the torque oscillations of the two sheets are quite irregular compared to that for the single sheet, while the pitch angle oscillations are much more regular. For the front sheet there are two distinct time periods when the phase difference between T' and α' is close to $\frac{\pi}{2}$. The first period is between times (a) and (b), during which negative T' corresponds to a positive pitching rate, $\dot{\alpha}'$. The product of T' and $\dot{\alpha}'$ is thus negative, so the energy is being transferred from the sheet to the fluid at the moment. The second period is between times (c) and (e), during which negative T' corresponds to negative $\dot{\alpha}'$. The product is positive, so the energy is being transferred from the fluid to the sheet. Compared to the single sheet where the phase shift is nearly π, the current phase shift allows a larger amount of energy to be transferred with a lower torque. For the rear sheet, a similar phase shift can be seen between times (a) and (b), during which the energy is transferred from the sheet to the fluid. In summary, for the two sheets and especially the front sheet, the phase shift of the hydrodynamic load enhances the energy exchange between the fluid and the structure, and this effect has helped the resonance to occur.

Comparing the resonance of the thin sheets and that of two elastically mounted cylinders in tandem arrangement, we point out that there are significant differences between the underlying mechanisms. In the case of cylinders, the two bodies can vibrate transversely to the flow with a phase shift so that the rear body is periodically exposed to the free stream. According to Borazjani & Sotiropoulos [78], such an exposure leads to a pressure distribution around the rear cylinder that directs the flow through the gap region created by the position shift of the cylinders. Furthermore, when the transverse distance between the cylinders in their case is more than one diameter length, the gap flow causes the top-side shear layer of the front cylinder to be pushed into the bottom-side shear layer of the rear cylinder (or the bottom-side shear layer of the front cylinder into the top-side shear layer of the rear cylinder). They argued that such shear layer interactions cause great force oscillations and therefore large vibration amplitudes of the cylinders.

Unlike the cylinder case, in the present case the rear sheet is never directly subject to the free stream, which can be seen from Fig. 4.10. However, the interaction of the vortices shed from the same side of the two sheets can still lead to large-amplitude vibrations. Therefore, the transverse shift and the vertical gap are not necessary conditions for the bodies in tandem arrangement to undergo resonant vibrations. We also point out that even though in the present case there is no transverse gap between the sheets, there still exists a flow through the streamwise gap between the sheets. As shown by the velocity field in Fig. 4.10, and the gap flow between the two sheets may take different forms, e.g., entering the gap region from one side and leaving from the other side (see Fig. 4.10(a,d)), or entering and leaving from the same side (see Fig. 4.10(c)). In Borazjani & Sotiropoulos [78], the gap flow always enters from one side and leaves from the other. In the present case, the gap flow is important because it affects the vortex development for both the front and rear sheets.

4.4.3 Resonant vibrations of two sheets at $m^* = 1$ and $d/L = 1.5$

For the resonant case with $m^* = 1$ and $d/L = 1.5$, the interaction between the vortices and the sheets is in general similar to what we have described for the case of $m^* = 5$. We plot the typical flow field and corresponding α' and T' in Fig. 4.11 for this low-mass-ratio case. Different from $m^* = 5$, the oscillations of α' and T' are nearly periodic and exhibit little cycle-to-cycle variation. Another difference in this case is that the two sheets are oscillating out of phase. Therefore, when the front sheet is up against the free stream, the rear sheet is bent backward to its maximum extent. On the other hand, when the front sheet is bent backward, the rear sheet is up and is partially exposed to the free stream. This situation therefore bears some similarity to the cylinder case. However, after examining the vibration frequency, force magnitude and phase shift, we notice the similar features as described previously for $m^* = 5$. For example, the vortex shedding frequency in this case is adjusted toward the natural frequency of the sheets, i.e. from $f_v/f_n = 1.5$ for the single sheet to $f_v/f_n = 1.13$ for the two sheets; the rear sheet experiences large torque oscillations; and although T' on the front sheet has reduced magnitude, it has a phase shift which helps with energy exchange. Therefore, the three factors we discussed earlier also apply here for $m^* = 1$.

4.5 Further discussions

4.5.1 Effect of the Reynolds number

To see the effect of the Reynolds number on the resonant behavior of the two sheets, we performed two additional series of simulations for $Re = 100$ and $Re = 500$ at mass ratio $m^* = 5$. Fig. 4.12 shows the time-averaged amplitudes of oscillation for both sheets. It can be seen that as the Reynolds number is increased from 300 to 500, the critical separation distance for the system resonance does not change very much. In addition, the oscillation amplitude of the rear sheet remains around $A_m/L = 0.65$. However, the oscillation amplitude of the front sheet has increased nearly twice. When the Reynolds number is reduced to 100, Fig. 4.12 shows that the resonance region is shifted to the right and has become much wider. Furthermore, the oscillation amplitude of each sheet is smaller than that of the corresponding sheet at $Re = 300$. Flow visualization shows that at $Re = 100$, the vortices from the front sheet need a larger space to develop

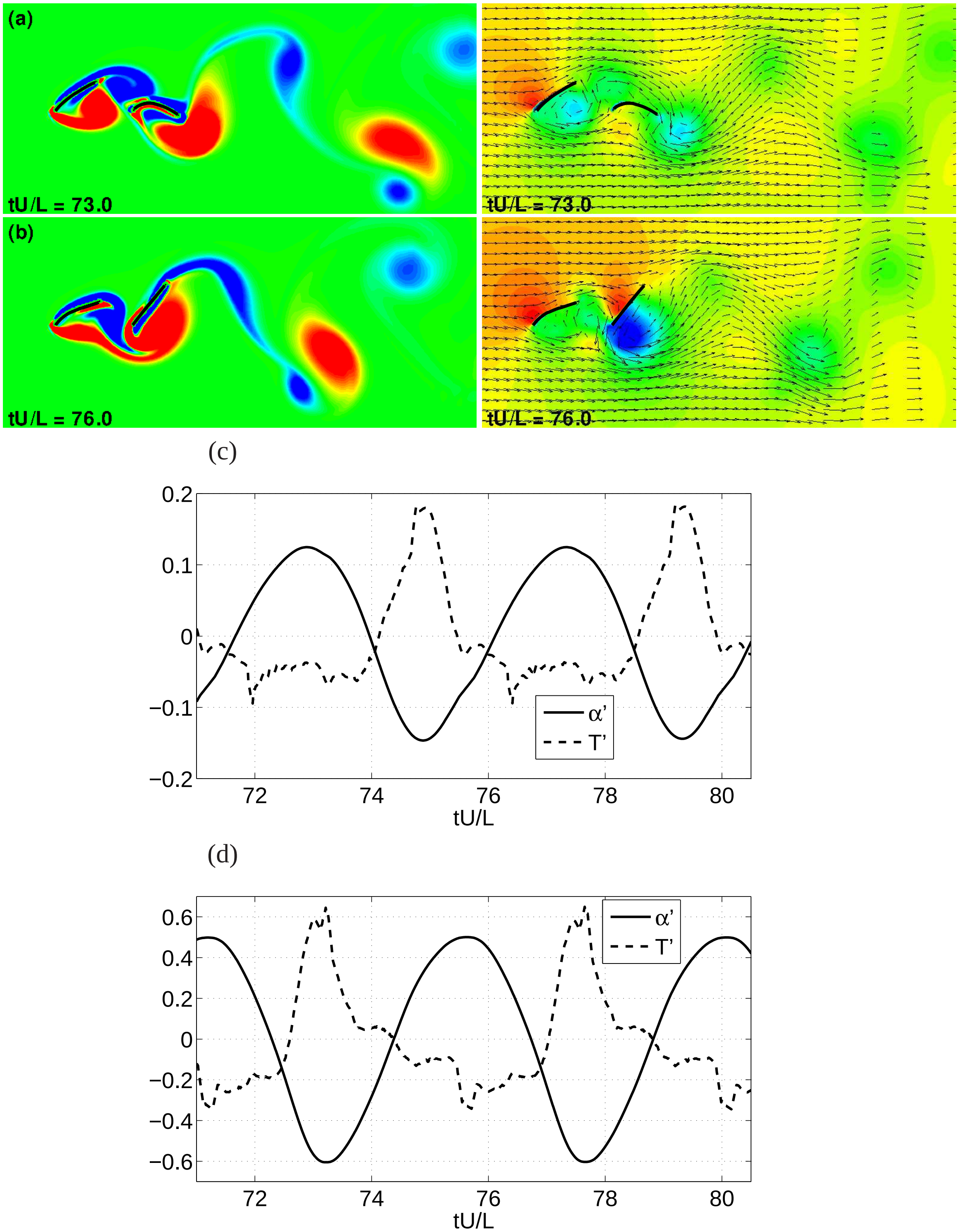

Figure 4.11: (a,b) Instantaneous vorticity field (left column) and pressure/velocity (right column) for two sheets at $m^* = 1$ and $d/L = 1.5$. The contour levels are the same as in Fig. 4.9. The oscillations of the pitch angle and torque are shown in (c) for the front sheet and (d) for the rear sheet.

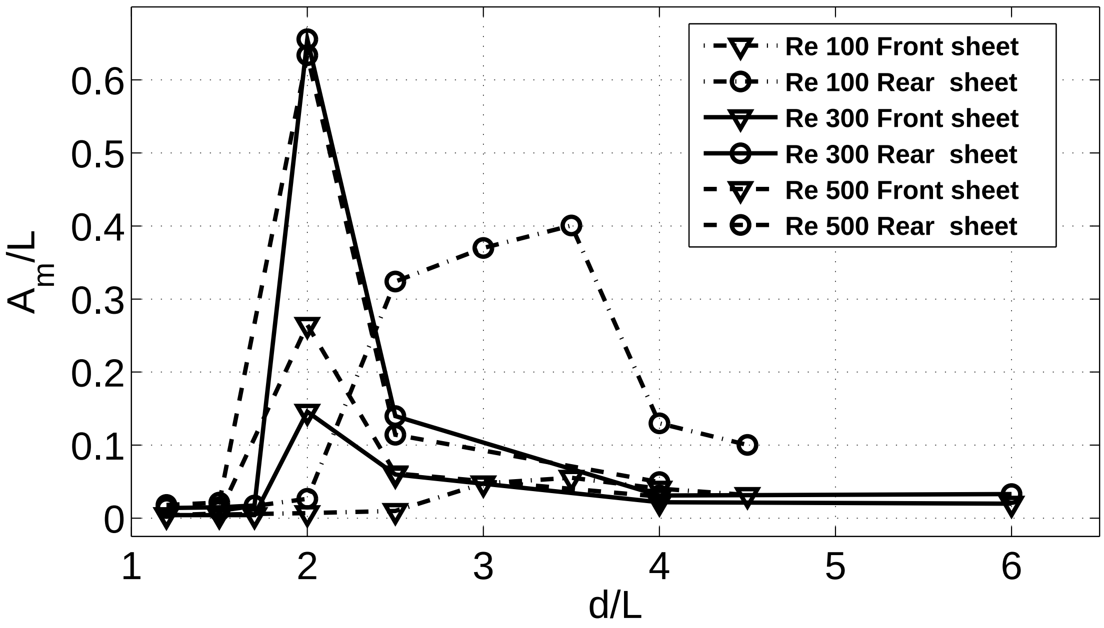

Figure 4.12: Effect of the Reynolds number on the oscillation amplitude of the two sheets at $m^* = 5$.

in this low-Re case, and the separation distance thus has to be increased for the vortex synchronization to take place.

4.5.2 Effect of the Strouhal number

The Strouhal number, St_n, has so far been fixed at 0.2. Previously, this parameter has been studied in detail by others in the context of one or two cylinders [70, 77, 78]. Note that the inverse of St_n, i.e., $St_n^{-1} = U/(f_n L)$ or the reduced velocity, may have been used in those studies. In the case of cylinders, there is a range of St_n, i.e., the lock-in region, where the resonance would occur. Furthermore, the lock-in region for the two cylinders in tandem arrangement is significantly different from that of the single cylinder [78]. To see whether a similar effect of St_n exists in the present problem, we set $d/L = 2$ for $m^* = 5$ and $d/L = 1.5$ for $m^* = 1$ and we vary St_n in the simulation. The result is shown in Fig. 4.13 for $Re = 300$.

The first observation from Fig. 4.13 is that for both mass ratios, there is indeed a range of Strouhal numbers at which both the front and rear sheet are excited and have large vibration amplitudes. In addition, compared to the corresponding single sheet, the lock-in regions of the two sheet are narrower and have been shifted to lower Strouhal numbers. In all the cases considered here, the rear sheet always has a larger vibration amplitude than the front sheet, while in the case of two cylinders a larger amplitude could happen for the front cylinder [78]. The closest case here is in Fig. 4.13(b), where the front and rear sheets have a similar amplitude at $St_n = 0.125$.

Fig. 4.14 shows the ratio between the vibration frequency and the natural frequency. Since the vortex shedding frequency, and thus the vibration frequency, is relatively constant, increasing the Strouhal number leads to decrease of this frequency ratio, which is seen from the figure. For both mass ratios, the two-sheet system has a lower vibration frequency than the single sheet at the same Strouhal number.

4.6 Multiple sheets in tandem arrangement

A natural question is whether a similar resonant behavior can also happen when more than two sheets are aligned in the same manner. If such resonance exists also for multiple sheets, then the energy in the unsteady flow may be harvested more efficiently. From the result described earlier, the resonance of the sheets as a group may not occur since the vortex structure in the merged wake behind the two sheets has been largely modified from that of the single sheet. Nevertheless, we ran a few simulations to verify this speculation. Fig. 4.15(a) shows the oscillation amplitude averaged for $n = 1, 2, 3, 5$ sheets at mass ratios $m^* = 1$ and 5. At $m^* = 5$, the oscillation amplitude drops quickly when $n \geq 3$. The flow visualization shows that initially all the sheets located downstream are greatly excited by the interaction among the sheets. However, after about 40 cycles the third sheet settles down to a low-amplitude motion, and the second sheet also has significantly reduced oscillation. The reason is that the vortices shed from

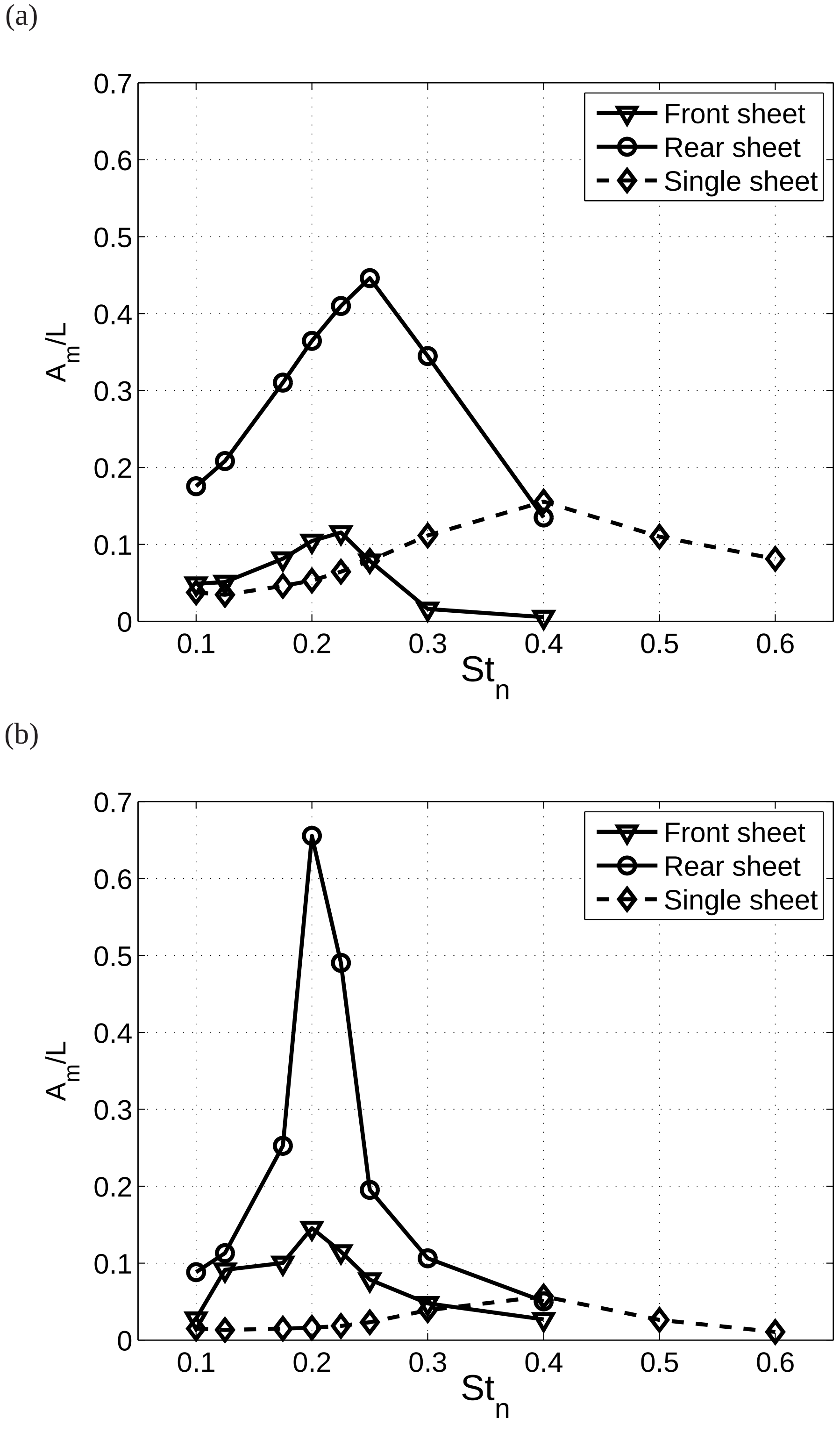

Figure 4.13: Effect of the Strouhal number St_n for (a) $m^* = 1$ and $d/L = 1.5$ (b) $m^* = 5$ and $d/L = 2$. The Reynolds number is $Re = 300$.

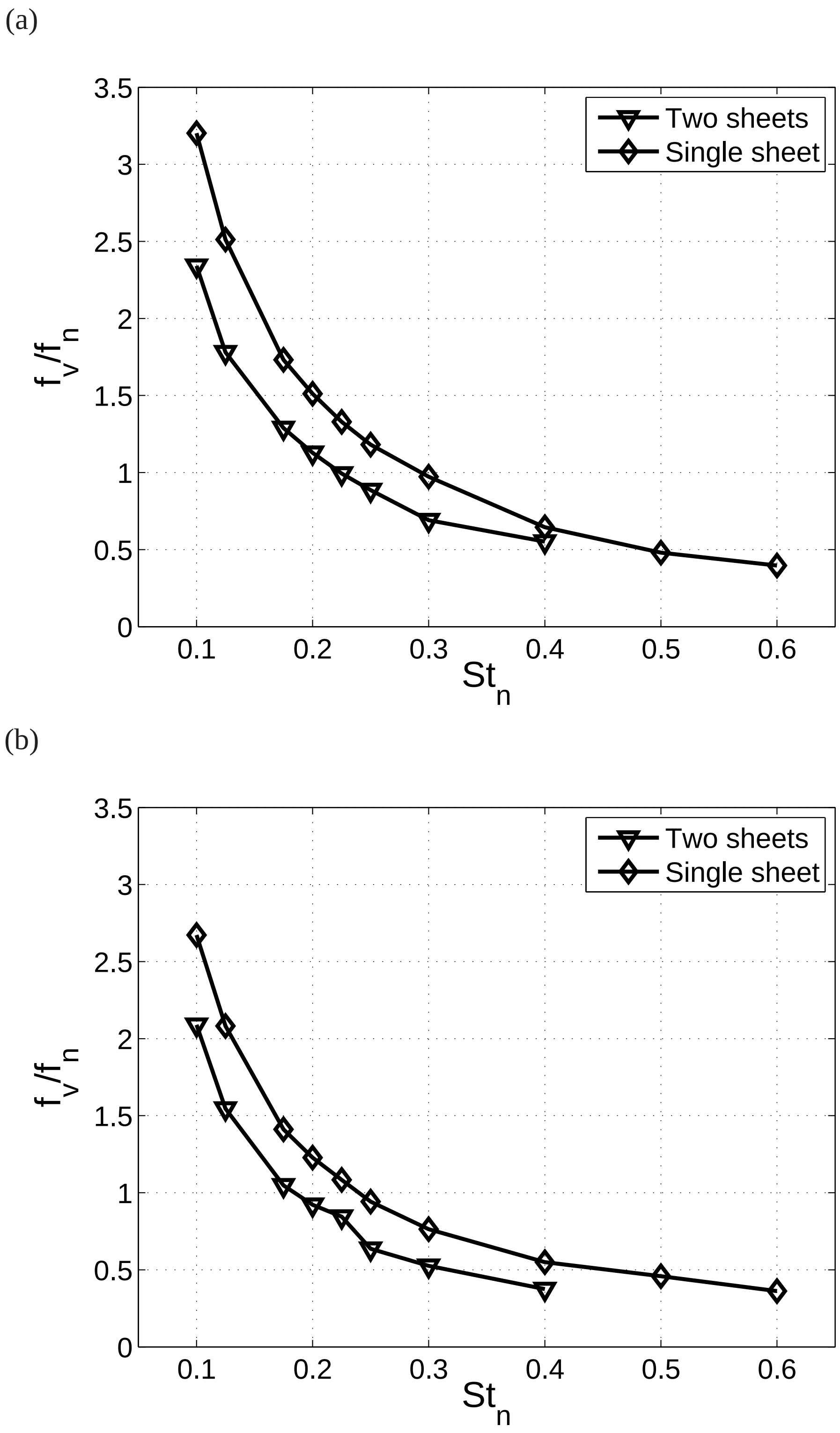

Figure 4.14: The frequency ratio of the sheets at different Strouhal numbers for (a) $m^* = 1$ and $d/L = 1.5$ (b) $m^* = 5$ and $d/L = 2$. The Reynolds number is $Re = 300$.

the second sheet does not have strong interaction with the third sheet and in addition, the vibration frequency of the three-member group has been reduced to $f_v/f_n = 0.85$ (Fig. 4.15(b)).

For $m^* = 1$, Fig. 4.15(a) shows the oscillation amplitude of the group becomes greater for $n = 3$ and then levels off. Fig. 4.15(a) shows that the oscillation frequency of the sheet at this mass ratio is around the natural frequency for $n = 3$ and $n = 5$. As an example, we plot the vorticity and shape of the sheets at an instantaneous moment in Fig. 4.16 for $n = 5$. The group form a regular vibration pattern: sheets 1, 3, and 5 are in phase with each other, but sheets 2 and 4 are out of phase with those three. The animation shows that each downstream sheet interacts with the vortices from the sheet immediately in front of it, and the interaction becomes weaker for the sheets located further downstream.

From these results, we conclude that the parameters that lead to the system resonance of two sheets may not lead to resonance of multiple sheets of the same properties and configuration. In order to excite all the sheets in a group and explore its maximum performance, one should adjust the parameters such as the individual spacing of the sheets and probably optimize the group as a whole system. One example of such study is by Hobbs and Hu [86], who studied the power generation performance of a four-cylinder array by varying both the separation distance and the flow speed (thus the vortex shedding frequency). Alternatively, different arrangement patterns could be considered, e.g., a staggered placement in the transverse direction, so that the interaction between the vortices and the downstream sheets may be strengthened.

Finally, we point out that the current study is limited to two dimensions and the three-dimensional effects due to flow instability or finite aspect ratios are not included. In addition, only low Reynolds numbers (less than 1000) are considered, and the inclination angle of the sheets is fixed. Explorations beyond these limitations will be considered in the future work.

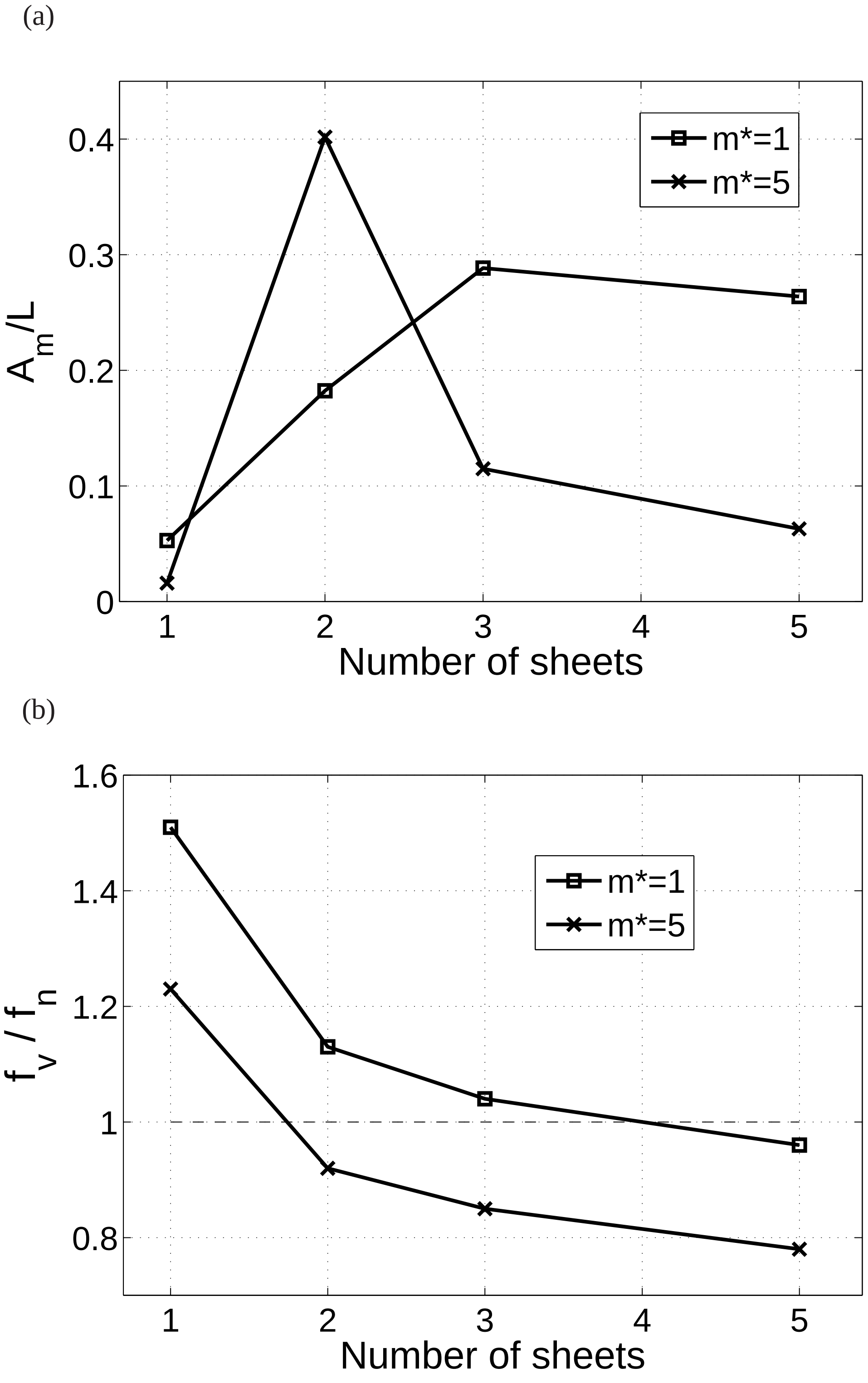

Figure 4.15: Multiple sheets in tandem arrangement where $d/L = 1.5$ for $m^* = 1$ and $d/L = 2$ for $m^* = 5$. (a) The averaged oscillation amplitude; (b) the vibration frequency of the sheets. The Reynolds number and the Strouhal number are $Re = 300$ and $St_n = 0.2$, respectively.

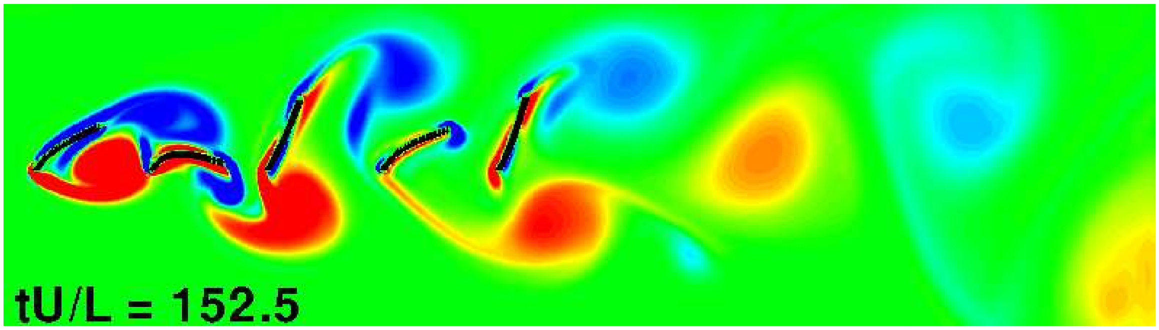

Figure 4.16: Vibration pattern and vorticity field for five sheets at $m^* = 1$, $d/L = 1.5$, $Re = 300$ and $St_n = 0.2$.

4.7 Conclusion

We have performed a two-dimensional numerical simulation of the hydrodynamic interaction between two elastic sheets mounted in tandem in a flow. The goal is to explore the energy-harvesting potential of the sheets through vortex-induced vibrations. The result shows that at a particular distance that depends on the mass ratio, both sheets are excited and the system exhibits a resonant behavior. At the resonant state, the vibration amplitude of both sheets can be an order of magnitude higher than that of the corresponding single sheet. Different from two elastically and in tandem mounted cylinders that oscillate perpendicularly to the free stream, the two sheets are fixed at the base and do not have a relative shift in position. As a result, the free stream may not directly impinge on the rear sheet. Nevertheless, the two sheets can still experience a similar resonant vibration that is seen in the case of two cylinders. To investigate the underlying mechanism of resonance, we examined the instantaneous flow field and force characteristics of each sheet. It was found that through the hydrodynamic interaction, the vortex shedding frequency, which is the same as the vibration frequency, is adjusted to better match the natural frequency of the sheets. Furthermore, the vortex-vortex synchronization causes stronger force oscillations on the rear sheet and greatly intensifies its vibration. For the front sheet, the phase of the torque on the sheet is shifted so that the energy transfer between the fluid and the sheet is enhanced. By studying the effect of the Strouhal number, we found that the resonant behavior is consistent within the lock-in region.

The optimal configuration that causes resonance of the two sheets does not necessarily lead to resonance of multiple sheets that have the same material properties and the same separation distance as in the two-sheet case. The interaction of the downstream sheets could become weak due to modification of the upstream vortical structures by the first two sheets. This result implies that in order to improve the overall energy-harvesting potential of multiple sheets, one should adjust the governing parameters from a system perspective.

CHAPTER 5

NUMERICAL SIMULATION OF DROPS INSIDE AN ASYMMETRIC MICROCHANNEL WITH PROTRUSIONS

5.1 Background

Drops in microfluidic channels have been recently explored as a highly controllable platform for applications in the measurement of chemical reaction kinetics [12]. In these applications, mixing of agents inside the drops is often needed for the device to perform its function. However, mixing in microfluidic channels is typically slow because the Reynolds numbers involved are small and convective mixing is limited. To enhance the mixing rate in microchannels (not necessarily involving drops), both active and passive mixers have been developed in the past. Active mixers include acoustic [87], temperature [88], or magneto [89] actuation approaches and thus require incorporation of additional system components. Passive mixers typically reply on the certain geometrical features of the microchannel, e.g., a serpentine channel, that are made without introducing extra steps in the fabrication process [90]. A number of previous studies have focused on the passive mixing that involves drops. For example, Bringer *et al.* [12] provided a comprehensive review of the mixing mechanisms and the scaling of the mixing time for both straight and winding channels. Muradoglu *et al.* [91] numerically studied the mixing inside a drop passing through a serpentine channel and investigated the effects of the Reynolds number, capillary number, and viscosity ratio. In another study, Stone & Stone [92] simulated the mixing inside a drop through serpentine channels by simplifying the flow to superposition of uniform and shear flows.

Liau *et al.* [93] introduced single-sided wall protrusions, or “bumps”, into both straight and serpentine channels, illustrated here in Fig. 5.1, and found that the periodic

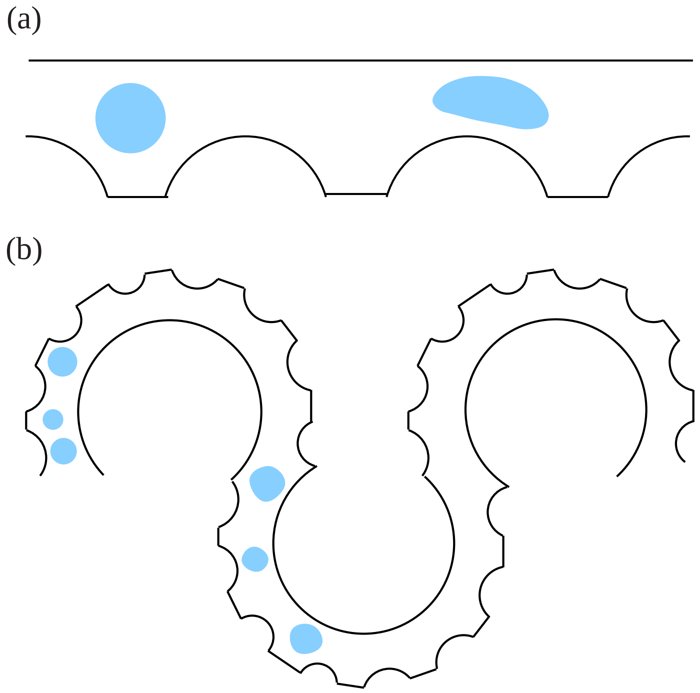

Figure 5.1: Straight and winding channels with bumps on the wall to enhance the mixing inside the droplets. The idea was presented in Liau *et al.* [93].

protrusions significantly enhance mixing inside the drop passing through the channels. To explain the mixing enhancement, Liau *et al.* [93] provides three factors that may have played a role: (1) the asymmetry of the flow and shear stress in the constriction region, (2) the surfactant distribution caused by the asymmetric stretching of the droplet surface, and (3) the non-Newtonian effect of the drop fluid. Despite the insightful view, their explanation was qualitative, and a parametric study would be helpful to clarify these effects. Given that previous studies on dynamics of drops through a channel constriction typically focus on symmetric geometries [e.g. 94], in the current work we aim to study the effect asymmetric constriction on the drop deformation and on the streamline pattern inside the drop. In addition, we will consider different shapes of the wall protrusion and study their effect on the flow pattern.

Computational modeling of two immiscible fluids in contact in an arbitrary geometry is in general a challenging task since it needs to handle the interface between the two fluids and also the interface between the fluids and solid surface. In the existing numerical methods, the mesh discretizing the domain, either a curvilinear grid or an unstructured grid, is typically chosen to conform to the fluid-solid interface so that the no-slip and no-penetration conditions at the wall can be imposed straightforwardly. On the other hand, the interface between the two fluids can be handled by several approaches that do not require the mesh to be conformal to the morphological change of the interface. Based on how the fluid–fluid interface is traced, these approaches include the following: (1) the Lagrangian mesh approach, where the interface is represented by a set of marker points moving with the local fluid [22]; (2) the volume-of-fluids (VOF) method, where the interface is represented by the volume fraction of the fluids [18]; (3) the level-set function, where the interface is represented by the zero-level contour of a distance function [19]; and (4) the phase-field method, where the interface is represented by the chemical energy level of the fluids [20]. Among these approaches, method (2)-(4) uses a scalar variable convected by the flow to trace the interface implicitly, and they have the inherent capability of handling topological changes of the interface.

For complex and moving boundaries of solid bodies, the immersed-boundary method based on a fixed Cartesian grid has been developed and utilized extensively in various applications [26, 29]. Compared with the curvilinear or unstructured grid based methods, the advantages of the immersed-boundary method include simple mesh generation and efficient computational algorithms that are based on the Cartesian grid. Among several existing variants of the immersed-boundary method are those categorized as the sharp-interface method, where the effect of the solid surface is incorporated as a direct forcing through interpolation [26]. Compared to the diffuse-interface immersed-boundary method where the surface traction is smeared and the accuracy is correspondingly reduced [29], the sharp-interface method is usually second-order accurate.

One way to simulate the fluid–solid–fluid interface is to combine the immersed-boundary method for solid bodies and the interfacial treatment for multiphase flows so that the advantages of each method can be shared. Such a method indeed has been developed before. For example, Liu *et al.* [95] presented a two-dimensional (2D)

Cartesian grid based sharp-interface method to simulate drop impact and spreading on solid surfaces of arbitrary shape. In their method, both the fluid–fluid and fluid–solid interfaces are traced by level-set functions. Yang & Stern [96] developed a sharp-interface/level-set Cartesian grid method for large eddy simulations of three-dimensional (3D) two-phase flows interacting with moving bodies. In both works, the ghost-fluid method [97], is used to treat the jump conditions at the fluid–fluid interface, which requires designation of ghost cells near the interface and explicit incorporation of the interfacial discontinuity into the finite-difference approximation of the governing equation. A simple alternative to their approach is to use the continuous surface force model (CSF) [30] to regularize the traction jump and solve the governing equation in a unified approach.

In the present work, we combine the level-set method for the fluid-fluid interface and a sharp-interface immersed-boundary method for the solid boundary, and we adopt the CSF model to incorporate the traction jump due to the surface tension. The numerical method has been described in Chapter 2. Here the method will be used to simulate the drops passing through channels with asymmetric constriction.

5.2 Validation

The current numerical method has been implemented in both 2D and 3D. To validate the method, we consider three problems that involve non-trivial geometries of the fluid–fluid and/or fluid–solid interfaces.

5.2.1 Leveling of an interface in a wavy channel

The leveling of a fluid–fluid interface under the effect of surface tension in a corrugated 2D channel is firstly considered. The problem is illustrated in Fig. 5.2(a), where the horizontal channel has a straight top wall and a sinusoidal bottom wall described by $y_w = a_w \cos(kx)$, where a_w is the amplitude, $k = 2\pi/L$ is the wavenumber, and L is the

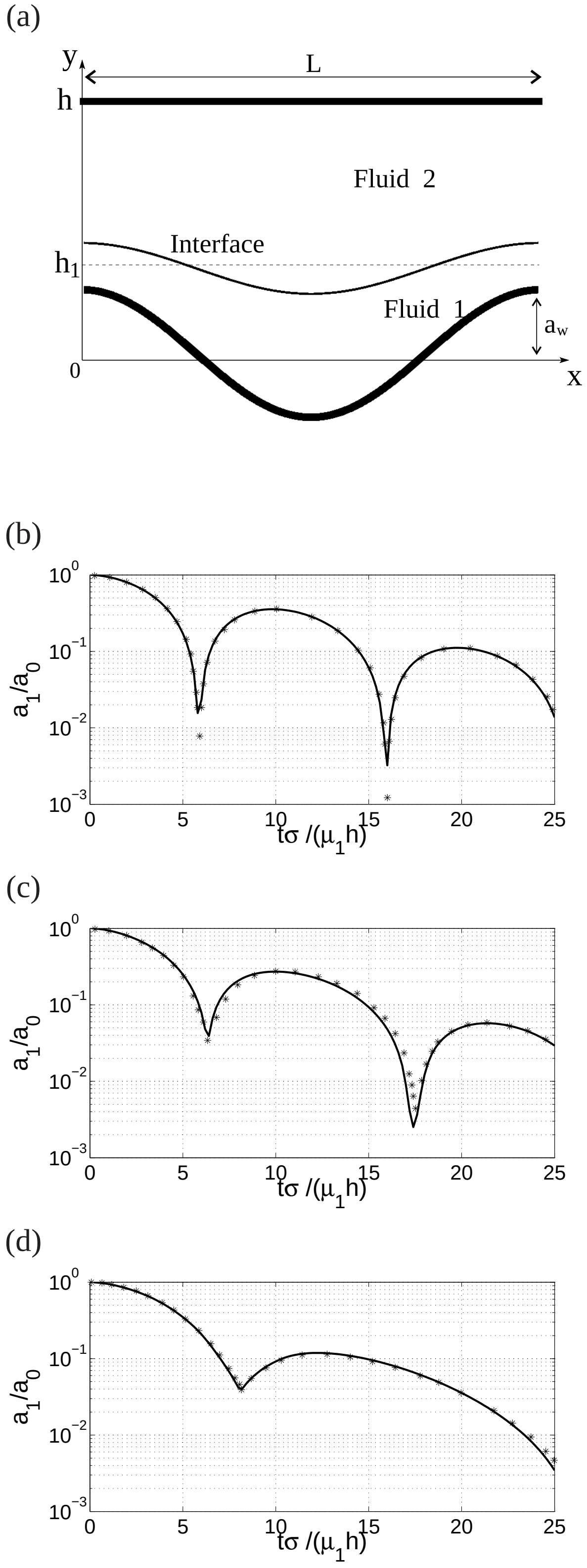

Figure 5.2: (a) Illustration of a two-layer flow in a wavy channel. (b-d) Evolution of the interfacial amplitude in time for $a_w/h = 0$ (b), 0.15 (c), and 0.25 (d). Solid line: current result; symbols: result from Luo *et al.* [98].

wavelength. The two-fluid interface is initially placed at

$$y = h_1 + \epsilon\, h\ \cos(kx) \tag{5.1}$$

where h is the channel width, $h_1 = h/3$ is the mean thickness of fluid 1, and $\epsilon = 0.1$ is the amount of initial perturbation. The fluids are initially quiescent, and there is no any external force. The fluid interface starts to evolve due to the stabilizing effect of the surface tension in this problem. Periodic conditions are applied at the left and right boundaries.

To apply the current numerical method, the uneven wall is represented with piecewise line segments and is treated as an immersed solid boundary. A single-block Cartesian grid is used to discretize the computational domain that ranges from $-L/2$ to $L/2$ in x and from $-a_w$ to h in y. Equal density fluids are considered so that $\rho_1 = \rho_2 = \rho$. For the case study, the dimensionless parameters are chosen as $L/h = \pi/2$, $\lambda = \mu_2/\mu_1 = 0.2$, and $Re = \rho\sigma h/\mu_1^2 = 200$. The surface tension σ is assumed to be constant along the interface. A uniform grid is used for the simulation with the grid intervals $\Delta x/h = \Delta y/h = 0.02$, and the time step is $\Delta t = 0.0025\mu_1 h/\sigma$. Previously, this problem has been solved using a curvilinear grid that conforms to the wavy wall by Luo *et al.* [98]. In that study, the two-fluid interface is treated using a variant of Peskin's immersed-boundary method [29], and a second-order finite-difference method is used to discretize the governing equation. Their result is used here to validate the current simulation.

Fig. 5.2(b-d) shows evolution of the amplitude of the interface, a_1/a_0, against the dimensionless time, $t\sigma/(\mu_1 h)$. Here a_1 is the amplitude of the interface, and $a_0 = \epsilon h$ is the initial amplitude. The result is plotted on a log-linear scale and is shown for three different wall amplitudes, a_w/h=0, 0.15 and 0.25. Due to a combined surface tension and inertial effect, the fluid interface first levels off but then overshoots by reversing its waviness, resembling a standing wave under the gravitational effect. The wave amplitude thus oscillates up and down in time as shown in the figure. However, due to presence of the viscous damping, the wave amplitude becomes smaller and smaller and would eventually diminish. As the wall amplitude is increased from a_w/h=0 to a_w/h=0.25, the oscillation period is elongated and the interface movement slows down, and in addition, the wave oscillation decays in a faster rate. Comparing the current result with that from Luo *et al.* [98], we see that they agree with each other very well.

5.2.2 Deformation of a 3D droplet in simple shear flow

In the second test, we consider the dynamic deformation of a 3D drop in a linear shear flow as shown in Fig. 5.3(a). The drop is initially spherical and has a radius R_0. The two fluids have equal densities. Under the shearing effect, the drop assumes an ellipsoidal shape with three characteristic axes. The problem is governed by two dimensionless groups, the viscosity ratio $\lambda = \mu_2/\mu_1$, where μ_2 and μ_1 are respectively the viscosity of the drop and the viscosity of the continuous fluid, the capillary number is defined as $Ca = \mu_1\dot{\gamma}R_0/\sigma$, where $\dot{\gamma}$ is the shear rate, and the Reynolds number is defined as $Re = \rho\dot{\gamma}R_0^2/\mu_1$ and is set at $Re = 0.2$.

Taylor [100, 101] introduced a non-dimensional parameter $D = (L - B)/(L + B)$ to describe the shape of the ellipsoid at the steady state in the limit of Stokes flow, where L is the length of the principal axis and B the length of the minor axis in the xz-plane (as in Fig. 5.3(a)). He derived the relationship between D and the governing parameters λ and Ca,

$$D = Ca\,\frac{19\lambda + 16}{16\lambda + 16}. \tag{5.2}$$

At the steady state, the viscous and capillary effects balance with each other. Taylor's equation matches the experimental result well when $Ca \ll 1$. As Ca is further increased beyond some critical value, the drop deviates from the ellipsoidal shape and pinch-off may appear in the middle of the elongated drop, eventually causing it to break up [102]. In the present simulation, a cubic box of length $2R_0$ is used for the computational domain. The mesh resolution is $R_0/32$ in all three directions, and the time step size is

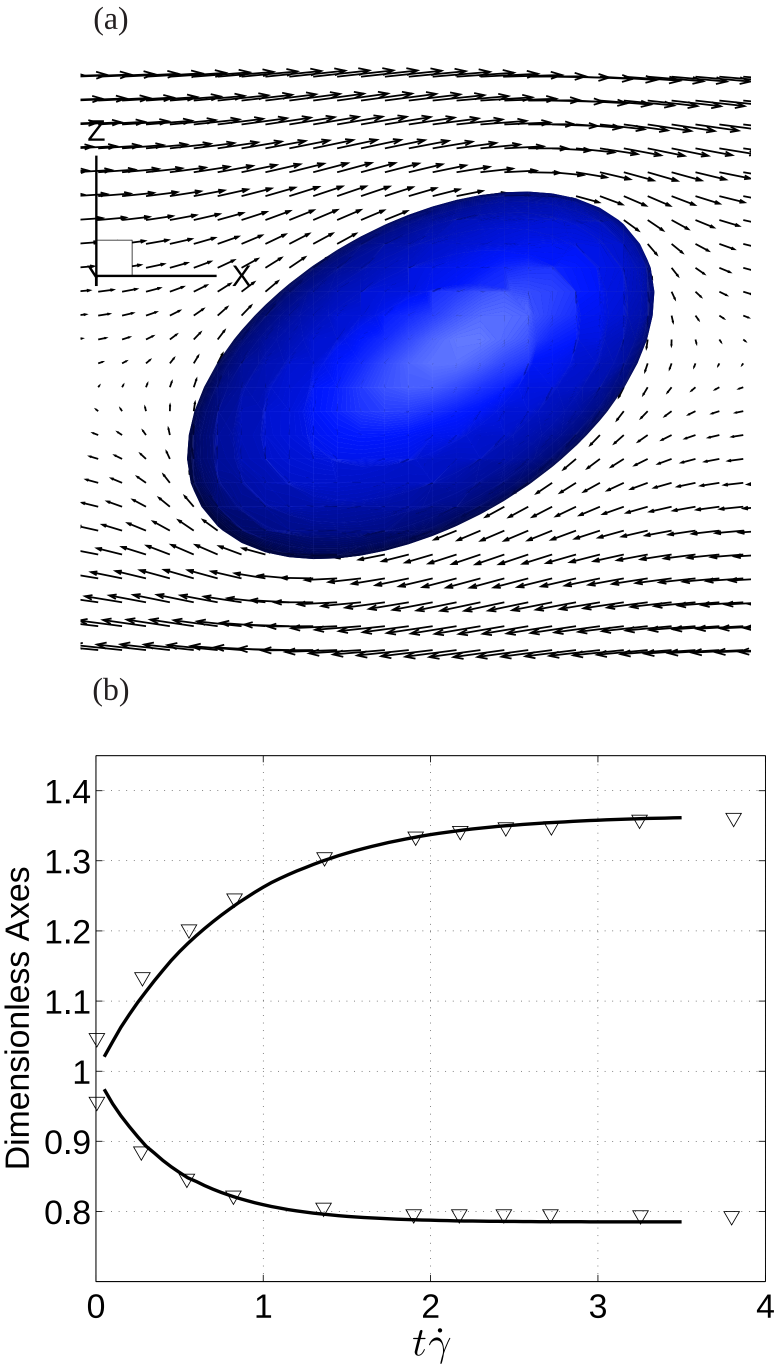

Figure 5.3: See next page for the caption.

(c)

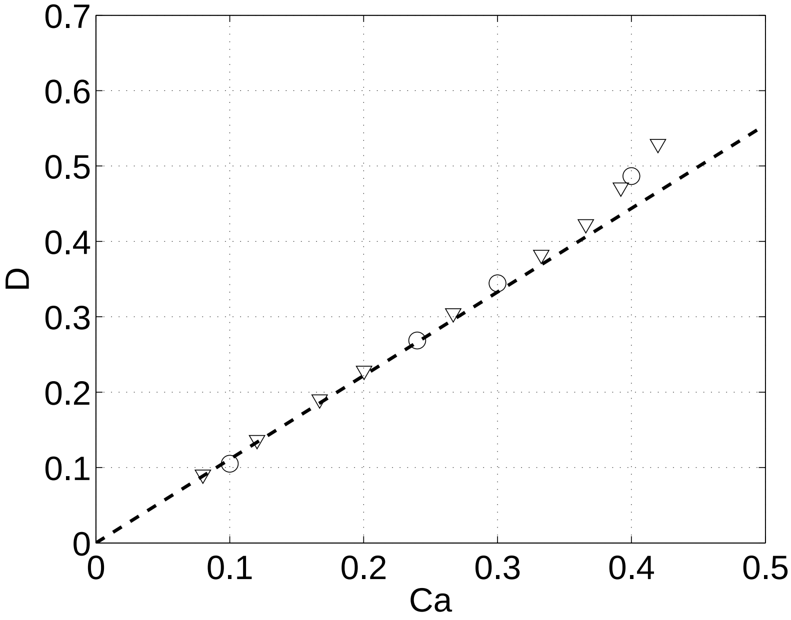

Figure 5.3: (a) An initially spherical drop in a linear shear flow with $Ca = 0.24$ and $\lambda = 1.4$, where the velocity field in the symmetry plane is shown for the steady state. (b) Evolution of the axes of the drop with $Ca = 0.24$ and $\lambda = 1.4$, where the upper branch is L/R_0 and the lower branch is B/R_0. Lines: current result; triangles: experimental data [99]. (c) D as a function of Ca at the steady state for $\lambda = 1.4$. Dashed line: Taylor's prediction [100, 101]; circles: present simulation; triangles: experimental data [99].

$\Delta t\dot{\gamma} = 0.005$.

Fig. 5.3(b) shows evolution of the principal and minor axes, normalized by R_0, against the dimensionless time, $t\dot{\gamma}$, at $Ca = 0.24$ and $\lambda = 1.4$. Together shown is the experimental result from Guido [99], who used an oil droplet in his study and employed an automated procedure to analyze image and extract the drop dimensions. It can be seen that the experimental data and present result agree very well and the present simulation is able to capture both the transient and steady deformations of the drop. Fig. 5.3(c) is a comparison among the theoretical, experimental, and current numerical results. In this figure, simulations are run at the capillary number $Ca = 0.1$ to 0.4 and $\lambda = 1.4$. The shape parameter D is calculated from the steady state and is compared with Taylor's prediction, Eq. (5.2), and also with Guido's experimental data [99]. The figure shows that at small capillary numbers, both experimental and numerical data fit the linear trend described by Eq. (5.2) very well. However, the deviation from the theory becomes evident as Ca is raised above 0.3. In all cases, the current result matches the experimental data very well.

5.2.3 Instability of a core-annular flow

In the third problem, a core-annular flow is considered as shown in Fig. 5.4(a), where two fluids are concentrically placed and have equal densities. The stationary flow in the cylindrical channel is perturbed initially by positioning the two-fluid interface as described by

$$r(x, t = 0) = a + \epsilon \, b \cos(kx), \tag{5.3}$$

where b represents the channel radius, $a = 0.5b$ is the mean thickness of the core fluid, $k = 2\pi/L$ denotes the wavenumber, the wavelength of the interfacial wave is $L/b = 6$, and ϵ is the dimensionless amplitude of the initial disturbance and is set to be $\epsilon = 0.01$. A 3D numerical simulation on a single-block Cartesian grid is performed even through the problem is axisymmetric, and we compare the result with that from the axisymmetric simulation in Blyth *et al.* [31].

In the current simulation, the cylindrical wall is represented by a triangular mesh and is immersed in a uniform Cartesian grid with resolution of $96 \times 48 \times 48$ in the x, y, and z directions. The time step size is $\Delta t = 0.005\mu_2 b/\sigma$. Periodic conditions are applied along the x-direction. The viscosity ratio and the Reynolds number are chosen to be $\lambda = \mu_2/\mu_1 = 0.5$ and $Re = \frac{\rho\sigma b}{\mu_2^2} = 1$. Fig. 5.4(b) shows a comparison between the current result and that in Blyth *et al.* [31]. The interface amplitude a_1 normalized by the initial amplitude $a_0 = \epsilon b$ is plotted against the dimensionless time $t\sigma/(\mu_2 b)$ on a log-linear scale. It can be seen that the two results agree with each other very well.

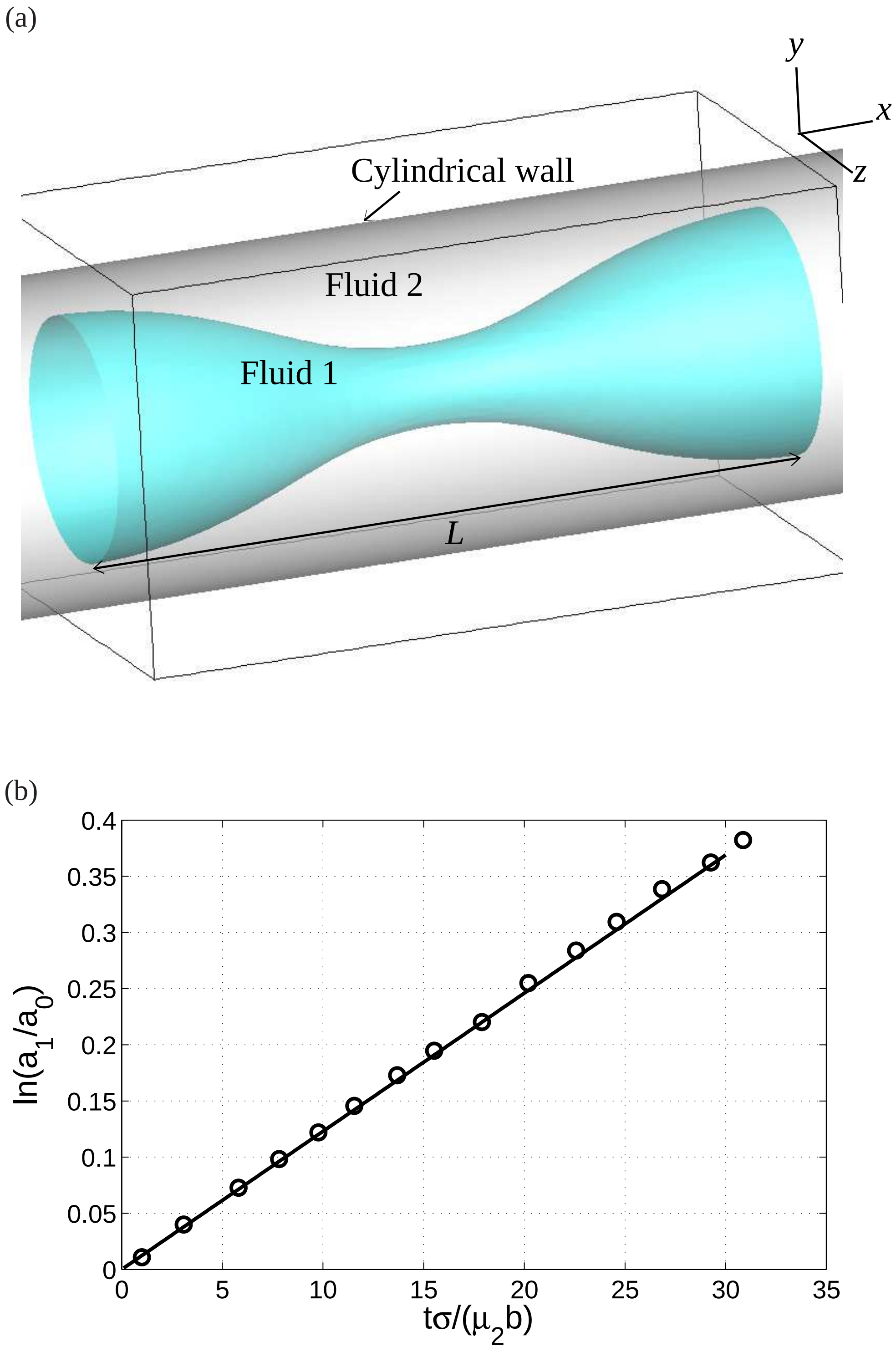

Figure 5.4: (a) Breakup of a core-annular flow. (b) Growth of the interface amplitude in time, where the line represents the current result and the symbols are from Blyth *et al.* [31].

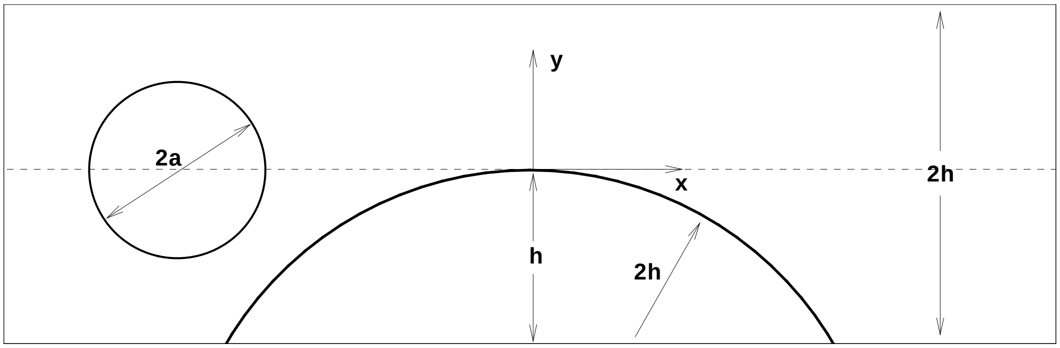

Figure 5.5: A 2D schematic of a drop passing through an asymmetric channel with a bump as labeled type A.

5.3 Motion of a drop through a constricted channel

5.3.1 Problem description

In this section, we apply the immersed-boundary method to simulate the motion of a viscous drop through an asymmetrically constricted channel. The problem is illustrated in Fig. 5.5, where the channel is assumed to be periodic with the ratio between the wavelength and the width at $L/(2h) = 3$. The flow is driven by a mean pressure gradient applied along the channel. A circular bump of radius $2h$ is set up in the channel blocking half of the passage. An initially spherical drop of radius a, where $a/h = 0.5$, is placed at the centerline as shown. The ratio between the viscosity of the drop, μ_d, and viscosity of the surrounding liquid, μ_0, is $\lambda = \mu_d/\mu_0$. The two fluids are assumed to have the same density, ρ. The Reynolds number and capillary number are defined respectively as $Re = \rho U_0(2h)/\mu_0$ and $Ca = \mu_0 U_0/\sigma$, where U_0 is a reference velocity, $U_0 = \chi h^2/(2\mu_0)$, and χ is the negative of the uniform streamwise pressure gradient driving the flow. In the current work, we will discuss the effects of λ, Ca, and Re on the translation and deformation of the drop. In addition, we will discuss the effect of the geometry of the bump and the three-dimensional effect.

In the simulations, a period of the channel is discretized by a uniform Cartesian grid which covers the semi-circular blockage. The uneven channel wall and the drop surface are treated respectively with the sharp- and diffuse-interface immersed-boundary methods as discussed in Chapter 2. The resolution of the volume mesh is chosen as $h/64$ in both x- and y-directions and the time step is $\Delta t U_0/h = 0.0005$, which prevents numerical instability while solving the Navier–Stokes equation and the level-set function.

5.3.2 Effects of the viscosity ratio and capillary number

We first consider the low-Re situation and study the consequence of varying the viscosity ratio and the capillary number. A set of simulations are performed at $Re = 1$, $Ca = 0.2$, 0.5, 1.0, and $\lambda = 0.01$, 0.1, 1.0, 10. When the drop motion settles down to a periodical state in the channel, usually after 3 to 5 cycles, we compare the drop's translational velocity and deformed shape under different values of λ.

Fig. 5.6 shows the x-velocity of the mass center of the drop, U_c, normalized by U_m against the position of the mass center, x_c/h. Here U_m is the maximum x-velocity of the flow *in the absence* of the drop and is obtained in a separate simulation. It can be seen from the figure that the translational velocity of the drop is significantly affected by λ and Ca. In Fig. 5.6(a) where $Ca = 0.2$, all the normalized velocities are less than 1, which means the drop in the gap moves at a slower velocity than the unperturbed background flow or introducing the drop slows down the flow through the channel. Furthermore, the velocity of the drop decreases as λ is increased, which is due to the greater impedance effect of a more viscous drop. For the drop with lower viscosity than the surrounding fluid, i.e., $\lambda = 0.01$ and 0.1, U_c/U_m is still less than 1. This is because the surface tension tends to maintain the drop's spherical shape and thus causes resistance to the flow. Nevertheless, the impedance of the drop should be lower than that of a rigid particle of equivalent size because the fluid inside the drop may move along with the surrounding fluid. The effect of the viscosity ratio on the translation of the drop seen here is consistent to the previous study of the drop moving in a symmetric plane channel [103] where the Stokes flow was considered.

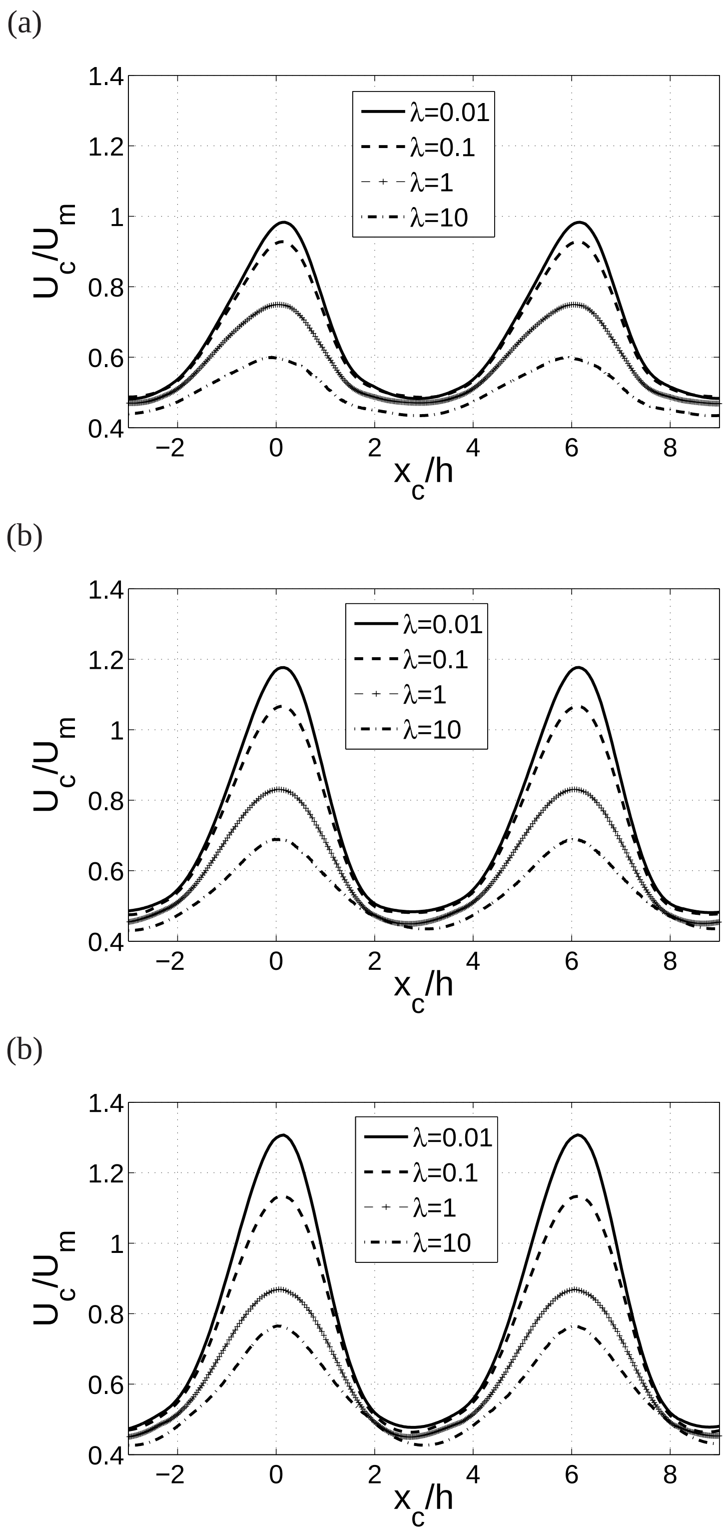

Figure 5.6: (a) The translational velocity of the mass center of the drop in the channel with bump A for *Re* = 1 and *Ca* = 0.2 (a), 0.5 (b), 1 (c).

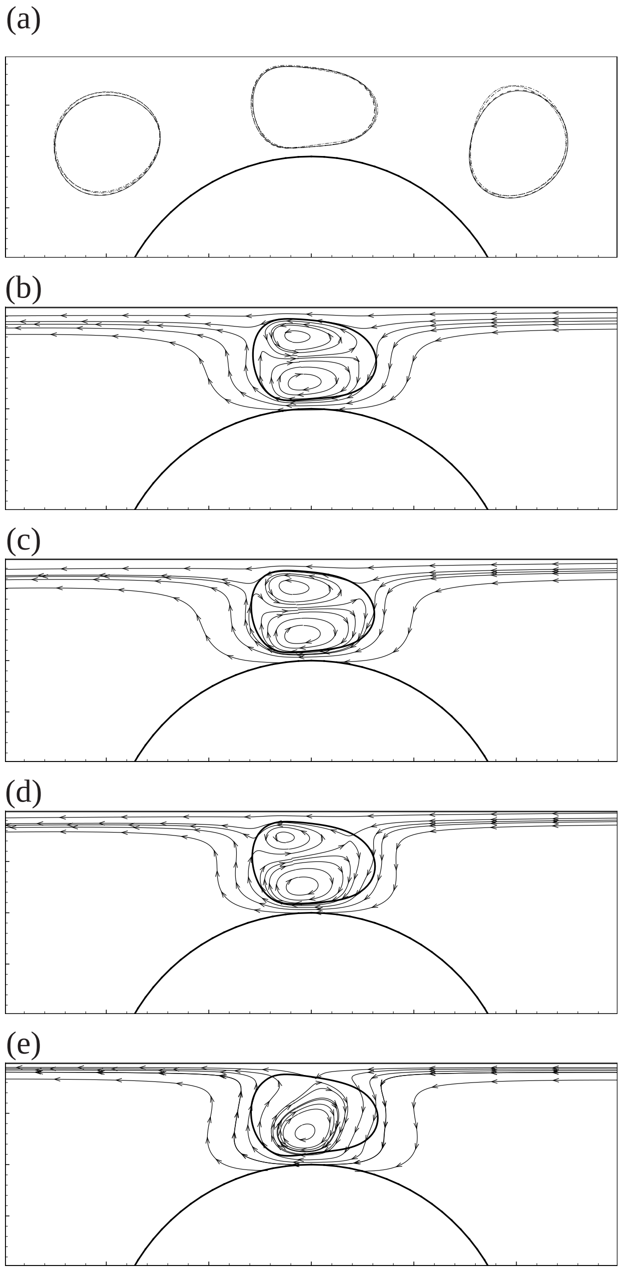

Figure 5.7: (a) The shape of the drop at three different positions in the channel: $x_c = -2h, 0, +2h$, for $Re = 1$ and $Ca = 0.2$, $\lambda = 0.01$ (solid line), 0.1 (dashed line), 1 (dash-double-dotted line) and 10 (dash-dotted line). (b-e) Streamlines as viewed by traveling with the drop for $\lambda = 0.01$ (b), 0.1 (c), 1 (d), 10 (e).

If we increase Ca and meanwhile have Re and λ fixed, the surface tension effect is reduced and the drop would thus deform more easily. Such deformability should play a positive role in enhancing mobility of the drop through the constricted channel. This effect is reflected in Fig. 5.6(b,c) where $Ca = 0.5$ and 1. Comparing these cases with the corresponding value of λ at $Ca = 0.2$, we see that the drop of higher capillary numbers passes through the channel gap at a faster speed. At $Ca = 0.5$, the maximum translational velocity of the drop reaches $U_c/U_m = 1.18$ for $\lambda = 0.01$ and 1.07 for $\lambda = 0.1$. At $Ca = 1$, this velocity reaches $U_c/U_m = 1.31$ for $\lambda = 0.01$ and 1.13 for $\lambda = 0.1$. Therefore, the translation of the drop is faster than the unperturbed flow. Of course in these cases where $\lambda < 1$, the low viscosity of the enclosed fluid inside the drop also contributes the mobility of the drop. In Fig. 5.6(b,c), U_c/U_m is still less than 1 for the cases of $\lambda = 1$ and 10.

The instantaneous deformation of the drop is shown in Fig. 5.7(a) for three locations: before, within, and after the gap region. In these cases, since the surface tension effect is relatively strong, the deformation of the drop is moderate, and the shapes of the drop at different values of λ are quite close to each other. However, since the drop has different viscosities in these cases, the fluid motion inside the drop exhibits disparate behaviors. Fig. 5.7(b) to (e) show the flow pattern as seen by moving along with the drop. That is, the streamlines are drawn from the the velocity field subtracted uniformly by the velocity of the drop, U_c. For the drop with a low viscosity, i.e., $\lambda = 0.01$ and 0.1, there are a pair of circulation regions inside the drop, meaning that the fluid on the top and bottom sides of the drop moves more slowly than the center. As the viscosity ratio is increased to $\lambda = 1$, the two vortices become more asymmetric and the one near the bump is larger in size than the other one. As the viscosity of the drop is further increased to 10 times of that of the surrounding fluid, i.e., $\lambda = 10$, the drop contains only one single vortex that allows the drop to roll clockwisely while it is passing through the gap region. This result confirms the explanation of the mixing experiment in Liau *et al.* [93] that a higher viscosity ratio would lead to a single-vortex pattern in the drop that passes

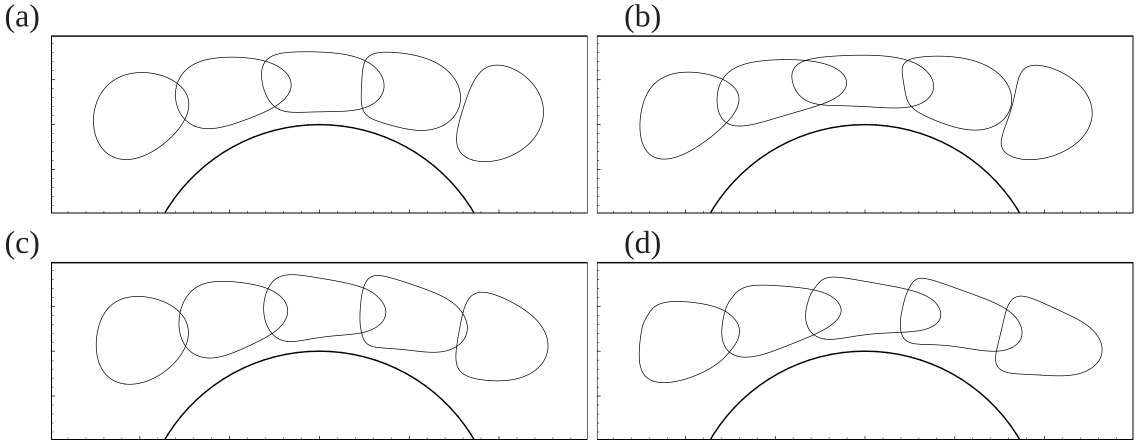

Figure 5.8: The instantaneous deformation of the drop at *Re*=1 and (a) $Ca = 0.5$, $\lambda = 0.1$, (b) $Ca = 1$, $\lambda = 0.1$, (c) $Ca = 0.5$, $\lambda = 10$, (d) $Ca = 1$, $\lambda = 10$.

over the bump.

The instantaneous deformation of the drop of higher capillary numbers is shown in Fig. 5.8 for $\lambda = 0.1$ and 10. The deformation patterns at $\lambda = 0.01$ and 1 are close to the situation at $\lambda = 0.1$ and are thus not shown here. From these plots, we see that as λ is fixed, increasing Ca leads to an elongated shape of the drop due to the weakened surface tension effect. As the drop becomes more viscous, e.g., $\lambda = 10$, its front portion becomes narrower compared to its rear portion, revealing the sluggish deformation of the drop due to its internal damping. Fig. 5.9 shows the streamline pattern inside the drop for $\lambda = 0.1$ and $Ca = 0.5$, 1, and 10. It can be seen that as Ca is increased, the drop becomes slenderer and the interior vortex pair are more skewed. At the highest Ca, the interior fluid joins the exterior fluid and forms a single circulation. From these results, we see that the single-vortex pattern can also be produced by increasing the capillary number.

5.3.3 Effect of the Reynolds number

In addition to the viscosity ratio and capillary number, we have varied the Reynolds number from 1 to 50 to study the effect of the fluid inertia. The simulations show

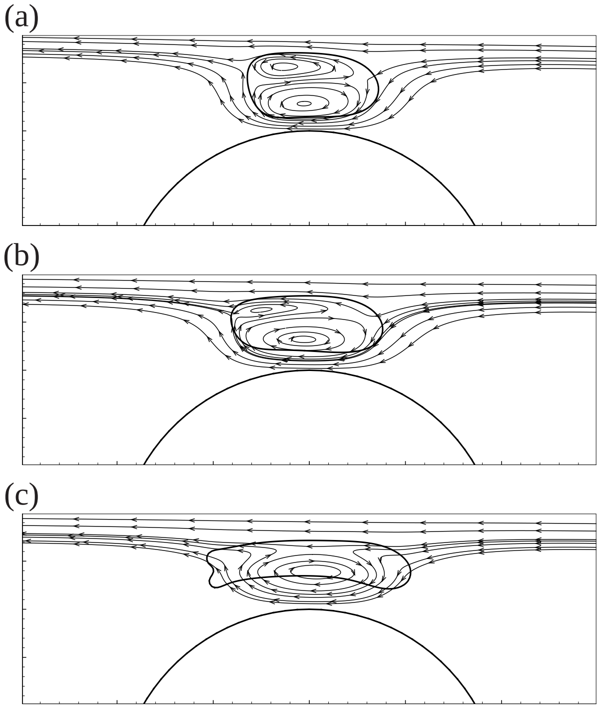

Figure 5.9: The instantaneous streamline pattern inside the drop at Re=1, λ = 0.1, and (a) Ca = 0.5, (b) Ca = 1, (c) Ca = 10.

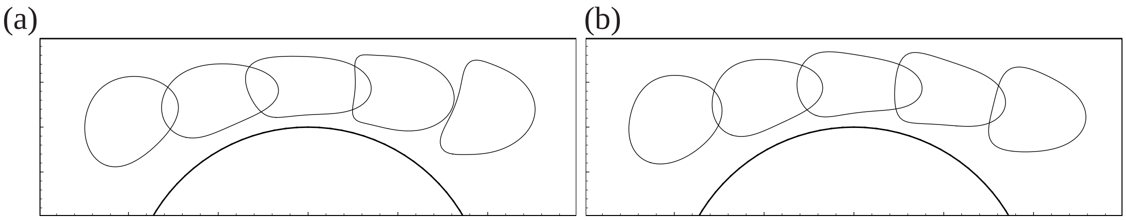

Figure 5.10: Deformation of the 2D drop at Re = 50, Ca = 0.5, and λ = 0.1 (a) and 10 (b).

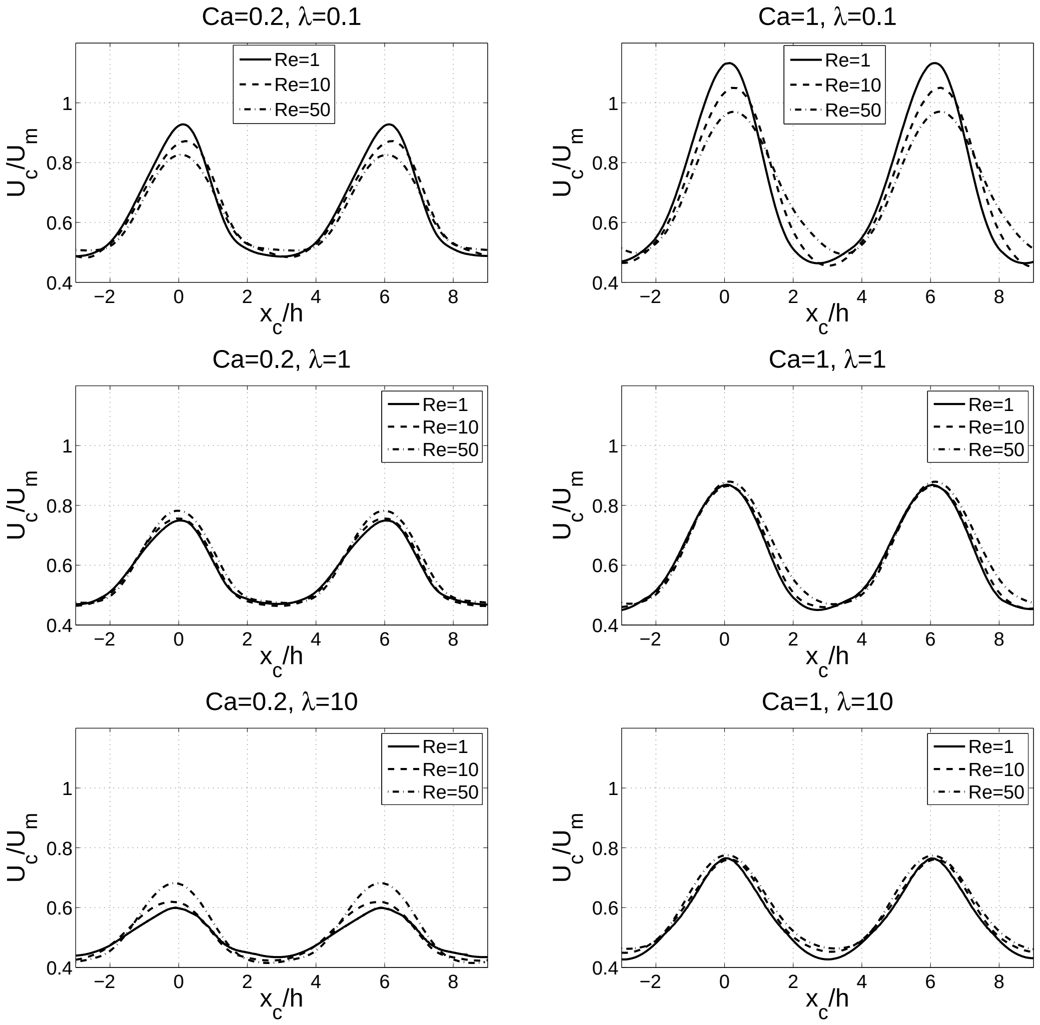

Figure 5.11: The translational velocity of the drop as a function of the centroid position for different *Re*, *Ca*, and λ.

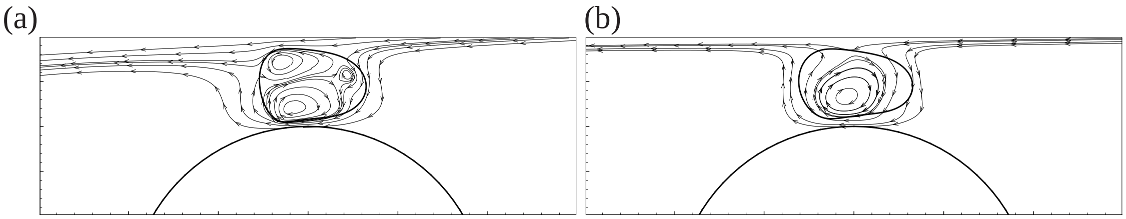

Figure 5.12: Instantaneous streamline pattern inside the drop where $Re = 50$, $Ca = 0.2$, $\lambda = 0.1$ (a) and 10 (b).

that the Reynolds number in this range does not change the deformation of the drop significantly. For example, Fig. 5.10 shows a sequence of drop shapes for $Ca = 0.5$, $Re = 50$, and $\lambda = 0.1$ or 10. Comparing these patterns with those corresponding cases for $Re = 1$ in Fig. 5.8(a,c), we only notice slight differences in the instantaneous shape as the drop exits the gap region.

Fig. 5.11 shows the translational velocity of the drop as a function of the position of the mass center for $Re = 1$, 10, and 50. The viscosity ratio is chosen to be $\lambda = 0.1$, 1, or 10, and the capillary number is $Ca = 0.2$ or 1. One interesting observation from this figure is that the effect of Re is not consistent in these cases. At the lowest viscosity ratio, $\lambda = 0.1$, U_c/U_m is greater for lower values of Re. Note that the reference velocity used in the normalization, U_m, varies for different Reynolds numbers and the result does not mean that the actual velocity of the drop would decrease when Re is increased. Instead, it means that introducing the drop into the channel causes relatively more impedance to the flow when Re is higher. The figure shows that the effect of Re is not very significant at $\lambda = 1$, or at $\lambda = 10$ and $Ca = 1$. However, at $Ca = 0.2$ and $\lambda = 10$ the role of Re is reversed. In this case, U_c/U_m is greater for higher values of Re, meaning that introducing the viscous drop into the channel would cause less flow resistance.

To better understand the effect of the Reynolds number, we plot in Fig. 5.12 the streamline pattern as the drop passes through the gap. Again, the streamlines are plotted in the coordinate system that moves in the x-direction with the centroid of the drop. The two cases with $Ca = 0.2$, $Re = 50$, and $\lambda = 0.1$ or 10 are shown. The corresponding cases with $Re = 1$ can be found in Fig. 5.7(c,e).

Comparing Fig. 5.12(a) and Fig. 5.7(c), where both Ca and λ are the same but Re is different, we notice that the fluid motion inside the drop becomes somewhat more complex in the case of $Re = 50$. Note that a higher Re corresponds to the situation where the fluid density is increased while all other dimensional parameters are held constant. For $Re = 1$, the flow inside the drop consists a pair of major vortices, while at $Re = 50$, smaller vortices have been developed due to the low-viscosity and high-inertia effects inside the drop. Since the drop fluid is 10 times less viscous than the surrounding fluid in this case, the interior flow in the case of $Re = 50$ becomes less regular and thus the drop causes higher resistance to the flow than in the corresponding case of $Re = 1$. On the other hand, when the viscosity ratio is at $\lambda = 10$, the flow inside the drop consists of only one clockwise vortex for both $Re = 1$ and $Re = 50$, as seen in Fig. 5.7(e) and Fig. 5.12(b). At this high viscosity ratio, the shear layers in the surrounding fluid becomes more important for the mobility of the drop. A higher Re in this case likely provides better lubrication for the drop to go through the gap, and therefore the impedance effect of the drop on the flow is less than that at $Re = 1$. From this study we see that increasing Re up to 50 may affect the mobility of the drop but the the flow pattern inside the drop does not change significantly unless λ is much lower than 1.

5.3.4 Effect of the channel geometry

The flow patterns observed in Section 5.3.(2) and 5.3.(3) clearly have to do with the asymmetric shape of the channel. To better understand the geometric effect on the drop dynamics, we introduce two other bumps as shown in Fig. 5.13(a), where one has an exactly semi-circular shape and the other is a triangle. The channel length is kept the same in all three cases. The three types of bumps are labeled with A, B, and C, respectively. They have the same height but different gradualness in the gap width transition. Among the three cases, the triangular shape of bump C would cause the greatest curvature to the streamlines of the background flow. The maximum x-velocity in the absence of the drop for bump A, B, and C is U_m/U_0=0.56, 0.66, and 0.82, respectively. Fig. 5.13(b) shows that the shape of the gap has a significant effect on the motion of the drop. The width of the velocity peak of the drop is the greatest for bump A but the narrowest for bump C, reflecting the quick transition of the drop through the gap in case C. The figure also shows that the normalized peak velocity of

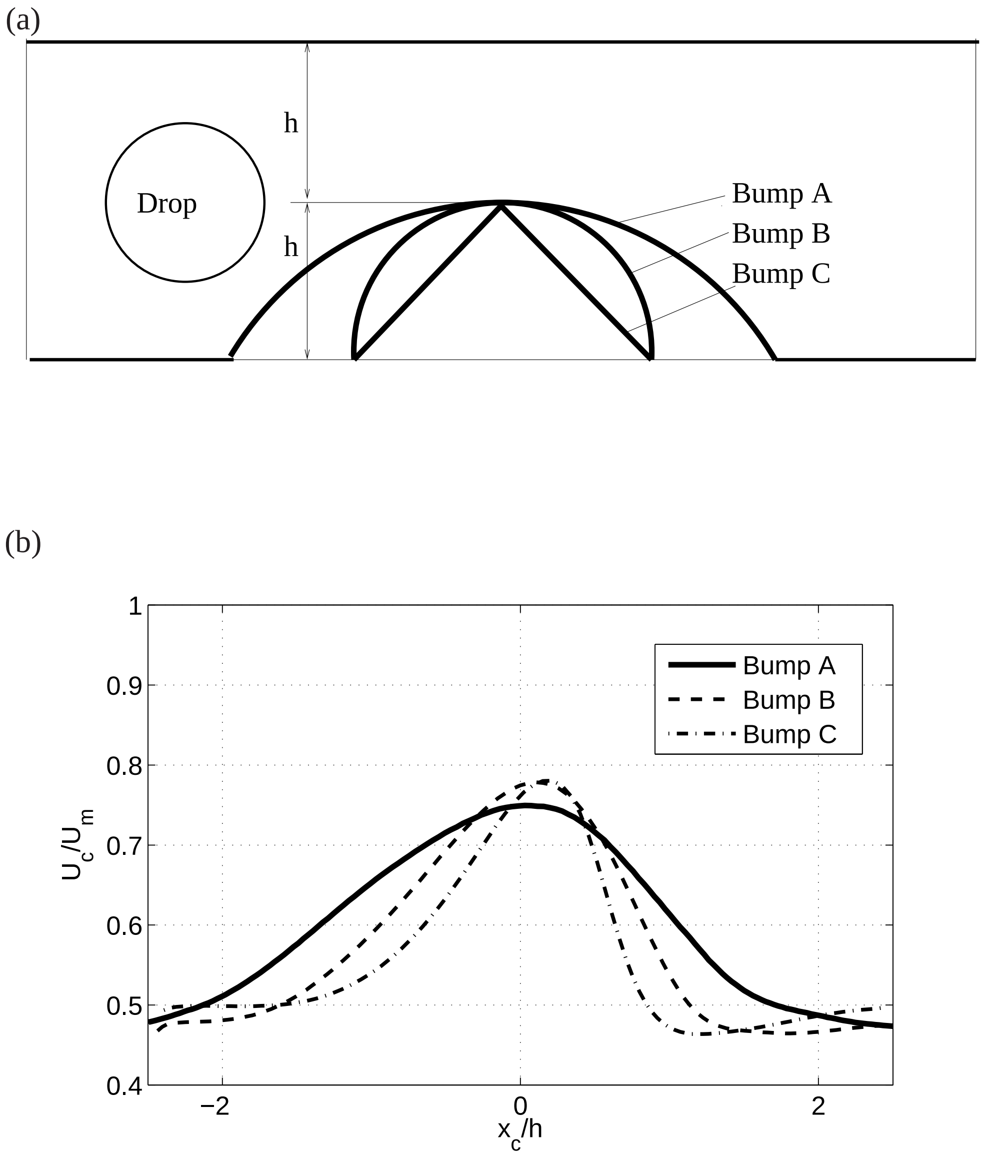

Figure 5.13: (a) Three types of bumps considered here to study the geometric effect. (b) The velocity of the mass center of the drop through each type of channel.

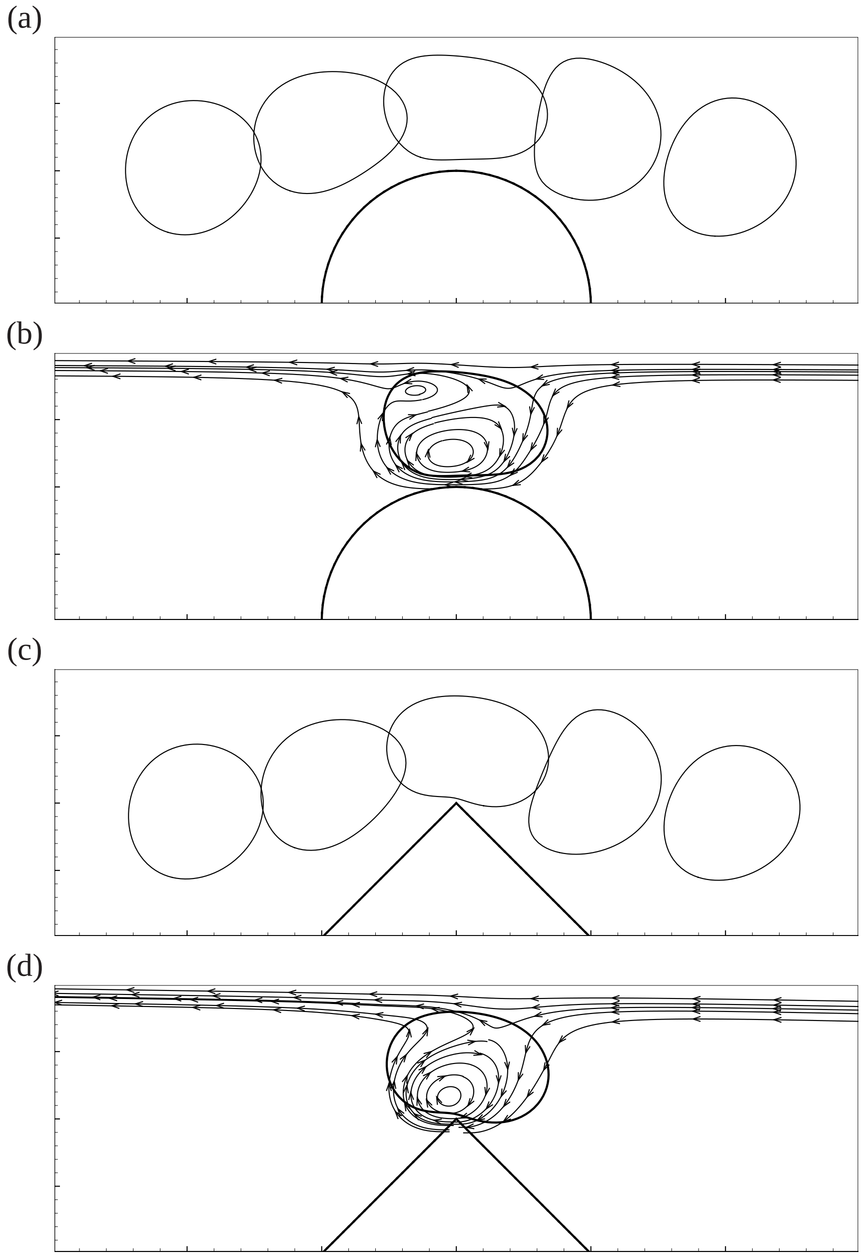

Figure 5.14: Drop deformation and the streamline pattern for bump B (a,c) and bump C (b,d) at $Re = 1$, $Ca = 0.2$, and $\lambda = 1$. The corresponding result for bump A is in Fig. 5.7(a,d).

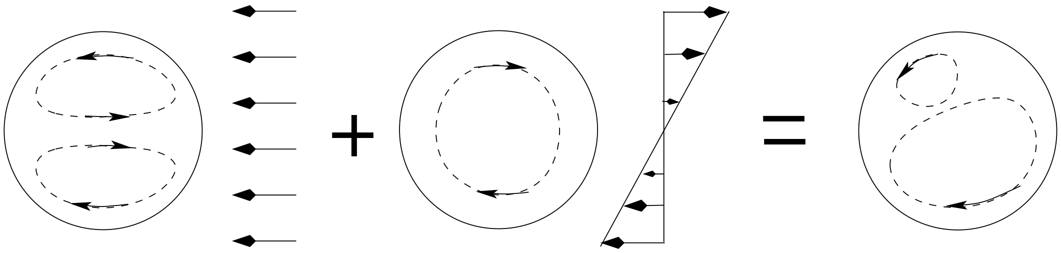

Figure 5.15: Illustration of the superposition effect of the uniform and shear flows causing the circulations inside the drop that passes over the bump.

the drop is similar for bumps B and C while this velocity is slightly lower for bump A.

Fig. 5.14 shows the simulation results for bump B and bump C at $Re = 1$, $Ca = 0.2$ and $\lambda = 1$. The corresponding result for bump A is in Fig. 5.7(a,d). Comparing the drop shapes in the three cases, we see that bump C causes the most asymmetric deformation to the drop. The asymmetry in the internal flow is shown by the streamline pattern. It can be seen that the two circulations zones in the drop becomes more asymmetric for bump B as compared to those for bump A in Fig. 5.7(d). For bump C, the interior of the drop forms a single circulation zone, which is similar to the situation in the case of bump A with $\lambda = 10$ shown in Fig. 5.7(e). Therefore, for bump C the critical viscosity ratio λ becomes much lower for a single circulation to occur inside the drop.

To characterize the flow pattern inside a drop passing through a winding channel, Stone & Stone [92] approximated the flow by simple superposition of uniform and shear flows. Their approach can be used in the current study to qualitatively explain the streamline pattern observed here. The idea is illustrated in Fig. 5.15. As the drop is going through the gap, the shearing effect of the channel walls both above and below the drop, if symmetric, would cause a pair of equal circulation zones inside the drop, much like a uniform flow passing the drop. In the present case, the bump on the bottom side causes greater shear than the straight wall on the top side. Therefore, a linear shear flow can be used to approximate the asymmetric shearing effect, which would cause a single circulation zone in the drop. The resultant flow depends on how strong the shear flow is relative to the uniform flow. In the present case, increasing either the viscosity ratio or the curvature of the bump would strengthen the shear flow effect and cause the circulations to be more skewed. Different from the inverted U-channel in Stone & Stone [92] where the shear flow is in the counterclockwise direction due to the curvature of the entire channel, in the present case the shear flow is in the clockwise direction.

5.3.5 Three-dimensional effect

We now extend the study of the drop to 3D and incorporate the deformation of the drop in the spanwise direction. To do this, the channel is extended in the z-direction and the spanwise depth of the channel is $2h$. Periodic boundary condition is applied along the z-axis. To limit the scope of our study, we only focus on the cases where $Re = 1$. Our simulation shows that in the 3D cases considered here, the translational velocity of the drop is generally higher as compared to that of the corresponding 2D drop, which is due to the lower drag induced by the 3D drop. This result is consistent to the finding in Mortazavi & Tryggvason [104], who studied the translation of 2D and 3D drops in a plane channel at $Ca = 0.05$.

Fig. 5.16 shows the deformation pattern of the 3D drop for bump A with $\lambda = 1$ and $Ca = 0.2$ or 1. Both side view and top view of the drop are shown. From the side view, it can be seen that the drop's shape is very similar to that in the corresponding 2D case with the same viscosity ratio and capillary number, i.e., Fig. 5.16(a) and Fig. 5.7(a). The spanwise deformation, which is unique in the 3D cases, can be clearly seen from the top view in Fig. 5.16(b,d). For $Ca = 0.2$, the 3D drop overall remains a circular shape in the xz-plane. In the case of $Ca = 1$, as the drop exits the gap, its rear portion is depressed in the middle but is stretched at upper and lower corners, forming two protrusions on the rear side. In all the 3D cases, the drop exhibits a symmetric deformation pattern about the $z = 0$ plane.

Fig. 5.17(a-c) shows the streamline pattern inside the drop for the case of bump A and $Ca = 0.2$, $\lambda = 0.1$, 1, and 10. By comparing the flow field with that in the

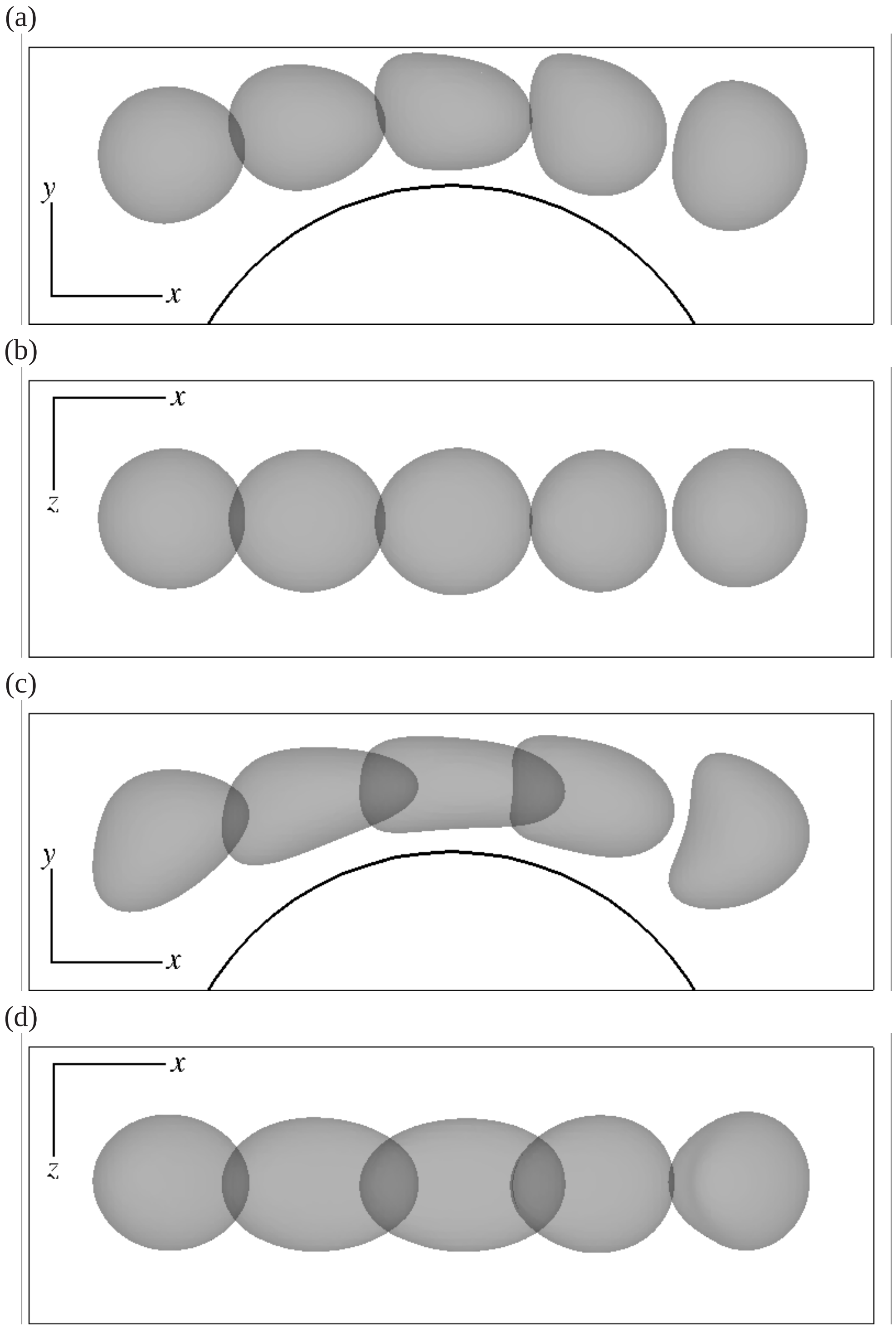

Figure 5.16: Side view (a,c) and top view (b,d) of the 3D drop above bump A for $Re = 1$, $\lambda = 1$, and (a,b) $Ca = 0.2$, (c,d) $Ca = 1$.

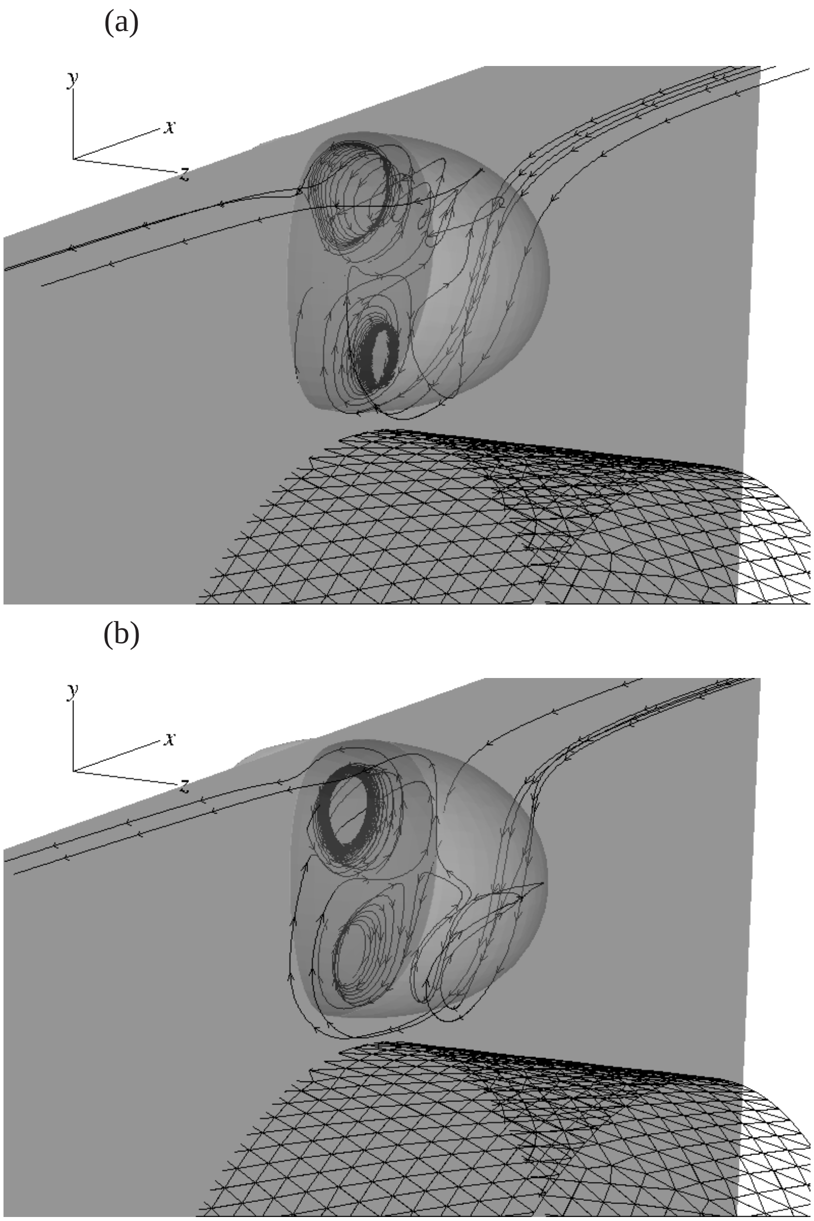

Figure 5.17: See next page for the caption.

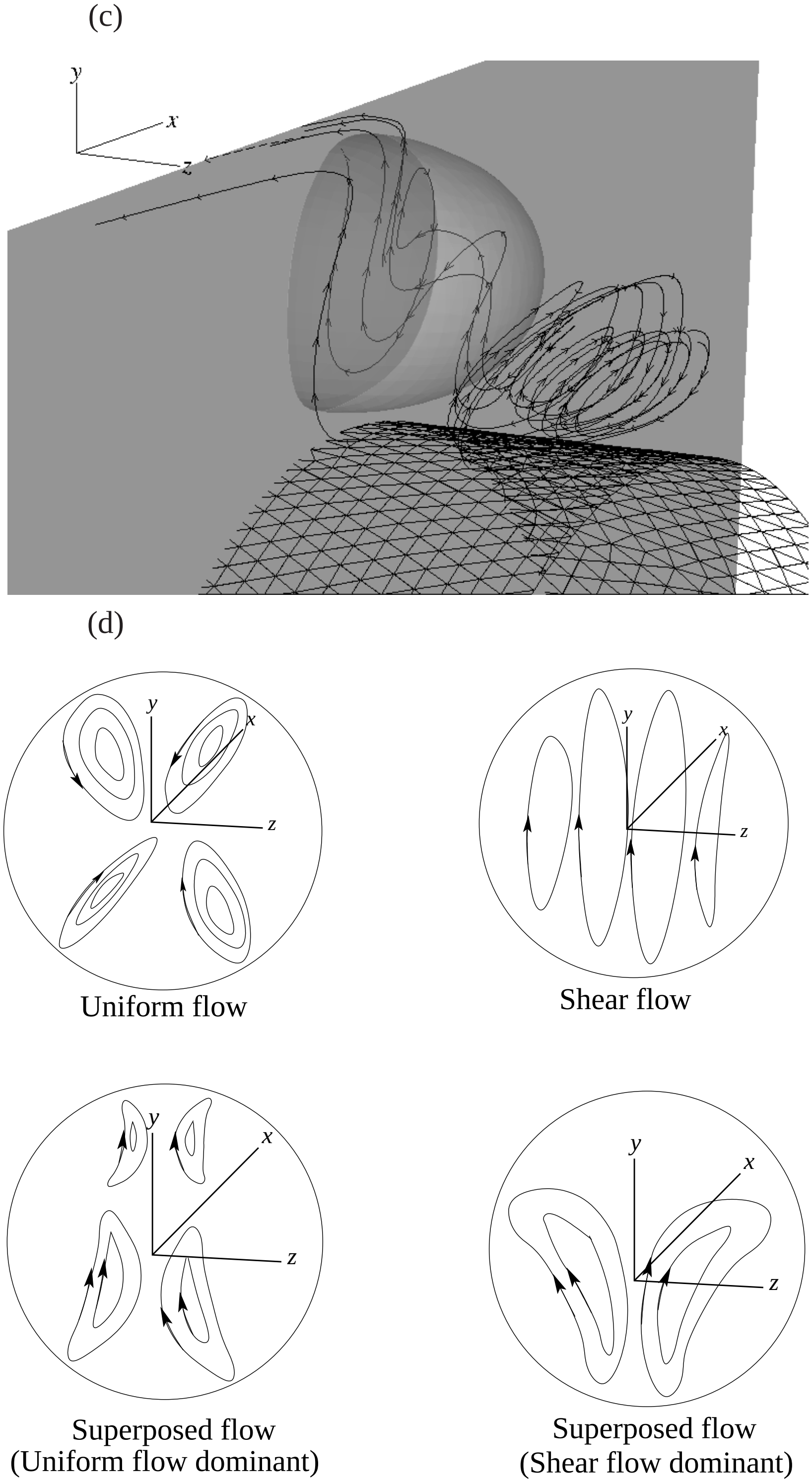

Uniform flow

Shear flow

Superposed flow
(Uniform flow dominant)

Superposed flow
(Shear flow dominant)

Figure 5.17: The streamline pattern inside the drop above bump A with $Re = 1$, $Ca = 0.2$, and $\lambda = 0.1$ (a), 1 (b), and 10 (c). (d) Illustration of the superposition effect for the streamlines off the symmetry plane.

corresponding 2D case shown in Fig. 5.7(c-e), we note that the circulation in the symmetry plane at $z = 0$ is close to that in the 2D case. Away from this symmetry plane, 3D features can be clearly seen in the present cases. To explain the these features, we again use the similar decomposition approach described in Stone & Stone [92]. In the approach, the interior of a spherical drop passing a channel turn consists of the axisymmetric circulations caused by a uniform flow and the in-plane circulation caused by a shear flow. A similar decomposition can be applied here although in the current case there is no spanwise wall present and the circulation in the *xz*-plane is not as strong as that in the *xy*-plane. As seen in Fig. 5.17(d), if the uniform flow is dominant, the circulations off the symmetry plane ($z = 0$) become bent in the spanwise direction, and those circulations in the lower hemisphere become greater in size. Such situation is found in Fig. 5.17(a) where $\lambda = 0.1$. If the shear flow becomes strong or even dominant, the circulations off the symmetry plane change their topology – the circulations in the upper hemisphere disappear while those in the lower hemisphere take over and are bent in the spanwise direction. Such situations are found in the cases of $\lambda = 1$ and $\lambda = 10$.

As discussed in the 2D case, the shear flow here is in the clockwise direction as viewed from the positive *z*-axis, which is opposite to that in the inverted U-channel studied by Stone & Stone [92]. In addition, Fig. 5.17(a-c) shows that the circulations are not separate vortex rings but are connected to each other, forming spiral patterns.

We have studied the 3D drop for $Ca = 1$. The results are in general consistent to that presented in Fig. 5.17. One major difference is that at $Ca = 1$, the drop becomes narrower in the spanwise direction and the horizontal circulations become weak or even disappear, so the circulations mostly remain in the *xy*-planes. We also studied the drop over bumps B and C. The results are again consistent except that the shear flow effect becomes dominant at a much lower value of the viscosity ratio, e.g., $\lambda = 1$, for those two bumps.

5.4 Conclusion

We have applied an immersed-boundary method to simulate the dynamics of a viscous drop passing through a channel with bumps on one side. The goal is to study the translation and deformation of the drop and to investigate the flow pattern inside the drop. The governing parameters under consideration include the Reynolds number, the capillary number, and the viscosity ratio.

The results show that the drop with a higher viscosity than the surrounding fluid or with high capillary numbers tends to impede the flow, while the drop with a lower viscosity may accelerate the flow. Although the deformation patterns of the drop at different viscosity ratios may be close to each other when the capillary number is low, the internal flow patterns can be quite different. At higher viscosity ratios, the vortex pair become skewed or reduce into one single vortex. This result is consistent to the experimental observation. A similar internal flow pattern may appear when the capillary number is raised and the drop has a slender shape. By varying the shape of the bump, we found that the critical viscosity ratio for the flow in the drop to switch the pattern becomes lower if the bump has a greater curvature. The flow pattern is in general consistent for a range of Reynolds numbers except at very low viscosity ratios, the interior of the drop may consists of multiple vortices due the inertial effect.

Three-dimensional simulations show that the flow pattern in the symmetry plane is close to that in the two-dimensional study. Off the symmetry plane the vortices also become skewed. Qualitatively the streamline pattern inside the drop may be viewed as a result of superposition of external uniform and shear flows. Finally, the switch of the internal flow pattern as the drop passes over the bump can be used to enhance the mixing inside the drop.

CHAPTER 6

CONCLUSIONS

6.1 Summary of the present work

We have developed an immersed-boundary method to model the fluid-structure interaction of viscous incompressible fluids with thin solid structures. The method was applied to simulate the aeroelasticity of flexible flapping wings and hydrodynamic interaction of multiple elastic sheets placed in tandem arrangement.

In Chapter 3, a two-dimensional hovering wing is modeled as a flexible plate undergoing translating and pitching motions. The wing is parametrized by the dimensionless mass ratio, which represents the relative effect of the wing inertia with respect to the aerodynamic force, and the frequency ratio, which represents the flexibility of the structure. The representative values of the mass ratio from the insect data were used, while the frequency ratio was systematically varied to represent from a completely rigid wing to a very flexible wing. The results show that for a certain range of flexibility, the wing deformation increases the lift production and enhances the aerodynamic power efficiency. However, when the wing is overly flexible, the deformation is detrimental to the aerodynamic performance. Furthermore, when the magnitude of deformation is about the same, the low-mass wing leads to greater performance compared to the high-mass wing. Note that for the low-mass wing, both aerodynamic force and the wing-inertial force have significant contribution to the wing deformation.

In Chapter 4, the energy-harvesting potential of an array of elastic sheets in tandem arrangement was explored where the sheets oscillate in a free stream due to vortex-induced vibration. The effects of the mass ratio and the separation distance are investigated. It was found that within a particular region that depends on the mass ratio, the two sheets in tandem experience greatly increased vibration, i.e., a state referred to as the system resonance. At the resonance, both the upstream and the downstream sheets undergo larger-amplitude oscillations, and their kinetic energy grow by several times as compared to the corresponding single sheet placed in the flow. We further studied the mechanism of the system resonance in detail and found that the resonance is caused by the vortex-sheet and vortex-vortex interactions that adjust the oscillation frequency and modify the magnitude/phase-shift of the hydrodynamic force on the sheets. We also discussed the effects of the Reynolds number and reduced velocity. Furthermore, implication of the study on multiple sheets in tandem arrangement is also discussed.

The immersed-boundary method is also extended to two-phase flows in arbitrary domains in which both fluid-solid and fluid-fluid interfaces of complex shapes need to be handled. Using the level-set function and the diffuse-interface approach to treat the fluid-fluid interface, the method has the flexibility of dealing with interfacial morphological and topological changes. Both two- and three-dimensional versions of the method are developed and are described in Chapter 2. The method was used to model the dynamics of drops traveling through microchannels with bumps on one side of the walls. The effects of the capillary number, viscosity ratio, and Reynolds number on the drop translation and deformation were investigated. The special focus was given to the interior flow pattern of the drop. It was found that when the viscosity ratio or the curvature of the bumps is increased, the vortex pair inside the drop become skewed or even reduce to one single circulation. In three dimensions, the circulations in the spanwise direction are also developed. These flow patterns could be used to enhance the drop based mixing.

6.2 Contributions

The contribution of this dissertation work can be summarized as follows.

1. We have developed a simple two-dimensional model to address the aeroelasticity

of insect wings and help to explain the role of the structural deformation in the aerodynamic performance of the wings. We have clarified the respective contributions from the wing inertia and the aerodynamic force to the wing deformation, and through the present study, we have made the aerodynamic consequence of each type of contribution understood. The results presented here will be useful for the future engineering design of flexible flapping wings.

2. We have innovatively applied the idea from the formation flight and fish schooling in nature to energy-harvesting piezo-leaves in close arrangement. We have developed a simple model to simulate the hydrodynamic interaction of two leaves in tandem arrangement and have found a resonant state at which both leaves can benefit remarkably from the hydrodynamic interaction. We have offered an explanation, through a detailed study, to the underlying mechanism for the observed resonant behavior.

3. We have successfully developed and validated a Cartesian grid based numerical method for two- and three-dimensional simulations of the two-phase flows in complex domains, and we have applied the method to simulate the drop dynamics in non-trivial shaped channels. We have systematically studied the flow pattern inside the drop, and the results help to explain the mechanism behind the observed drop behavior in a previous experimental study. Furthermore, the results will be useful for the design drop-based mixing in microfluidic channels.

The work described in this dissertation has been presented in the following publications:

1. **Yin, B.**, Luo, H. (2013) Numerical simulation of drops inside an asymmetric microchannel with protrusions. Submitted to Computers & Fluids.

2. **Yin, B.**, Luo, H. (2013) Hydrodynamic interaction of oblique sheets in tandem arrangement. Physics of Fluids, 25, 011902

3. Luo, H., Dai, H., Ferreira de Sousa, P.,**Yin, B.** (2012) On numerical oscillation of the direct-forcing immersed-boundary method for moving boundaries. Computers & Fluids. 56, 61-76

4. **Yin, B.**, Luo, H. (2010) Effect of wing inertia on hovering performance of flexible flapping wings. Physics of Fluids, 22, 111902 (10 pages).

5. **Yin, B.**, Luo, H. Energy-harvesting potential of multiple elastic structures in tandem arrangement. The 64th Annual Meeting of APS/DFD, November 20-22, 2011. Baltimore, Maryland.

6. **Yin, B.**, Luo, H. Numerical simulation of two-phase flows in complex geometries by combining two different immersed-boundary methods. *The 63rd APS/DFD Annual Meeting*, Nov. 21-23, 2010. Long Beach, California.

6.3 Future work

The future work is summarized as follows regarding each of the three applications:

For the inset flight problem, there are rarely three-dimensional models that address the role of the wing flexibility in the aerodynamics. The future work will focus on development of such models, which are obviously more computationally expensive. The questions that could be addressed include: (1) to what extent can the current 2D results be extended to 3D? (2) Can the complex structure of an insect wing be parametrized efficiently using only a few variables? (3) What fluid-structure interaction mechanisms have caused the 3D and asymmetric deformation patterns of insect wings observed during flight? (4) How general can the results from simplified numerical models be extended to different wing morphology of insects? (5) How can results be applied to actual wing designs of a biomimetic micro air vehicle? Some of these questions are currently being answered by our group, while others require future collaboration with biologists as well as engineers who specialize machine design and system integration.

For the energy harvesting problem, a straightforward question to ask is whether there is a resonance regime for multiple piezo-leaves placed in a patterned array. As suggested by our current study, an investigation incorporating more leaf sheets would help to find the answer in which the separation distance and array pattern could be explored. In addition, a simulation including the characteristics of the piezoelectric material and the circuit has not been done yet. Such system-level modeling work could be pursued in the future.

For the study on the drops moving in microchannels, the future study could focus on modeling the actual mixing inside the drop and quantifying the mixing rate for different geometries of the wall protrusions. Fig. 6.1 shows an example of such study, where mixing of two species inside the drop is shown for three bump shapes considered in the present work. Passive tracers are introduced inside the drop to mark the mixing both qualitatively and quantitatively. Our preliminary study confirms that the wall protrusions significantly enhance the mixing rate in the drop. Further quantitative and parametric study can be done in the future.

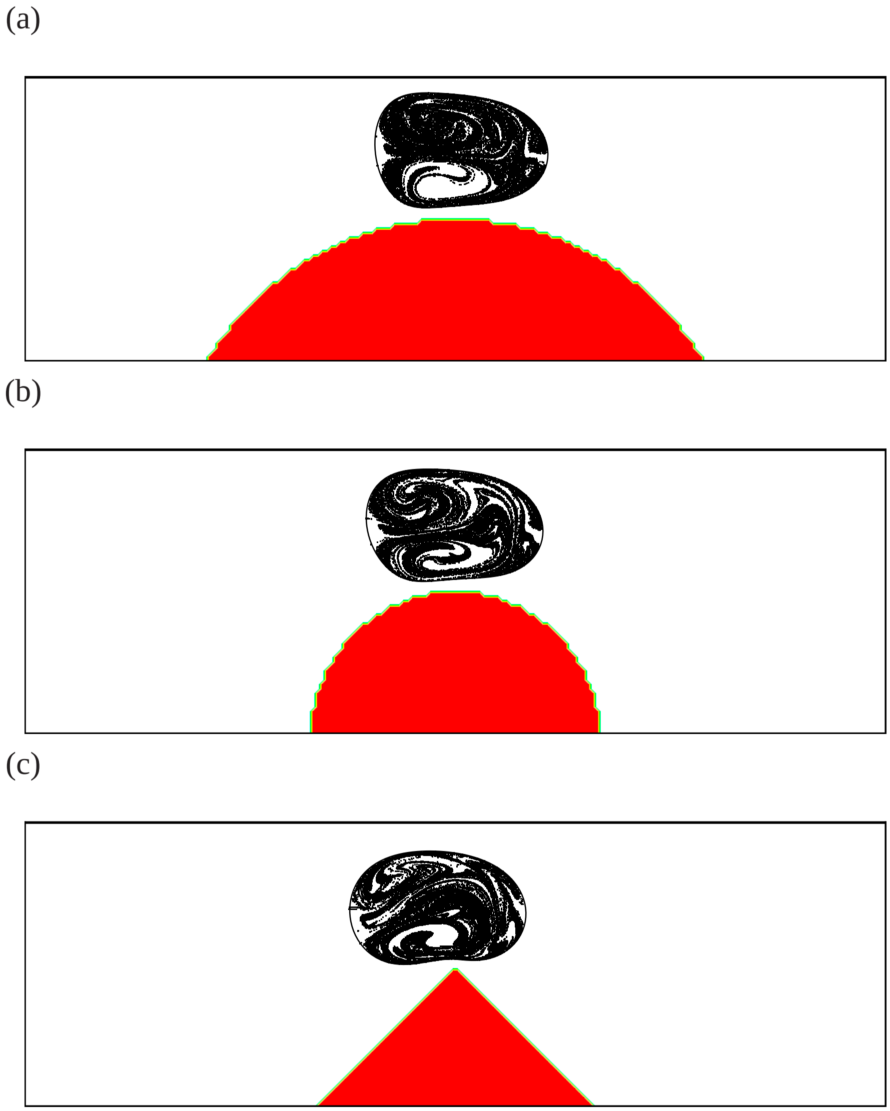

Figure 6.1: Mixing as indicated by passive tracers inside different channels with (a) bump A; (b) bump B; (c) bump C.

REFERENCES

[1] Z.J. Wang. Vortex shedding and frequency selection in flapping flight. *J. Fluid Mech.*, 410:323–341, 2000.

[2] M. Sfakiotakis, D.M. Lane, and J.B.C. Davies. Review of fish swimming modes for aquatic locomotion. *IEEE J. Oceanic. Eng.*, 24(2):237–252, 1999.

[3] J.M. Berg, J.L. Tymoczko, and L. Stryer. Biochemistry: International version (hardcover). 2002.

[4] P. Bagchi, P.C. Johnson, A.S. Popel, et al. Computational fluid dynamic simulation of aggregation of deformable cells in a shear flow. *J. Biomech. Eng.*, 127(7):1070, 2005.

[5] C.P. Ellington. The novel aerodynamics of insect flight: applications to micro-air vehicles. *J. Exp. Biol.*, 202(23):3439–3448, 1999.

[6] S.A. Combes and T.L. Daniel. Flexural stiffness in insect wings II. Spatial distribution and dynamic wing bending. *J. Exp. Biol.*, 206(17):2989–2997, 2003.

[7] R.J. Wootton, R.C. Herbert, P.G. Young, and K.E. Evans. Approaches to the structural modelling of insect wings. *Phil. Trans. R. Soc. Lond. B*, 358:1577–1588, 2003.

[8] H.A. Sodano, D.J. Inman, and G. Park. A review of power harvesting from vibration using piezoelectric materials. *Shock Vib.*, 36(3):197–206, 2004.

[9] S.R. Anton and H.A. Sodano. A review of power harvesting using piezoelectric materials (2003–2006). *Smart Mater. Struct.*, 16:R1–R21, 2007.

[10] H.D. Akaydin, N. Elvin, and Y. Andreopoulos. Energy harvesting from highly unsteady fluid flows using piezoelectric materials. *J. Intel. Mat. Syst. Str.*, 21(13):1263, 2010.

[11] S. Li, J. Yuan, and H. Lipson. Ambient wind energy harvesting using cross-flow fluttering. *J. Appl. Phys.*, 109(2):026104–026104, 2011.

[12] M.R. Bringer, C.J. Gerdts, H. Song, J.D. Tice, and R.F. Ismagilov. Microfluidic systems for chemical kinetics that rely on chaotic mixing in droplets. *Philosophical Transactions of the Royal Society of London. Series A: Mathematical, Physical and Engineering Sciences*, 362(1818):1087–1104, 2004.

[13] DD Joseph, R. Bai, KP Chen, and YY Renardy. Core-annular flows. *Ann. Rev. Fluid Mech.*, 29(1):65, 2003.

[14] J. Clausell-Tormos, D. Lieber, J.C. Baret, A. El-Harrak, O.J. Miller, L. Frenz, J. Blouwolff, K.J. Humphry, S. Koster, et al. Droplet-based microfluidic platforms for the encapsulation and screening of mammalian cells and multicellular organisms. *Chem. Biol.*, 15(5):427–437, 2008.

[15] V. Srinivasan, V.K. Pamula, and R.B. Fair. An integrated digital microfluidic lab-on-a-chip for clinical diagnostics on human physiological fluids. *Lab Chip*, 4(4):310–315, 2004.

[16] S. Ghosh, T.K. Mandal, G. Das, and P.K. Das. Review of oil water core annular flow. *Renew. Sust. Energ. Rev.*, 13(8):1957–1965, 2009.

[17] S.V. Apte, K. Mahesh, F. Ham, G. Constantinescu, and P. Moin. Large-eddy simulation of multiphase flows in complex combustors. *Adv. Fluid Mech.*, 37:53–62, 2004.

[18] R. Scardovelli and S. Zaleski. Direct numerical simulation of free-surface and interfacial flow. *Ann, Rev. Fluid Mech.*, 31:567–603, 1999.

[19] J.A. Sethian. *Level Set Methods and Fast Marching Methods, 2nd ed*. Cambridge University Press, Cambridge ,UK, 1999.

[20] P. Yue, C. Zhou, J.J. Feng, C.F. Ollivier-Gooch, and H.H. Hu. Phase-field simulations of interfacial dynamics in viscoelastic fluids using finite elements with adaptive meshing. *J. Comput. Phys.*, 219(1):47–67, 2006.

[21] C.W. Hirt, A.A. Amsden, and J.L. Cook. An arbitrary lagrangian-eulerian computing method for all flow speeds. *J. Comput. Phys.*, 14(3):227–253, 1974.

[22] S. Unverdi and G. Tryggvason. A front-tracking method for viscous incompressible multi-fluid flows. *J. Comput. Phys.*, 100:25–37, 1992.

[23] C.S. Peskin. Flow patterns around heart valves: a numerical method. *J. Comput. Phys.*, 10:252–271, 1972.

[24] R.J. LeVeque and Z. Li. The immersed interface method for elliptic equations with discontinuous coefficients and singular sources. *SIAM J. Numer. Anal.*, 31(4):1019–1044, 1994.

[25] J. Yang and E. Balaras. An embedded-boundary formulation for large-eddy simulation of turbulent flows interacting with moving boundaries. *J. Comput. Phys.*, 215(1):12–40, 2006.

[26] R. Mittal and G. Iaccarino. Immersed boundary methods. *Annu. Rev. Fluid Mech.*, 37:239–261, 2005.

[27] S. Marella, S. Krishnan, H. Liu, and H.S. Udaykumar. Sharp interface cartesian grid method I: an easily implemented technique for 3d moving boundary computations. *J. Comput. Phys.*, 210(1):1–31, 2005.

[28] S. Haeri and J.S. Shrimpton. On the application of immersed boundary, fictitious domain and body-conformal mesh methods to many particle multiphase flows. *Int. J. of Multiphas. Flow.*, 2011.

[29] C.S. Peskin. The immersed boundary method. *Acta Numerica*, 11:479–517, 2002.

[30] J.U. Brackbill, D.B. Kothe, and C. Zemach. A continuum method for modeling surface tension. *J. Comput. Phys.*, 100:335–354, 1992.

[31] M.G. Blyth, H. Luo, and C. Pozrikidis. Stability of axisymmetric core annular flow in the presence of an insoluble surfactant. *J. Fluid. Mech.*, 548:207–235, 2006.

[32] R. Mittal, H. Dong, M. Bozkurttas, F. M. Najjar, A. Vargas, and A. vonLoebbeck. A versatile sharp interface immersed boundary method for incompressible flows with complex boundaries. *J. Comput. Phys.*, 227(10), 2008. 4825-4852.

[33] H. Luo, H. Dai, P. Ferreira de Sousa, and B. Yin. On numerical oscillation of the direct-forcing immersed-boundary method for moving boundaries. *Comput. Fluids*. In press.

[34] S. Osher and R. Fedkiw. *Level set methods and dynamic implicit surfaces*. Springer, 2002.

[35] S. Osher and J.A. Sethian. Fronts propagating with curvature-dependent speed: algorithms based on Hamilton-Jacobi formulations. *J. Comput. Phys.*, 79:12–49, 1988.

[36] A. Harten, B. Engquist, S. Osher, and S. Chakravarthy. Uniformly high-order accurate essentially non-oscillatory schemes III. *J. Comput. Phys*, 71:231–303, 1987.

[37] C.W. Shu and S. Osher. Efficient implementation of essentially non-oscillatory shock capturing schemes. *J. Comput. Phys*, 77:439–471, 1988.

[38] X.D. Liu, S. Osher, and T. Chan. Weighted essentially non-oscillatory schemes. *J. Comput. Phys*, 126:202–212, 1996.

[39] G.S. Jiang and C.-W. Shu. Efficient implementation of weighted ENO schemes. *J. Comput. Phys*, 126:202–228, 1996.

[40] G.-S. Jiang and D. Peng. Weighted ENO schemes for Hamilton Jacobi equations. *SIAM J. Sci. Comput.*, 21:2126–2143, 2000.

[41] M. Sussman, P. Smereka, and S. Osher. A level set approach for computing solutions to incompressible two-phase flow. *J. Comput. Phys*, 114:146–159, 1994.

[42] M. Sussman and S. Uto. A computational study of the spreading of oil underneath a sheet of ice. *CAM Report*, 114:146–159, 1998.

[43] M. Sussman, A. S. Almgren, J. B. Bell, P. Colella, L. H. Howell, and M. L. Welcome. An adaptive level set approach for incompressible two-phase flows. *J. Comput. Phys*, 148:81–124, 1999.

[44] G. Russo and P. Smereka. A remark on computing distance functions. *J. Comput. Phys*, 163:51–67, 2000.

[45] D. Enright, R. Fedkiw, and J. Ferziger. A hybrid particle level set method for improved interface capturing. *J. Comput. Phys.*, 183:83–116, 2002.

[46] P.D.M. Spelt. A level-set approach for simulations of flows with multiple moving contact lines with hysteresis. *J. Comput. Phys*, 207:389–404, 2005.

[47] P.D.M. Spelt. Shear flow past two-dimensional droplets pinned or moving on an adhering channel wall at moderate Reynolds numbers: a numerical study. *J. Fluid. Mech.*, 561:439–463, 2006.

[48] M. W. Williams, D. B. Kothe, and E. G. Puckett. *Accuracy and convergence of continuum surface tension models, in Fluid Dynamics at Interfaces, edited by, W. Shyy and R. Narayanan*. Cambridge Univ. Press, Cambridge, UK, 1998.

[49] Y. Renardd and M. Renardy. PROST: A Parabolic Reconstruction of Surface Tension for the Volume-of-Fluid Method. *J. Comput. Phys.*, 183:400–421, 2002.

[50] P.-H. Chiu and Y.-T. Lin. A conservative phase field method for solving incompressible two-phase flows. *J. Comput. Phys.*, 230:185–204, 2011.

[51] M. Vanella, T. Fitzgerald, S. Preidikman, E. Balaras, and B. Balachandran. Influence of flexibility on the aerodynamic performance of a hovering wing. *J. Exp. Biol.*, 212(1):95–105, 2009.

[52] J.D. Eldredge, J. Toomey, and A. Medina. On the roles of chord-wise flexibility in a flapping wing with hovering kinematics. *J. Fluid Mech.*, 659:94–115, 2010.

[53] J. Young, S.M. Walker, R.J. Bomphrey, G.K. Taylor, and A.L.R. Thomas. Details of Insect Wing Design and Deformation Enhance Aerodynamic Function and Flight Efficiency. *Science*, 325(5947):1549, 2009.

[54] S.K. Chimakurthi, J. Tang, R. Palacios, C. Cesnik, and W. Shyy. Computational aeroelasticity framework for analyzing flapping wing micro air vehicles. *AIAA J.*, 47(8):1865–1878, 2009.

[55] S.A. Combes and T.L. Daniel. Into thin air: contributions of aerodynamic and inertial-elastic forces to wing bending in the hawkmoth Manduca sexta. *J. Exp. Biol.*, 206(17):2999–3006, 2003.

[56] J.S. Chen, J.Y. Chen, and Y.F. Chou. On the natural frequencies and mode shapes of dragonfly wings. *J. Sound Vib.*, 313(3-5):643–654, 2008.

[57] S. Heathcote, D. Martin, and I. Gursul. Flexible flapping airfoil propulsion at zero freestream velocity. *AIAA J.*, 42(11), 2004.

[58] S. Heathcote and I. Gursul. Flexible flapping airfoil propulsion at low Reynolds numbers. *AIAA J.*, 45(5):1066–1079, 2007.

[59] S. Heathcote, Z. Wang, and I. Gursul. Effect of spanwise flexibility on flapping wing propulsion. *J. Fluid Struct.*, 24(2):183–199, 2008.

[60] Q. Zhu. Numerical simulation of a flapping foil with chordwise or spanwise flexibility. *AIAA J.*, 45(10):2448–2457, 2007.

[61] S. Michelin and S.G.L. Smith. Resonance and propulsion performance of a heaving flexible wing. *Phys. Fluid*, 21:071902, 2009.

[62] Z.J. Wang, J.M. Birch, and M.H. Dickinson. Unsteady forces and flows in low Reynolds number hovering flight: two-dimensional computations vs robotic wing experiments. *J. Exp. Biol.*, 207(3):449–460, 2004.

[63] J. D. Eldredge. Numerical simulation of the fluid dynamics of 2d rigid body motion with the vortex particle method. *J. Comput. Phys.*, 221:626–648, 2007.

[64] C. Pozrikidis. Buckling and collapse of open and closed cylindrical shells. *J. Eng. Math.*, 42:157–180, 2002.

[65] E. Volterra and EC Zachmanoglou. *Dynamics of vibrations*. CE Merrill Books, Columbus, 1965.

[66] H. Luo, R. Mittal, X. Zheng, S. A. Bielamowicz, R. J. Walsh, and J. K. Hahn. An immersed-boundary method for flow–structure interaction in biological systems with application to phonation. *J. Comput. Phys.*, 227(22):9303–9332, 2008.

[67] H. Luo, B. Yin, H. Dai., and J. F. Doyle. A 3D computational study of the flow–structure interaction in flapping flight. *AIAA Paper 2010-556*, 2010.

[68] H. Aono, F. Liang, and H. Liu. Near-and far-field aerodynamics in insect hovering flight: an integrated computational study. *J. Exp. Biol*, 211(2):239, 2008.

[69] S. Sunada, L. Zeng, and K. Kawachi. The relationship between dragonfly wing structure and torsional deformation. *J. Theor. Biol*, 193(1):39–45, 1998.

[70] C.H.K. Williamson and R. Govardhan. Vortex-induced vibrations. *Annu. Rev. Fluid Mech.*, 36:413–455, 2004.

[71] M.M. Bernitsas, K. Raghavan, Y. Ben-Simon, and E.M.H. Garcia. VIVACE (vortex induced vibration aquatic clean energy): A new concept in generation of clean and renewable energy from fluid flow. *Journal of Offshore Mechanics and Arctic Engineering*, 130:041101, 2008.

[72] D. Weihs. Hydromechanics of fish schooling. *Nature*, 241:290–291, 1973.

[73] P.B.S. Lissaman and C.A. Shollenberger. Formation flight of birds. *Science*, 168(3934):1003–1005, 1970.

[74] R.W. Whittlesey, S. Liska, and J.O. Dabiri. Fish schooling as a basis for vertical axis wind turbine farm design. *Bioinspiration & Biomimetics*, 5:035005, 2010.

[75] M.M. Zdravkovich and D.L. Pridden. Interference between two circular cylinders; series of unexpected discontinuities. *Journal of Wind Engineering and Industrial Aerodynamics*, 2(3):255–270, 1977.

[76] M.M. Zdravkovich. Review of interference-induced oscillations in flow past two parallel circular cylinders in various arrangements. *Journal of Wind Engineering and Industrial Aerodynamics*, 28(1-3):183–199, 1988.

[77] S. Mittal and V. Kumar. Flow-induced oscillations of two cylinders in tandem and staggered arrangements. *J. Fluids & Struct.*, 15(5):717–736, 2001.

[78] I. Borazjani and F. Sotiropoulos. Vortex-induced vibrations of two cylinders in tandem arrangement in the proximity-wake interference region. *J. Fluid Mech.*, 621:321, 2010.

[79] L. Ristroph and J. Zhang. Anomalous hydrodynamic drafting of interacting flapping flags. *Phys. Rev. Lett.*, 101(19):194502, 2008.

[80] L. Zhu. Interaction of two tandem deformable bodies in a viscous incompressible flow. *J. Fluid Mech.*, 635(1):455–475, 2009.

[81] H. Luo, H. Dai, P. Ferreira de Sousa, and B. Yin. On the numerical oscillation of the direct-forcing immersed-boundary method for moving boundaries. *Comput. Fluids*, 56:61–76, 2012.

[82] B. Yin and H. Luo. Effect of wing inertia on hovering performance of flexible flapping wings. *Phys. Fluids*, 22:111902, 2010.

[83] F. Tian, H. Luo, J. Song, and X.-Y. Lu. Force production and asymmetric deformation of a flexible flapping wing in forward flight. *J. Fluids Struct.*, 2012. In press.

[84] H. Dai, H. Luo, and J.F. Doyle. Dynamic pitching of an elastic rectangular wing in hovering motion. *Journal of Fluid Mechanics*, 693:473–499, 2012.

[85] R. Milla and P.B. Reich. The scaling of leaf area and mass: the cost of light interception increases with leaf size. *Proceedings of the Royal Society B: Biological Sciences*, 274(1622):2109–2115, 2007.

[86] W.B. Hobbs and D.L. Hu. Tree-inspired piezoelectric energy harvesting. *J. Fluids & Struct.*, 28:103–114, 2012.

[87] Z. Yang, S. Matsumoto, H. Goto, M. Matsumoto, and R. Maeda. Ultrasonic micromixer for microfluidic systems. *Sensors and Actuators A: Physical*, 93(3):266–272, 2001.

[88] J.H. Tsai and L. Lin. Active microfluidic mixer and gas bubble filter driven by thermal bubble micropump. *Sensors and Actuators A: Physical*, 97:665–671, 2002.

[89] H.H. Bau, J. Zhong, and M. Yi. A minute magneto hydro dynamic (mhd) mixer. *Sensors and Actuators B: Chemical*, 79(2-3):207–215, 2001.

[90] L. Capretto, W. Cheng, M. Hill, and X. Zhang. Micromixing within microfluidic devices. *Microfluidics*, pages 27–68, 2011.

[91] M. Muradoglu and H.A. Stone. Mixing in a drop moving through a serpentine channel: A computational study. *Physics of Fluids*, 17:073305, 2005.

[92] ZB Stone and HA Stone. Imaging and quantifying mixing in a model droplet micromixer. *Physics of Fluids*, 17:063103, 2005.

[93] A. Liau, R. Karnik, A. Majumdar, and J.H.D. Cate. Mixing crowded biological solutions in milliseconds. *Analytical chemistry*, 77(23):7618–7625, 2005.

[94] T.M. Tsai and M.J. Miksis. Dynamics of a drop in a constricted capillary tube. *J. Fluid. Mech.*, 274:197–217, 1994.

[95] H. Liu, S. Krishnan, S. Marella, and HS Udaykumar. Sharp interface cartesian grid method ii: A technique for simulating droplet interactions with surfaces of arbitrary shape. *Journal of Computational Physics*, 210(1):32–54, 2005.

[96] J. Yang and F. Stern. Sharp interface immersed-boundary/level-set method for wave–body interactions. *Journal of Computational Physics*, 228(17):6590–6616, 2009.

[97] M. Kang, R.P. Fedkiw, and X.D. Liu. A boundary condition capturing method for multiphase incompressible flow. *Journal of Scientific Computing*, 15(3):323–360, 2000.

[98] H. Luo, M.G. Blyth, and C. Pozrikidis. Two-layer flow in a corrugated channel. *J. Eng. Math*, 60:127–147, 2008.

[99] S. Guido and Marco. Villone. Three-dimensional shape of a drop under simple shear flow. *J. Rheol.*, 42:395–444, 1998.

[100] G.I. Taylor. The viscosity of a fluid containing small drops of another fluid. *Proc. R. Soc. London*, Ser. A 138:41–48, 1932.

[101] G.I. Taylor. The formation of emulsions in definable fields of flow. *Proc. R. Soc. London*, Ser. A 146:501–523, 1934.

[102] J.M. Rallison. The deformation of small viscous drop and bubbles in shear flow. *Annu. Rev. Fluid Mech.*, 16:45–66, 1984.

[103] A. J. Griggs, A. Z. Zinchenko, and R. H. Davis. Low-Reynolds-number motion of a deformable drop between two parallel plane walls. *Intl. J. Multiphas. Flow.*, 33:182–206, 2007.

[104] S. Mortazavi and G. Tryggvason. A numerical study of the motion of drops in Poiseuille flow. Part 1. Lateral migration of one drop. *J. Fluid. Mech.*, 411:325–350, 2000.